LA-UR-12-20353
Approved for public release; distribution is unlimited.

Title:	Deflagration Wave Profiles
Author(s):	Menikoff, Ralph
Intended for:	OSTI web site Report

Deflagration Wave Profiles

Ralph Menikoff

February 20, 2012

Abstract

Shock initiation in a plastic-bonded explosives (PBX) is due to hot spots. Current reactive burn models are based, at least heuristically, on the *ignition and growth* concept. The ignition phase occurs when a small localized region of high temperature (or hot spot) burns on a fast time scale. This is followed by a growth phase in which a reactive front spreads out from the hot spot. Propagating reactive fronts are deflagration waves. A key question is the deflagration speed in a PBX compressed and heated by a shock wave that generated the hot spot. Here, the ODEs for a steady deflagration wave profile in a compressible fluid are derived, along with the needed thermodynamic quantities of realistic equations of state corresponding to the reactants and products of a PBX. The properties of the wave profile equations are analyzed and an algorithm is derived for computing the deflagration speed. As an illustrative example, the algorithm is applied to compute the deflagration speed in shock compressed PBX 9501 as a function of shock pressure. The calculated deflagration speed, even at the CJ pressure, is low compared to the detonation speed. The implication of this are briefly discussed.

Contents

1 Background

Across a steady wave, the hydrodynamic variables must satisfy the Rankine-Hugoniot jump relations. For reactive flow, a discussion of the detonation and deflagration loci is given in Courant and Friedrichs [1976, Chpt. III E]. In contrast to a shock or detonation wave, both the ahead and behind states of a deflagration wave are subsonic. Moreover, for a given ahead state, not all points on the deflagration locus are physically admissible. A deflagration waves must have a steady continuous wave profile. Unlike, shock and detonation waves, the admissible deflagration waves depend on transport properties; in particular, on thermal conduction.

1.1 Gaseous combustion

Most of the theory for deflagration waves has been developed in the context of gaseous combustion in the high activation energy limit. This enables the use of simplifying approximations; low wave speed compared to the sound speed and nearly constant pressure across the wave. Consequently, the flow model can be reduced to an equation for the conservation of energy and a rate equation for the reaction progress variable. Furthermore, the energy equation can be expressed in the form of a diffusion equation for the temperature. The key material parameters for a deflagration wave are then the specific heat at constant pressure and the coefficient of thermal diffusion.

In contrast, for a reactive solid in the high pressure regime that occurs during a shock-to-detonation transition, the equation of states of the reactants and products are important and very non-ideal. As a result, the simplifying assumptions used for gaseous deflagrations are not applicable. Therefore, the full set of conservation laws (mass, momentum, energy) for compressible reactive flow needs to be analyzed.

1.2 Deflagration wave profile

A study of deflagration waves by Friedrichs [1946], using the full set of reactive flow equations with an Arrhenius reaction rate and an ideal explosive equation of state, concluded that for a given initial state, a steady wave profile with heat conduction and viscosity only exists for one point on the deflagration locus; see also, [Courant and Friedrichs, 1976, §91]. Subsequently,

existence and uniqueness of detonation and deflagration wave profiles have been studied in great detail, see for example Wagner [1989], Gasser and Szmolyan [1993] and references therein. These analyzes are highly dependent on the use of a simplified ideal explosive equation of state (EOS); see App. A. While many of the qualitative properties of deflagration waves are independent of the EOS, there are significant differences between the deflagration loci of a gaseous explosive with an ideal EOS and a solid explosive with a realistic EOS; see App. B .

The purpose of this article is to review the theory and equations that describe steady deflagration waves in one-dimension with an eye towards calculating the deflagration speed for a specific explosive. The focus, in particular, is on solid explosives described by realistic equations of state.

1.3 Solid high explosives

The main motivation for this work is to gain a better understanding of shock initiation in a plastic-bonded explosive (PBX). Due to material heterogeneities, shock compression gives rise to hot spots or small localized regions of high temperature. This leads to the ignition and growth concept used in reactive burn models; see [Menikoff, 2009a] and references therein. The ignition phase is the formation and burning of hot spots on a fast time scale. This is followed by a growth phase in which a reactive front is triggered by the high temperature of each burned hot spot. A propagating reactive front is a deflagration wave. A key question is the deflagration speed in the shock compressed PBX.

Briefly, the material covered is organize as follows. First, the ODEs for the wave profile of a steady deflagration wave are derived. The ahead and behind states of the wave profile are critical points. Second, the stable manifolds for each critical point are determined. Third, the properties of the trajectories of the ODEs are analyzed. This enables a numerical shooting algorithm to be derived for computing the deflagration speed of an explosive with an arbitrary EOS.

As an illustrative example, the shooting algorithm is applied to the high explosive PBX 9501. The deflagration speed is computed as a function of pressure for the ahead state on the principal Hugoniot locus. The deflagration speed, even at high shock pressure, turns out to be low compared to the detonation speed. The implication are briefly discussed in the final section.

2 Reactive flow PDEs

The one-dimensional PDEs for reactive fluid flow with viscosity and heat conduction in Lagrangian form are

$$\frac{\mathsf{d}}{\mathsf{d}t}V - \quad V\frac{\partial}{\partial x}u = 0 \ , \tag{1a}$$

$$\frac{\mathsf{d}}{\mathsf{d}t}u + \quad V\frac{\partial}{\partial x}P = V\frac{\partial}{\partial x}\Big(\nu\frac{\partial}{\partial x}u\Big) \ , \tag{1b}$$

$$\frac{\mathsf{d}}{\mathsf{d}t}e + PV\frac{\partial}{\partial x}u = V\,\nu\Big(\frac{\partial}{\partial x}u\Big)^2 + V\frac{\partial}{\partial x}\Big(\kappa\frac{\partial}{\partial x}T\Big) \ , \tag{1c}$$

$$\frac{\mathsf{d}}{\mathsf{d}t}\lambda \qquad\qquad = \mathcal{R} \ , \tag{1d}$$

where $\frac{\mathsf{d}}{\mathsf{d}t} = \frac{\partial}{\partial t} + u\frac{\partial}{\partial x}$ is the convective time derivative, λ is a reaction progress variable, $\mathcal{R}$ is the reaction rate, ν is the coefficient of dynamic viscosity, and κ is the coefficient of thermal conduction. The usual hydrodynamic and thermodynamic variables for particle velocity, specific volume, specific internal energy, pressure and temperature are denoted by u, V, e, P and T, respectively. We take λ to be the mass fraction of the products. Moreover, the chemical energy associated with the reaction is included in e. Hence, there is no energy source term due to the reaction.

We assume a pressure-temperature equilibrium EOS for partly burned explosive; *i.e.*, $P = P(V, e, \lambda)$ is based on reactants ($\lambda = 0$) and products ($\lambda = 1$) equations of state, which we denote by subscripts 'r' and 'p', respectively. The equilibrium EOS is defined by the Gibbs free energy

$$G(P, T, \lambda) = \lambda\, G_p(P, T) + (1 - \lambda)\, G_r(P, T) \ . \tag{2}$$

This leads to the fundamental thermodynamic identity

$$\mathsf{d}e = -P\,\mathsf{d}V + T\,\mathsf{d}S + (\Delta G)\,\mathsf{d}\lambda \ , \tag{3}$$

where $\Delta G = G_p - G_r$, $S = -(\partial_T G)_{P,\lambda}$ is the specific entropy, and $e = G + T\,S - P\,V$. From general thermodynamic relations, it follows that the mixture quantities are given by

$$\begin{aligned} V &= \lambda V_p + (1 - \lambda)V_r \ , \\ e &= \lambda e_p + (1 - \lambda)e_r \ , \\ S &= \lambda S_p + (1 - \lambda)S_r \ , \end{aligned} \tag{4}$$

where V_p, e_p and S_p are functions of P and T, and similarly for V_r, e_r and S_r. This defines a mixture EOS for the pressure $\tilde{P}(V, T, \lambda)$, which can be re-expressed as $P(V, e, \lambda)$, provided that the EOS of the reactants and products are each thermodynamically consistent (derivable from a potential) and thermodynamically stable (entropy jointly concave in e and V).

Remarks:

(i) More precisely, the convective time derivative should be written $\left(\frac{\partial}{\partial t}\right)_m$ where m is the Lagrangian mass variable defined by $\mathsf{d}m = \rho\,\mathsf{d}x$. However, we later use m for mass flux.

(ii) We have assumed a Newtonian viscosity for which the viscous pressure Q has a linear form; $Q = -\nu\frac{\partial}{\partial x}u$. The coefficient of dynamic viscosity ν has dimensions of pressure·time. Furthermore, we assume ν is constant. For more detailed discussion of viscous stress, see for example, http://en.wikipedia.org/wiki/Viscosity. Other forms for the viscous pressure are possible. In particular, numerical shock capturing algorithms frequently use a quadratic form for the artificial viscosity; $Q = -\left(\nu_1 + \nu_2|\frac{\partial}{\partial x}u|\right)\frac{\partial}{\partial x}u$.

(iii) The heat flux, $q = -\kappa\frac{\partial}{\partial x}T$, has dimensions energy/(time·length^2). Hence κ has dimensions energy/(length·time·K). The coefficient of thermal diffusion is $k = \kappa/(\rho\, C_r)$, and has dimensions of length^2/time. Here, C_r is a reference value for the specific heat.

(iv) We assume that the reaction, *reactants* $\rightarrow$ *products*, is irreversible; *i.e.*, $\mathcal{R} \geq 0$. Moreover, $\mathcal{R} = 0$ when $\lambda = 1$, *i.e.*, reactants are completely burned.

(v) Reaction contributes to the entropy production. From Eq. (3) and Eq. (1c), one can derive an equation for the specific entropy;

$$\frac{\mathsf{d}}{\mathsf{d}t}S - V\,\frac{\partial}{\partial x}\left(\frac{\kappa}{T}\frac{\partial}{\partial x}T\right) = \nu\,\frac{V}{T}\left(\frac{\partial}{\partial x}u\right)^2 + \kappa\,\frac{V}{T^2}\left(\frac{\partial}{\partial x}T\right)^2 - \frac{\Delta G}{T}\,\mathcal{R}\ . \qquad (5)$$

For an irreversible reaction, $\Delta G < 0$ and $R \geq 0$. Hence, the dissipation, *i.e.*, the right hand side of Eq. (5), is positive. We further assume that the explosive is exothermic; *i.e.*, $\Delta h < 0$, where $h = e + P\,V$ is the enthalpy.

(vi) Formulae for the equilibrium mixture thermodynamic quantities (specific heat C_V, Grüneisen coefficient Γ and sound speed c), in terms of those of the components, are derived in Appendix C. We note that the mixture quantities are not constant. Moreover, for realistic reactants and products EOS, the component specific heats are temperature dependent. In addition,

for fixed λ, we assume that the EOS is convex, $(\partial_V^2 P)_S > 0$, and that the Grüneisen coefficient is positive. Other mixture rules for $P(V, e, \lambda)$ are possible. However, it is important that the EOS is thermodynamically consistent (satisfy Eq. (3) with ΔG independent of λ) and thermodynamically stable (mixture entropy is jointly concave in V, e for fixed λ). This enables our analysis to make use of various thermodynamic identities, such as those listed in Appendix A of [Menikoff and Plohr, 1989].

(vii) For later use, we note variations of Eq. (3) for fixed λ and different pairs of independent thermodynamic variables:

$$\begin{aligned} \mathsf{d}e &= -\Big(1 - \Gamma \tfrac{C_V T}{P V}\Big) P \, \mathsf{d}V + C_V \, \mathsf{d}T \ , \\ \Gamma \, \mathsf{d}e &= (\gamma - \Gamma) P \, \mathsf{d}V + V \, \mathsf{d}P \ , \\ \Gamma \, C_V \, \mathsf{d}T &= K_T \, \mathsf{d}V + V \, \mathsf{d}P \ , \end{aligned} \tag{6}$$

where $\gamma = c^2/(P\,V)$ is the adiabatic exponent, and K_T is the isothermal bulk modulus. Thermodynamic stability requires that $K_T > 0$. Furthermore, we assume that $\gamma \geq \Gamma + 1$, which is a sufficient condition for stability of shock waves. These inequalities determine the sign of some thermodynamic derivatives that play an important role in the analysis.

(viii) Mass diffusion — additional terms $V \frac{\partial}{\partial x}\Big[d \frac{\partial}{\partial x}\lambda\Big]$ and $V \frac{\partial}{\partial x}\Big[(e_p - e_r)\, d \frac{\partial}{\partial x}\lambda\Big]$ on the right hand sides of Eq. (1d) and Eq. (1c), respectively, where d is the coefficient of mass diffusion with dimensions of mass/(length·time) — is often included for gaseous combustion; see for example [Kassoy, 1985] and reference therein. We have left these terms out since our aim is to describe deflagration waves in reactive solids at high pressure; *i.e.*, the close packing of molecules at solid density severely restricts their ability to diffuse.

3 Steady-state ODEs

For a steady wave, all hydrodynamic and thermodynamic quantities are functions of the variable

$$\xi = x - D\,t \ ,$$

where D is the wave speed. We assume a right facing wave, for which $D > 0$. Substituting $\frac{\partial}{\partial t} = -D \, \frac{\mathsf{d}}{\mathsf{d}\xi}$ and $\frac{\partial}{\partial x} = \frac{\mathsf{d}}{\mathsf{d}\xi}$, the PDEs reduce to ODEs:

$$(D-u)\,\frac{\mathsf{d}}{\mathsf{d}\xi}V = -V\frac{\mathsf{d}}{\mathsf{d}\xi}u\ , \tag{7a}$$

$$(D-u)\,\frac{\mathsf{d}}{\mathsf{d}\xi}u = V\frac{\mathsf{d}}{\mathsf{d}\xi}\Big(P+Q\Big)\ , \tag{7b}$$

$$(D-u)\,\frac{\mathsf{d}}{\mathsf{d}\xi}e = \Big(P+Q\Big)V\frac{\mathsf{d}}{\mathsf{d}\xi}u - V\frac{\mathsf{d}}{\mathsf{d}\xi}\Big(\kappa\frac{\mathsf{d}}{\mathsf{d}\xi}T\Big)\ , \tag{7c}$$

$$(D-u)\,\frac{\mathsf{d}}{\mathsf{d}\xi}\lambda = -\mathcal{R}\ , \tag{7d}$$

where the steady-state viscous pressure is

$$Q = -\nu\frac{\mathsf{d}}{\mathsf{d}\xi}u\ . \tag{7e}$$

Asymptotically the derivatives of all variables are assumed to vanish at the end states; *i.e.*, as $\xi \to \pm\infty$. We denote the ahead and behind states, corresponding to $\lambda = 0$ and 1, respectively, by the subscripts '0' and '1'. For a right facing wave, the ahead state is at $\xi = \infty$ and the behind state at $\xi = -\infty$. Moreover, $D - u > 0$.

The mass equation (7a) can be expressed as $\frac{\mathsf{d}}{\mathsf{d}\xi}\Big[(D-u)\,\rho\Big] = 0$, where $\rho = 1/V$ is the density. The first integral is

$$(D-u)\rho = m = \text{mass flux}\ . \tag{8a}$$

Alternatively,

$$\Delta V = -\Delta u/m\ , \tag{8b}$$

where $\Delta f = f(\xi) - f(\infty)$ is the change in the variable f relative to its value at $\xi = \infty$, or $\Delta f = f(\xi) - f_0$. For a right facing wave, $m > 0$, and mass flows from $\xi = +\infty$ to $-\infty$, *i.e.*, right to left.

Remark: Since all derivatives vanish at $\xi = \infty$, for any $f' = \frac{\mathsf{d}}{\mathsf{d}\xi}f$, $\Delta f' = f'(\xi)$.

The first integral of the momentum equation (7b) constrains the flow to be along a modified '*Rayleigh line*';

$$\begin{aligned}\Delta\Big(P+Q\Big) &= m\,\Delta u \\ &= -m^2\Delta V\ .\end{aligned} \tag{9a}$$

Substituting Eq. (7e), we obtain

$$\nu \, \frac{\mathsf{d}}{\mathsf{d}\xi} u = \Delta \Big[P + m^2 \, V \Big] \; , \tag{9b}$$

or by Eq. (8b)

$$\Big(\nu \, m \Big) \, \frac{\mathsf{d}}{\mathsf{d}\xi} V = - \, \Delta \Big[P + m^2 \, V \Big] \; . \tag{9c}$$

We note that the right hand side vanishes when V and P lie on the Rayleigh line, $P_{\mathcal{L}}(V) = P_0 - m^2 (V - V_0)$.

The energy equation (7c) can be combined with Eqs. (7b) and (8a) as follows:

$$\begin{aligned} -\frac{\mathsf{d}}{\mathsf{d}\xi} \Big(\kappa \frac{\mathsf{d}}{\mathsf{d}\xi} T \Big) &= m \, \frac{\mathsf{d}}{\mathsf{d}\xi} e - (P + Q) \, \frac{\mathsf{d}}{\mathsf{d}\xi} u \\ &= m \, \frac{\mathsf{d}}{\mathsf{d}\xi} e + \frac{\mathsf{d}}{\mathsf{d}\xi} \Big[(P + Q)(D - u) \Big] - (D - u) \, \frac{\mathsf{d}}{\mathsf{d}\xi} \Big(P + Q \Big) \\ &= m \, \frac{\mathsf{d}}{\mathsf{d}\xi} \Big[e + (P + Q) \, V + \tfrac{1}{2} (D - u)^2 \Big] \; . \end{aligned}$$

The first integral gives a modified '*Bernoulli relation*';

$$\kappa \, \frac{\mathsf{d}}{\mathsf{d}\xi} T = - m \, \Delta \Big[e + (P + Q) \, V + \tfrac{1}{2} (D - u)^2 \Big] \; . \tag{10a}$$

Substituting Eq. (9a) to eliminate $P + Q$ and Eq. (8a) to eliminate the velocity, yields

$$\kappa \, \frac{\mathsf{d}}{\mathsf{d}\xi} T = - m \, \Big[\Delta[e] - \Big[P_0 + \tfrac{1}{2} m^2 (V_0 - V) \Big] \Big(V_0 - V \Big) \Big] \; . \tag{10b}$$

We note that the factor $P_0 + \frac{1}{2} m^2 (V_0 - V)$ can be expressed as $\frac{1}{2} [P_0 + P_{\mathcal{L}}(V)]$.

Collecting the results, equations (9c), (10b) and (7d), the ODEs for the wave profile can be expressed as

$$\Big(\frac{\nu}{m} \Big) \, \frac{\mathsf{d}}{\mathsf{d}\xi} V = - \, \frac{1}{m^2} \, \Delta \Big[P + m^2 \, V \Big] \; , \tag{11a}$$

$$\Big(\frac{\kappa}{m C_V} \Big) \, \frac{\mathsf{d}}{\mathsf{d}\xi} T = - \, \frac{1}{C_V} \, \Big(\Delta[e] + \Big[P_0 - \tfrac{1}{2} \, m^2 (V - V_0) \Big] \cdot \Big[V - V_0 \Big] \Big) \; , \tag{11b}$$

$$\Big(m \, V \Big) \, \frac{\mathsf{d}}{\mathsf{d}\xi} \lambda = - \, \mathcal{R}(V, T, \lambda) \; . \tag{11c}$$

The system of 3 ODEs is closed by using the equation of state for the pressure and the specific internal energy; *i.e.*, P=$\widetilde{P}(V,T,\lambda)$ and $e = e(V,T,\lambda)$.

Across a deflagration wave P decreases while V and T increase. Moreover, in the wave profile, these quantities typically vary monotonically. The variations are related by the thermodynamic relation

$$\mathsf{d}P = K_T\Big[-\frac{\mathsf{d}V}{V} + \frac{V_p - V_r}{V}\mathsf{d}\lambda\Big] + \frac{\Gamma}{V}C_V T\,\frac{\mathsf{d}T}{T}\ , \tag{12}$$

where we have substituted Eq. (C.21) for $(\partial_\lambda \widetilde{P})_{V,T}$. In order for P to decrease monotonically, the change from increasing V must be larger than the combined change from increasing λ and increasing T. This can occur because $K_T \gg \frac{\Gamma}{V}C_V\,T$. An additional requirement is that $-\mathsf{d}V > (V_p - V_r)\mathsf{d}\lambda$. From Eq. (11), this requirement can be expressed as

$$\Delta\Big(P + m^2 V\Big) > \frac{V_p - V_r}{V}\,\nu\mathcal{R}\ . \tag{13}$$

Typically, this inequality is satisfied because ν is sufficiently small. For the special case of an ideal explosive EOS, Appendix A, the inequality follows from the fact that $V_p = V_r$; *i.e.*, the pressure depends on V and T, and is independent of λ.

3.1 Scaled ODEs

Physically, reaction rates are temperature sensitive and heat conduction determines the rate which drives a deflagration wave. It is natural to define a length scale based on the thermal conduction;

$$\ell = \frac{\kappa}{m\,C_r}\ .$$

Here, C_r is a reference value for the specific heat. For a solid propellant or explosive, $C_P \gtrsim C_V$. Moreover, the specific heat is temperature dependent. Reasonable estimates for C_r may vary by a factor of 2. Alternately, the length scale may be expressed in terms of the viscosity and the Prandtl number

$$\ell = \frac{\nu}{m\,Pr} \qquad \text{and} \qquad Pr = \frac{C_r\,\nu}{\kappa}\ .$$

Typically, for gaseous combustion $Pr \approx 1$. For solid reactants, $Pr \gg 1$; see for example § 8.2.1.

In terms of the dimensionless length $\zeta = \xi/\ell$, Eq. (11) can be re-expressed as

$$\frac{\mathsf{d}}{\mathsf{d}\zeta} V = - Pr^{-1} \frac{1}{m^2} \Delta\Big[P + m^2 V\Big] \ , \tag{14a}$$

$$\frac{\mathsf{d}}{\mathsf{d}\zeta} T = - \frac{1}{C_r} \Big(\Delta[e] + \Big[P_0 - \tfrac{1}{2} m^2 (V - V_0)\Big] \cdot \Big[V - V_0\Big] \Big) \ , \tag{14b}$$

$$\frac{\mathsf{d}}{\mathsf{d}\zeta} \lambda = - \frac{\ell}{m V} \mathcal{R}(V, T, \lambda) \ . \tag{14c}$$

This scaling is advantageous for calculating deflagration profiles numerically. Since the right hand side of Eq. (11b) is near zero, without the scaling it would be multiplied by a large number (mC_V/κ) and roundoff errors may cause large errors in computing $\frac{\mathsf{d}}{\mathsf{d}\xi} T$. However, for a weak deflagration wave (small m) and $Pr \simeq 1$, there is still a potential issue with roundoff errors for Eq. (14a). Thus, length scaling can help with one equation but not necessarily for both the energy and momentum equations.

We expect the reaction to occur on a comparable scale to that over which the temperature changes; namely, ℓ. Having used this as the length scale, a distinguished solution of the wave profile ODEs should occur when the maximum of the right hand side of Eq. (14c) (or the Damköler number) is $\mathcal{O}(1)$.

In this case, the natural time scale, τ, for a deflagration is the inverse of the peak of the rate; $\tau = 1/\mathcal{R}(V_1, T_1, 0)$. Hence,

$$m V \sim \frac{\ell}{\tau} = \frac{\kappa}{m C_r \tau} \ .$$

Consequently, the deflagration speed and thermal length would be

$$D - u_0 \sim \left[\frac{\kappa V_0}{C_r \tau}\right]^{1/2} \qquad \text{and} \qquad \ell \sim (D - u_0)\, \tau \ . \tag{15}$$

We note that $k = \kappa V_0/C_r$ is the coefficient of thermal diffusion. Hence, $D - u_0 \sim (k/\tau)^{1/2}$ and $\ell \sim (k\,\tau)^{1/2}$.

It may seem counter-intuitive, but the length scale and hence the deflagration wave width increases with the thermal conductivity. A shock profile has the analogous property that its width increases with the coefficient of viscosity.

Another distinguished type of deflagration profile occurs for a ZND detonation wave, which can be thought of as a shock followed by a deflagration. In this case, the deflagration profile is dominated by the reaction rate rather than heat conduction. Consequently, the appropriate length scale is given by $\tilde{\ell} = mV_0\tau = D\,\tau$. Moreover, we expect $\ell \ll \tilde{\ell}$, and the right hand side of Eq. (14c) is less than $\ell/\tilde{\ell}$ and would be very small.

In terms of the dimensionless length $z = \xi/\tilde{\ell}$, Eq. (11) can be re-expressed as

$$\left(\frac{\nu}{V_0\tau}\right)\Delta\frac{\mathsf{d}}{\mathsf{d}z}V = -\,\Delta\Big[P + m^2\,V\Big]\;, \tag{16a}$$

$$\left(\frac{\kappa}{m^2V_0\tau}\right)\Delta\frac{\mathsf{d}}{\mathsf{d}z}T = -\left(\Delta[e] + \Big[P_0 - \tfrac{1}{2}\,m^2(V - V_0)\Big]\cdot\Big[V - V_0\Big]\right)\;, \tag{16b}$$

$$\frac{\mathsf{d}}{\mathsf{d}z}\lambda = -\tau\,\frac{V_0}{V}\,\mathcal{R}(V,T,\lambda)\;. \tag{16c}$$

It is important to note that the derivatives behind the lead shock do not vanish. This provides a degree of freedom needed for a deflagration profile solution to exist when the wave speed or mass flux is determined by the Hugoniot locus state rather than Eq. (15).

We note that right hand sides of Eqs. (16a) and (16b) correspond to shock jump conditions. Their vanishing would contradict non-zero derivatives of V and T behind the shock. However, these can be justified as follows. Physically, the shock jump conditions are a statement of the conservation laws; the flux matches across a discontinuity or a steady wave. Viscosity gives rise to a momentum flux and heat conduction to an energy flux. When ν and κ are small, these fluxes would be a small perturbation on the Hugoniot locus. Moreover, viscosity and heat conduction give rise to a smooth shock profile. We will see later when trajectories of the ODEs are discussed that nearby trajectories from the ahead state display a rapid variation of the slope in the (V,T)-plane near the state behind the shock, as shown in Fig. 3. Typically, the shock rise time is very short and a negligible amount of reaction occurs in the shock profile.

Remarks:

(i) Conventional analysis also scales the hydrodynamic variables. However, in contrast to an ideal explosive EOS, realistic equations of state are not scale invariant, and non-dimensional hydrodynamic variables are not so helpful. Instead, for the critical point analysis in sec. 5, we use the relative change in V and T, which are dimensionless variables.

(ii) Typically, the pressure change across a weak deflagration wave is small. It is common in analysis of gas combustion to use a constant pressure approximation in place of the momentum equation. The justification is that for $Pr = \mathcal{O}(1)$ and small m, Eq. (14a) is singular. Hence the right hand side must vanish; *i.e.*, $P = P_0 - m^2 (V - V_0)$. Small m then implies that P is nearly constant. Numerical examples in sec. 8.2.2 show when κ is not sufficiently small that m need not be small. Furthermore, when ν is not sufficiently small, P need not be monotonic, let alone constant.

4 Preliminary considerations

Conditions are needed on the end points of a deflagration wave in order for the wave profile ODEs to have a solution whose derivatives vanish asymptotically.

4.1 Deflagration locus

For a given ahead state, the possible behind states of a steady reactive wave are determined by the Hugoniot equation;

$$e_1 - e_0 = \tfrac{1}{2} \left[P(V_1, e_1, \lambda_1) + P_0 \right] \cdot \left[V_0 - V_1 \right] , \tag{17a}$$

where $P_0 = P(V_0, e_0, \lambda_0)$, $\lambda_0 = 0$ and $\lambda_1 = 1$. The mass and momentum jump conditions then determine the mass flux, the deflagration speed and the particle velocity;

$$m^2 = (P_1 - P_0)/(V_0 - V_1) , \tag{17b}$$

$$\rho_0 (D - u_0) = m = \rho_1 (D - u_1) . \tag{17c}$$

On the deflagration branch of the reactive Hugoniot locus, $V_1 > V_0$. Assuming a convex EOS, for a given deflagration speed, the Hugoniot equation

has at most two solutions. These are denoted as weak and strong deflagrations with $V_0 < V_w < V_s$ and $P_0 > P_w > P_s$. The weak and strong states coincide for the CJ-wave speed. The other limit of a weak deflagration corresponds to constant pressure burn; $P = P_0$ and $D - u_0 = 0$. Typically, the strong branch ends at a finite V and $P \geq 0$. Thus, the weak and strong branches of the deflagration locus lies within a finite interval in both P and V.

In contrast to the detonation branch ($V_1 < V_0$), the CJ-state on the deflagration locus is an entropy maximum and the deflagration speed is a maximum. Since

$$(S_{CJ})_{\text{defl}} \geq S_w > (S_{CJ})_{\text{det}} > S_0 \ ,$$

the entire weak branch of the deflagration locus is entropy increasing. This is a consequence of $\Delta G < 0$ and the associate entropy increase from reaction. Thus reaction enables expansive waves to be physically possible. We note that the CJ-state does not have the same significance for a deflagration that it does for a detonation; *i.e.*, there is no equivalent of an underdriven or unsupported detonation wave. Moreover, we later prove, see Theorem 7.1, that a wave profile can not end on the strong branch of the deflagration locus. Hence, strong deflagration waves are inadmissible.

Without loss of generality, we may take the initial state to be at rest; *i.e.*, $u_0 = 0$. Then the deflagration speed is restricted to the interval $0 < D \leq D_{cj}$. For a weak deflagration wave, $V_0 \leq V_1 < V_{cj}$ and $u_1 < 0$. Moreover, for a right facing wave $\frac{\mathrm{d}}{\mathrm{d}\zeta}\lambda < 0$, and one might expect that $\frac{\mathrm{d}}{\mathrm{d}\zeta}V < 0$. This implies that $\frac{\mathrm{d}}{\mathrm{d}\zeta}u > 0$ and the viscous pressure $Q \leq 0$. By Eq. (11a) the deflagration profile in the (V, P)-plane would lie above the Rayleigh line. We later prove that V is indeed monotonic on a deflagration wave profile.

As with a shock wave, the behind state of a deflagration wave is subsonic with respect to the isentropic sound speed, $c^2 = -V^2 \left(\frac{\partial P}{\partial V}\right)_{S,\lambda}$; *i.e.*, $D - u_1 < c_1$. However, in contrast to a shock wave, the ahead state of a weak deflagration is also subsonic; *i.e.*, $D < c_0$. With respect to the isothermal sound speed, $c_T^2 = -V^2 \left(\frac{\partial P}{\partial V}\right)_{T,\lambda}$, the ahead state is typically subsonic as well. At $D = 0$, the behind state is subsonic with respect to the isothermal sound speed, But at the other extreme, the CJ condition implies that $(D - u) = c > c_T$. Hence, the CJ state is supersonic with respect to the isothermal sound speed. Therefore, with respect to the isothermal sound speed (wrt c_T), the behind state can be either subsonic or supersonic. This will play a role in some parts of our analysis.

The temperature of the behind state determines the reaction rate that drives the deflagration wave. For an exothermic reaction, $\Delta h < 0$, we later show that the constant pressure deflagration state has a temperature $T_{cp} > T_0$. Typically, on the deflagration locus, the temperature decreases as V increases. We assume the temperature at T_{cp} is sufficiently high that the deflagration temperature on the entire weak branch is always much larger than T_0; *i.e.*, the temperature increase from the heat release of the reaction greatly exceeds the cooling due to expansion. As with V, one might expect that the temperature would be monotonically increasing with λ on a deflagration profile. However, we later show that this is not necessarily true.

Remarks:

(i) A partly burned deflagration locus, with fixed $\lambda \in (0, 1)$, is defined in analogy to the deflagration locus by the equation

$$e_\lambda - e_0 = \tfrac{1}{2}\Big[P(V_\lambda, e_\lambda, \lambda) + P_0\Big] \cdot \Big[V_0 - V_\lambda\Big] \ . \tag{18}$$

Taking the derivative $\mathsf{d}/\mathsf{d}V$ and using Eq. (6) we find

$$-\left(\frac{\mathsf{d}P}{\mathsf{d}V}\right)_h = \frac{\gamma + \frac{\Gamma}{2}\left(\frac{P_0 - P}{P}\right)}{1 + \frac{\Gamma}{2}\left(\frac{V - V_0}{V}\right)} \cdot \frac{P}{V} \ . \tag{19}$$

On the deflagration locus $P < P_0$ and $V > V_0$. Since we are assuming $\Gamma > 0$, it follows that $(\mathsf{d}P/\mathsf{d}V)_h < 0$. Consequently, for fixed λ, the deflagration locus is a single valued function of either P or V. Moreover, in Appendix C we show that $(\partial e/\partial\lambda)_{V,P} < 0$. Hence, in the (V, P)-plane, the partly burned deflagration loci with different λ do not intersect. Typically, V_{CJ} and P_{CJ} are monotonic function of λ and they converge to (V_0, P_0) as $\lambda \to 0$. This implies that $D_{CJ}(\lambda) \to c_0$ as $\lambda \to 0$.

(ii) If the rate is so large that the estimated deflagration speed from Eq. (15) exceeds D_{cj}, then we anticipate that the reaction would generate a precursor shock to precondition the fluid state for a subsequent deflagration wave. Possibly this would lead to a detonation wave, which corresponds to a deflagration wave behind the lead shock to the CJ state; *i.e.*, a ZND profile.

(iii) Since shock waves are compressive, some hydro codes that use artificial viscosity to supply the numerical dissipation needed for shock capturing, set $Q = 0$ in expansion; *i.e.*, $\frac{\mathsf{d}}{\mathsf{d}\zeta}u > 0$. This has the effect of turning off viscosity in a deflagration wave profile.

(iv) In the limit of zero viscosity, Eq. (11a) reduces to the equation for the Rayleigh line

$$\widetilde{P}(V,T,\lambda) = P_0 - m^2(V - V_0) \ . \tag{20}$$

This determines V as function of T and λ. Alternatively, taking the derivative of the Rayleigh line equation leads to

$$\Big[(\rho\, c_T)^2 - m^2\Big]\frac{\mathsf{d}}{\mathsf{d}\xi}V = \rho\,\Gamma\, C_V\,\frac{\mathsf{d}}{\mathsf{d}\xi}T + (\partial_\lambda \widetilde{P})_{V,T}\,\frac{\mathsf{d}}{\mathsf{d}\xi}\lambda \ . \tag{21}$$

This equation for $\frac{\mathsf{d}}{\mathsf{d}\xi}V$ is singular at a sonic point wrt c_T. Similar consideration can be applied to the wave profile of a shock wave when heat conduction is the only dissipative mechanism. The result (due to Rayleigh [1910]) is that heat conduction is only sufficient to generate a smooth wave profile for weak shocks. As a consequence, for a detonation wave, viscosity is necessary for the lead shock profile that precedes the deflagration wave.

(v) It follows from the triple-shock rule (see [Menikoff and Plohr, 1989, Prop. 5.5]) that for a given wave speed the weak and strong deflagration states satisfy the Hugoniot jump conditions for the products EOS. Moreover, since we are assuming that the products EOS is convex and that the Grüneisen coefficient is positive, it follows that $T_w > T_s$ and $S_{cj} > S_w > S_s$. Furthermore, from the analysis of Gilbarg [1951], with $Pr > 0$ there is a shock profile from the strong to the weak deflagration states.

4.2 Reaction rate

We shall assume an Arrhenius reaction rate

$$\mathcal{R}(T,\lambda) = (1-\lambda)\, Z\, \exp(-T_a/T) \ , \tag{22}$$

where Z is the frequency factor (dimensions inverse time) and T_a is the activation temperature. To circumvent the 'cold boundary' problem ($\mathcal{R} > 0$ at $\lambda = 0$ for all $T > 0$) we modify the rate by introducing a cutoff temperature, $T_{\rm ign}$; *i.e.*,

$$\check{\mathcal{R}}(T,\lambda) = \begin{cases} (1-\lambda)\, Z\, \Big[\exp(-T_a/T) - \exp(-T_a/T_{\rm ign})\Big], & \text{for } T > T_{\rm ign}; \\ 0\,, & \text{for } T \le T_{\rm ign}. \end{cases} \tag{23}$$

The cutoff temperature, $T_{\rm ign}$, is often referred to as the 'ignition' temperature.

A zero rate at the ahead state simplifies the boundary conditions for the wave profile ODEs and allows a critical point analysis for the admissible deflagration waves. Typically, $T_0 \lesssim T_{\text{ign}} \ll T_1 \ll T_a$, and the rate at the ahead state is very small compared to the peak value in a deflagration wave profile, which occurs near the behind state. Consequently, the cutoff has a negligible affect on a deflagration wave.

5 Critical points

The ODEs for the deflagration profile consist of a system of 3 equations linear in the derivatives. For a steady wave, 3 condition are needed to specify the ahead state and another 3 for the behind state. If the ODEs were regular, only three initial conditions could be specified. With the modified rate, both the ahead and behind states are critical points for which the right hand side of Eq. (14) vanishes. Hence, a deflagration wave profile corresponds to a heteroclinic orbit.

We show in the following sections that the ratio of the derivatives $\frac{\mathsf{d}}{\mathsf{d}\xi}V : \frac{\mathsf{d}}{\mathsf{d}\xi}T : \frac{\mathsf{d}}{\mathsf{d}\xi}\lambda$ at the critical points provides two independent extra conditions, and the choice of the parameter m provides the third condition. Thus, the existence of a heteroclinic orbit depends on the mass flux parameter m. For a given ahead state, it determines the allowable steady state deflagration speed D corresponding to a point on the deflagration locus. Physically, a deflagration profile can only occur when the heat flux, which is directed from the behind state to the ahead state, is compatible with the mass flux, which is directed from the ahead state to the behind state. Consequently, the deflagration speed depends on the coefficient of thermal conduction. More precisely, the trajectories of Eq. (14) depend on $\kappa\,\mathcal{R}$, Pr and m. For a given ahead state and fixed Pr, the deflagration wave speed will be invariant if κ and $\mathcal{R}$ are scaled by inverse factors.

For a shock wave, the nature of the critical points has been analyzed by Weyl [1949]. Next we extend the analysis to reactive flow. About a critical point (V_c, T_c, λ_c), expanding the ODEs, Eq. (14), to first order leads to the linear system

$$\frac{\mathsf{d}}{\mathsf{d}\zeta}\begin{pmatrix}\hat{V}\\ \hat{T}\\ \hat{\lambda}\end{pmatrix} = -\,\mathbf{A}\begin{pmatrix}\hat{V}\\ \hat{T}\\ \hat{\lambda}\end{pmatrix}\ , \tag{24}$$

where $\hat{V} = (V - V_c)/V_c$, $\hat{T} = (T - T_c)/T_c$ and $\hat{\lambda} = \lambda - \lambda_c$. The coefficient matrix can be written as

$$\mathbf{A} = \begin{pmatrix} & & a_1 \\ \mathbf{A}_{\rm nr} & & a_2 \\ r_1 & r_2 & r_3 \end{pmatrix} . \tag{25}$$

The non-reactive sub-matrix is

$$\mathbf{A}_{\rm nr} = \begin{pmatrix} \frac{1}{Pr\, m^2}\left[m^2 - \rho\, K_T\right] & \frac{1}{Pr\, m^2}\,\Gamma\,\rho^2\, C_V\, T \\ \frac{1}{C_r}\,\Gamma\, C_V & \frac{1}{C_r}\, C_V \end{pmatrix} , \tag{26}$$

where $K_T = -V\,(\partial_V \widetilde{P})_{T,\lambda} = \rho\, c_T^2$ is the isothermal bulk modulus and c_T the isothermal sound speed, $\Gamma = V(\partial_e P)_{V,\lambda}$ is the Grüneisen coefficient, and $C_V = (\partial_T e)_{V,\lambda}$ is the specific heat at constant volume.

The additional matrix coefficient for V and T are

$$a_1 = \frac{\rho}{Pr\, m^2}\left(\frac{\partial \widetilde{P}}{\partial \lambda}\right)_{V,T} , \tag{27a}$$

$$a_2 = \frac{1}{C_r\, T}\left(\frac{\partial e}{\partial \lambda}\right)_{V,T} . \tag{27b}$$

For an equilibrium mixture EOS, the partial derivatives, $(\partial_\lambda \widetilde{P})_{V,T}$ and $(\partial_\lambda e)_{V,T}$, are derived in App. C. We note that $a_1 > 0$ and $a_2 < 0$.

Based on the modified rate, Eq. (23), the matrix coefficients for λ are

$$\begin{aligned} r_1 &= \frac{\ell}{m}\, V \frac{\partial}{\partial V}\left(\check{\mathcal{R}}/V\right)_{T,\lambda} \\ &= -\frac{\ell\, Z}{m\, V}\,(1-\lambda)\left[\exp(-T_a/T) - \exp(-T_a/T_{\rm ign})\right] , \end{aligned} \tag{28a}$$

$$\begin{aligned} r_2 &= \frac{\ell}{m\, V}\, T\left(\frac{\partial}{\partial T}\check{\mathcal{R}}\right)_{V,\lambda} \\ &= \frac{\ell\, Z}{m\, V}\,(1-\lambda)\,\frac{T_a}{T}\exp(-T_a/T) , \end{aligned} \tag{28b}$$

$$
\begin{aligned}
r_3 &= \frac{\ell}{m\,V}\left(\frac{\partial}{\partial\lambda}\check{\mathcal{R}}\right)_{V,T} \\
&= -\frac{\ell\,Z}{m\,V}\left[\exp(-T_a/T) - \exp(-T_a/T_{\text{ign}})\right] \,, \qquad (28c)
\end{aligned}
$$

for $T \geq T_{\text{ign}}$, and $r_1 = r_2 = r_3 = 0$ for $T < T_{\text{ign}}$. Clearly, for $T_{\text{ign}} > T_0$, $r_i = 0$ at the ahead state. However, $r_2 > 0$ at the ahead state when $T_{\text{ign}} = T_0$.

The eigenvalues of $\mathbf{A}_{\text{nr}}$ play a key role in the critical point analysis. From Eq. (26) and the thermodynamic identity, $c^2 = c_T^2 + \Gamma^2\,C_V\,T$, we obtain

$$
\det \mathbf{A}_{\text{nr}} = \frac{1}{Pr\,m^2}\,\frac{C_V}{C_r}\left[m^2 - (\rho\,c)^2\right] \,, \qquad (29)
$$

where c is the isentropic sound speed. Moreover, the discriminant of the eigenvalue equation,

$$
\det[\mathbf{A}_{\text{nr}} - \alpha\mathbb{I}] = \alpha^2 - [\mathsf{Tr}\,\mathbf{A}_{\text{nr}}]\,\alpha + \det \mathbf{A}_{\text{nr}} = 0 \,, \qquad (30)
$$

can be written as

$$
\begin{aligned}
[\mathsf{Tr}\,\mathbf{A}_{\text{nr}}]^2 - 4\,\det \mathbf{A}_{\text{nr}} &= \left[\frac{m^2 - \rho\,K_T}{Pr\,m^2} + \frac{C_V}{C_r}\right]^2 - \frac{4}{Pr\,m^2}\,\frac{C_V}{C_r}\left[m^2 - (\rho\,c)^2\right] \\
&= \left[\frac{m^2 - \rho\,K_T}{Pr\,m^2} - \frac{C_V}{C_r}\right]^2 + \frac{4}{Pr\,m^2}\,\frac{C_V}{C_r}\left[(\rho\,c)^2 - (\rho\,c_T)^2\right] \\
&= \left[\frac{m^2 - \rho\,K_T}{Pr\,m^2} - \frac{C_V}{C_r}\right]^2 + \frac{4}{Pr\,m^2}\,\frac{C_V}{C_r}\,(\rho\,\Gamma)^2 C_V\,T \\
&> 0 \,.
\end{aligned}
$$

Consequently, the eigenvalues are real. Moreover, at a subsonic critical point ($D - u < c$), the determinant is negative. Hence, one eigenvalue is positive and the other is negative. This is the case for both the ahead and the behind states of a weak deflagration wave.

For the reactive case, at the behind state ($\lambda = 1$), r_1 and r_2 are both 0. Therefore, the matrix $\mathbf{A}$ has two eigenvalues corresponding to those of $\mathbf{A}_{\text{nr}}$, and the third eigenvalue is $r_3 < 0$. Hence, for $-\mathbf{A}$, two eigenvalues are positive and one is negative. Therefore, for Eq. (14), the critical point at $\zeta = -\infty$ has a two-dimensional stable manifold and a one-dimensional unstable manifold. Moreover, for the estimated deflagration speed of Eq. (15), $|r_3| = \mathcal{O}\,(1)$.

For now we assume that T_{ign} is slightly greater than T_0. Then at the ahead state ($\lambda = 0$), $r_1 = r_2 = r_3 = 0$. Consequently, the matrix $\mathbf{A}$ has one positive eigenvalue, one negative eigenvalue, and the third is zero. In phase space, the wave profile at the ahead state must have a slope $\frac{\mathsf{d}T}{\mathsf{d}V}$ determined by the eigenfunction of $\mathbf{A}_{\text{nr}}$ corresponding to the positive eigenvalue (which is a negative eigenvalue of $-\mathbf{A}$); *i.e.*, the profile must lie on the stable manifold of the critical point at $\zeta = \infty$. As we will see in the example below, $\frac{\mathsf{d}T}{\mathsf{d}V} > 0$.

With $T_{\text{ign}} = T_0$, we later show that the third eigenvalue of $\mathbf{A}$ is nearly zero but positive. The simple counting argument would then suggest that there are enough degrees of freedom for a heteroclinic orbit to exist for any m. However, as later discussed in detail, due to the phase space constraint, $\lambda \geq 0$, the third eigenvalue does not provide the necessary degree of freedom. Consequently, the behavior is as described for the case $T_{\text{ign}} > T_0$. There are no degrees of freedom associated with the critical point at the ahead state, and the parameter m provides the remaining degree of freedom needed to obtain a heteroclinic orbit.

It is instructive to work out the eigenvalues and eigenvectors of $\mathbf{A}_{\text{nr}}$ for an ideal explosive EOS (see App. A);

$$P\,V = (\gamma - 1)(e + \lambda Q) \quad \text{and} \quad T = C_V\,(e + \lambda Q)\ .$$

Assuming $Pr = \mathcal{O}\,(1)$, a weak deflagration wave ($m \ll 1$) and $C_r = C_V$, it can be shown that

$$\mathsf{Tr}\,\mathbf{A}_{\text{nr}} \approx -[{M_T}^2 Pr]^{-1}\ ,$$

where $M_T = D/c_T \ll 1$ is the isothermal Mach number, and

$$\det \mathbf{A}_{\text{nr}} \approx -[M^2 Pr]^{-1}\ ,$$

where $M = D/c \ll 1$ is the isentropic Mach number. For an ideal gas EOS, $c^2 = \gamma\,P\,V$ and ${c_T}^2 = P\,V$. Hence, $\det \mathbf{A}_{\text{nr}} \approx \gamma\,\mathsf{Tr}\,\mathbf{A}_{\text{nr}}$. Moreover, both $\mathsf{Tr}\,\mathbf{A}_{\text{nr}}$ and $\det \mathbf{A}_{\text{nr}}$ are negative and large in magnitude. It then follows that the eigenvalues of $\mathbf{A}_{\text{nr}}$ are $\alpha \approx -Pr^{-1}(c_T/D)^2$ and γ. Consequently, the negative eigenvalue is very large in magnitude and the positive eigenvalue is order 1.

The eigenvectors can be expressed as $(1,\, x)$ where $x = \frac{V\Delta T}{T\Delta V}$. Then it is easy to show that $x = \Gamma/(\alpha - 1)$. Hence, the slope of the eigenvectors are

given by

$$\frac{\Delta T/T}{\Delta V/V} = \begin{cases} \frac{\Gamma}{\gamma-1} & \text{for } \alpha = \gamma \ , \\ -\frac{\Gamma\, Pr}{1+(D/c_T)^2 Pr} \cdot \left(\frac{D}{c_T}\right)^2 & \text{for } \alpha = -Pr^{-1}(c_T/D)^2 \ . \end{cases}$$

Thus, the eigenvector for the positive eigenvalue has positive slope while the negative eigenvector has a negative slope of small magnitude. In general, for small m, the same formulae hold but with γ replaced by $(c/c_T)^2$. For a solid EOS, $c/c_T \gtrsim 1$, and the largest affect is on the slope for the positive eigenvalue which is then proportional to $\frac{1}{1-(c_T/c)^2}$ and can be quite large.

Remarks:

(i) For a detonation wave, the ahead state is supersonic. Consequently, there is one degree of freedom associated with the derivatives at the ahead state, and the mass flux is not needed as an additional degree of freedom. As a result, one expects that a wave profile would exist for any point on the strong branch of the detonation locus.

(ii) The critical points imply that the wave profile has an exponential tail leading to the ahead and behind states. The exponential tail at the behind state is affected by the depletion factor of the reaction rate. For a heterogeneous reactive solid, such as a PBX, the rate is often taken as $\mathcal{R} \propto (1-\lambda)^n$ with $n < 1$. (We note in this case that the λ factor accounts for the dependence of the burn front area from hot spots and not to a chemical reaction order.) One consequence of $n < 1$ is that the reaction length in the approach to the behind state is finite; since

$$\Delta\zeta = \int_\lambda^1 \frac{\mathsf{d}\lambda}{\mathcal{R}(\lambda)} = 1 - \frac{(1-\lambda)^{1-n}}{1-n} \ ,$$

rather than $\Delta\zeta = -\ln(1-\lambda)$ if $n = 1$. Another consequence is that a component of the matrix $\mathbf{A}$, $r_3 \propto (1-\lambda)^{-(1-n)}$, is singular at the behind state. This requires the critical point analysis of the ODEs to be modified. The result is that the reaction completes ($\lambda = 1$) before (V, T) reaches the behind state, and the wave profile ends with a non-reactive tail. The eigenvalues of $\mathbf{A}_{\rm nr}$ still determines the behavior of the ODEs at the behind state. We also note that with an ignition temperature above the initial temperature, the exponential tail to the ahead state is non-reactive.

(iii) In the more general context of non-steady reactive fluid flow, the exponential tails of the wave profiles can be viewed as part of a matched asymptotic expansion for a transition layer; see for example Garbey [1994]. The wave profile represent the inner solution in which flow gradients are large, and consequently heat conduction and viscosity play a dominant role. The profile is matched to an outer solution in which gradients are sufficiently small, such that heat conduction and viscosity may be neglected. The matching conditions for the inner and outer solution are the end states of the wave profile. The matching is a good approximation provided that the wave profile is quasi-steady; *i.e.*, the end states vary slowly on the time scale for a particle to transit through the wave profile.

6 Perturbative approach

If the thermal diffusion coefficient and deflagration speed are such that the scaled rate in Eq. (14c) is small, $\frac{\ell}{mV}\mathcal{R} \ll 1$, then Eq. (16) applies. Moreover, if ν and κ are small, then we anticipate that the right hand sides of Eq. (16a) and Eq. (16b) would be small. This occurs for the deflagration profile following the lead shock in a detonation wave when $\tilde{\ell} \gg \ell$, *i.e.*, the reaction zone width ($D\tau$) is much greater than the length scale for heat conduction (k/D). The conditions may also apply to a quasi-steady deflagration wave generated by a hot spot or during a transient leading to a shock-to-detonation transition.

In this case, the deflagration profile projected onto the (V, P)-plane will lie close to the intersection of the Rayleigh line, Eq. (20), and the partly burned Hugoniot locus, Eq. (18). This can lead to large round-off errors when numerically integrating the ODEs, Eq. (16), with realistic equations of state. Consequently, it is advantageous to employ a perturbative approach based on the deflagration profile without viscosity and heat conduction.

6.1 Unperturbed wave profile

We take the unperturbed profile as the solution of the algebraic equations for the partly burned Hugoniot locus and the Rayleigh line, Eq. (18) and Eq. (20), corresponding to mass flux m, and the ODE for the reaction

progress variable, Eq. (14c). The profile can be expressed as $\lambda_h(\zeta)$, $V_h \circ \lambda_h(\zeta)$, and $T_h \circ \lambda_h(\zeta)$. It is convenient to determine $V_h(\lambda)$ and $T_h(\lambda)$ as the solution to a pair of ODEs rather than solving the algebraic equations for the intersection of the partly burned Hugoniot locus and the Rayleigh line. After determining V_h and T_h, the right hand side of the rate equation (14c) is a function of only λ. Hence, $\lambda_h(\zeta)$ is the solution of a single ODE.

The ODEs for V_h and T_h can be derived as follows. Taking the derivative, $\frac{\mathsf{d}}{\mathsf{d}\lambda}$, of Eq. (20) and Eq. (18) leads to the equations

$$\begin{aligned}
\frac{\mathsf{d}}{\mathsf{d}\lambda} P &= \left(\partial_V \widetilde{P}\right) \frac{\mathsf{d}}{\mathsf{d}\lambda} V + \left(\partial_T \widetilde{P}\right) \frac{\mathsf{d}}{\mathsf{d}\lambda} T + \partial_\lambda \widetilde{P} \\
&= -m^2 \frac{\mathsf{d}}{\mathsf{d}\lambda} V \ , \\
\frac{\mathsf{d}}{\mathsf{d}\lambda} e &= \left(\partial_V e\right) \frac{\mathsf{d}}{\mathsf{d}\lambda} V + \left(\partial_T e\right) \frac{\mathsf{d}}{\mathsf{d}\lambda} T + \partial_\lambda e \\
&= \tfrac{1}{2}\left(V_0 - V\right) \frac{\mathsf{d}}{\mathsf{d}\lambda} P - \tfrac{1}{2}\left(\widetilde{P} + P_0\right) \frac{\mathsf{d}}{\mathsf{d}\lambda} V \\
&= -\widetilde{P} \frac{\mathsf{d}}{\mathsf{d}\lambda} V \ .
\end{aligned}$$

This can be re-expressed as a system of 2 ODEs

$$\begin{pmatrix} m^2 - (\rho\, c_T)^2 & \frac{\Gamma}{V}\, C_V \\ \frac{\Gamma}{V}\, C_V\, T & C_V \end{pmatrix} \begin{pmatrix} \frac{\mathsf{d}}{\mathsf{d}\lambda} V \\ \frac{\mathsf{d}}{\mathsf{d}\lambda} T \end{pmatrix} = - \begin{pmatrix} \partial_\lambda \widetilde{P} \\ \partial_\lambda e \end{pmatrix} \ . \tag{31}$$

Equivalently, by scaling the equations, we obtain

$$\begin{pmatrix} \frac{1}{V} \frac{\mathsf{d}}{\mathsf{d}\lambda} V \\ \frac{1}{T} \frac{\mathsf{d}}{\mathsf{d}\lambda} T \end{pmatrix} = - \mathbf{A}_{\text{nr}}^{-1} \begin{pmatrix} \frac{\rho}{Pr\, m^2}\, \partial_\lambda \widetilde{P} \\ \frac{1}{C_r\, T}\, \partial_\lambda e \end{pmatrix} \ , \tag{32}$$

where $\mathbf{A}_{\text{nr}}$ is the same matrix as for a non-reactive critical point, Eq. (26). In fact, this analysis provides a derivation of the matrix $\mathbf{A}_{\text{nr}}$. In addition, we note that the vector on the right hand side of Eq. (32) is $[a_1, a_2]^T$, *i.e.*, components of matrix $\mathbf{A}$, Eq. (25).

By Eq. (29), $\det \mathbf{A}_{\rm nr}$ only vanishes at a sonic point; *i.e.*, the CJ state. Hence, the matrix $\mathbf{A}_{\rm nr}$ is invertible. The trajectory of the ODEs (32) starting at the ahead state ($\lambda = 0$) determines the functions $V_h(\lambda)$ and $T_h(\lambda)$. The ODEs can be written explicitly as

$$\frac{\mathsf{d}}{\mathsf{d}\lambda} V = \frac{\partial_\lambda \widetilde{P} - (\Gamma/V)\, \partial_\lambda e}{(\rho\, c)^2 - m^2} \ , \tag{33a}$$

$$\frac{\mathsf{d}}{\mathsf{d}\lambda} T = \frac{-[(\rho\, c_T)^2 - m^2]\, \partial_\lambda e / C_V - (\Gamma/V)\, T\, \partial_\lambda \widetilde{P}}{(\rho\, c)^2 - m^2} \ . \tag{33b}$$

From Appendix C, $\partial_\lambda \widetilde{P} > 0$ and $\partial_\lambda e < 0$. Hence, for subsonic flow ($m < \rho\, c$), V_h is a monotonically increasing function of λ, but T_h may either increase or decrease. If in addition the flow is supersonic wrt c_T ($\rho\, c_T < m$), as occurs near the CJ state, then T_h decreases with increasing λ.

Typically, $m \ll \rho\, c_T$ and the flow is subsonic wrt c_T. Using the thermodynamic relations in Appendix C, Eq. (33b) can be reduced for small m to

$$\frac{\mathsf{d}}{\mathsf{d}\lambda} T = -\left(\frac{c_T}{c}\right)^2 \cdot \frac{h_p - h_r}{C_V} + \mathcal{O}\left(m^2\right) \ .$$

For an exothermic reaction $h_p - h_r < 0$. In this case, T_h is a monotonically increasing function of λ. The average value can be used as a rough estimate for the derivative, *i.e.*, $\frac{\mathsf{d}}{\mathsf{d}\lambda} T_h \approx T_1 - T_0$.

The reaction progress variable, $\lambda_h(\zeta)$, is then the solution to the ODE

$$\frac{\mathsf{d}}{\mathsf{d}\zeta} \lambda = -\left[\frac{\ell\, \mathcal{R}_h(\lambda)}{m\, V_h(\lambda)}\right] \ , \tag{34}$$

where $\mathcal{R}_h(\lambda) = \mathcal{R}(V_h(\lambda), T_h(\lambda), \lambda)$. As previously noted, the unperturbed wave profile is given by $\widetilde{V}_h(\zeta) = V_h \circ \lambda_h(\zeta)$ and $\widetilde{T}_h(\zeta) = T_h \circ \lambda_h(\zeta)$. Later, we use $\widetilde{\mathcal{R}}_h(\zeta) = \mathcal{R}_h \circ \lambda_h(\zeta)$.

Remarks:

(i) Due to inaccuracies in calculating thermodynamic derivatives and the divergence of ODE trajectories, the numerical solution of the ODEs (33) may not give sufficiently accurate solutions to the equations for the Rayleigh line and Hugoniot locus. One way to improve the accuracy is to add a relaxation

term on the right hand side of Eq. (33). This can be done by substituting for the derivatives

$$\partial_\lambda \widetilde{P} \to \partial_\lambda \widetilde{P} + f * \Delta P \ ,$$
$$\partial_\lambda e \to \partial_\lambda e + f * \Delta e \ ,$$

where f is a convergence factor (typically, 1 to 100 depending on step size $\Delta\lambda$ used for the numerical integration), and

$$\Delta P = \widetilde{P}(V,T,\lambda) - [P_0 + m^2\,(V_0 - V)] \ ,$$
$$\Delta e = e(V,T,\lambda) - [e_0 + \tfrac{1}{2}(\widetilde{P}(V,T,\lambda)(V_0 - V)] \ .$$

Alternatively, the numerical solution of the ODEs can be corrected after the integration with a few Newton-Raphson iteration steps. The derivative matrix needed for the Newton-Raphson iteration has the same components as the coefficients of the derivatives ($\partial_\lambda \widetilde{P}$ and $\partial_\lambda e$) on the right hand side of Eq. (33). Thus, in effect, the relaxation terms in the ODE represent a continuous form of a Newton-Raphson iteration.

(ii) At the CJ state, $m^2 = (\rho\, c)^2$. The ODEs (33) for the CJ profile are singular at $\lambda = 1$; both $\frac{\mathrm{d}}{\mathrm{d}\lambda} V$ and $\frac{\mathrm{d}}{\mathrm{d}\lambda} T$ blow up as $(1-\lambda)^{-1/2}$. This is a consequence of the tangency condition in the (V,P)–plane for the deflagration locus and the Rayleigh line at the CJ state. We note that the singularity is integrable.

(iii) For an ideal explosive EOS (see Appendix A), $\partial_\lambda \widetilde{P} = 0$. Consequently, as λ increases, T_h is monotonically increasing on portions of the profile for which the flow is subsonic wrt c_T ($\rho\, c > \rho\, c_T > m$) and monotonically decreasing when the flow is supersonic wrt c_T. This is an example of a simplification for an ideal EOS that is not necessarily true for a realistic explosive EOS.

(iv) On the strong branch of the deflagration locus

$$m^2 - (\rho\, c_T)^2 > m^2 - (\rho\, c)^2 > 0 \ .$$

Since $\partial_\lambda \widetilde{P} > 0$ and $\partial_\lambda e < 0$, it follows from Eq. (33) that $\frac{\mathrm{d}}{\mathrm{d}\lambda} V < 0$ and $\frac{\mathrm{d}}{\mathrm{d}\lambda} T > 0$; *i.e.*, T decreases as V increases. The typical case of the loci $\Big(V_h(\lambda),\, T_h(\lambda)\Big)$ are shown in Fig. 2 as the dashed and dotted magenta curves for the weak and strong branches, respectively.

(v) On the profile, $\mathsf{d}e = -P\mathsf{d}V$. It then follows from the thermodynamic identity Eq. (3) that $T\mathsf{d}S = -(\Delta G)\mathsf{d}\lambda$. Since $\Delta G < 0$, the entropy increases as λ increases. Hence, on the weak branch, entropy is monotonically increasing with V.

As an aside, we are now in a position to determine the eigenvalues of the critical point matrix, Eq. (25), at the ahead state ($\lambda = 0$) when $T_{\rm ign} = T_0$. In this case

$$\mathbf{A} = \begin{pmatrix} & & a_1 \\ \mathbf{A}_{\rm nr} & & a_2 \\ 0 & r_2 & 0 \end{pmatrix} \ . \tag{35}$$

Evaluating the rate coefficient, Eq. (28), using Eq. (15) to estimate m, we find that $r_2 \approx (T_a/T_0)\exp[-T_a/T_0+T_a/T_1]$ is very small when $T_0 \ll T_1 \ll T_a$. Let α_1 and α_2 be the eigenvalues of $\mathbf{A}_{\rm nr}$. The eigenvalue equation for $\mathbf{A}$ can be expressed as

$$\alpha\Big[(\alpha-\alpha_1)(\alpha-\alpha_2) - a_2\, r_2\Big] = [a_1 A_{21} - a_2 A_{11}]\, r_2 \ . \tag{36}$$

To leading order in r_2, the three roots are α_1, α_2 and

$$\alpha_3 = \frac{a_1 A_{21} - a_2 A_{11}}{\alpha_1 \alpha_2}\, r_2 \ . \tag{37}$$

This can be simplified as follows. Using Eqs. (26), (27) and (33b), we obtain for the numerator

$$\begin{aligned} a_1 A_{21} - a_2 A_{11} &= \frac{1}{Pr\, m^2}\left[\frac{\partial \widetilde{P}}{\partial \lambda}\cdot\frac{\Gamma}{V}\frac{C_V}{C_r} + \frac{\partial e}{\partial \lambda}\cdot\frac{(\rho c_T)^2 - m^2}{C_r\, T}\right] \\ &= -\frac{(\rho c)^2 - m^2}{\mathrm{Pr}\ m^2}\cdot\frac{C_V}{T_h\, C_r}\cdot\frac{\mathsf{d}}{\mathsf{d}\lambda}T_h \ . \end{aligned}$$

The denominator is $\alpha_1\alpha_2 = \det \mathbf{A}_{\rm nr}$, which is given by Eq. (29). Combining these results, the third eigenvalue is

$$\alpha_3 = \frac{r_2}{T_h}\,\frac{\mathsf{d}}{\mathsf{d}\lambda}T_h \ . \tag{38}$$

Therefore, the sign of α_3 is the same as the sign of $\frac{\mathsf{d}}{\mathsf{d}\lambda}T_h$. Typically, this is positive. Consequently, the third eigenvalue of $\mathbf{A}$ is $\alpha_3 > 0$ and very small. Also to leading order in r_2, it follows from Eq. (35) and Eq. (32) that the third eigenfunction is $(V_h^{-1}\frac{\mathsf{d}}{\mathsf{d}\lambda}V_h,\, T_h^{-1}\frac{\mathsf{d}}{\mathsf{d}\lambda}T_h,\, 1)^T$.

6.2 Transformed variables

We define the parameter $\epsilon = \ell/\tilde{\ell}$. The transformation

$$V(\zeta) = V_h \circ \lambda_h(\zeta) \left[1 + \epsilon \hat{V}(\zeta)\right] , \tag{39a}$$

$$T(\zeta) = T_h \circ \lambda_h(\zeta) \left[1 + \epsilon \hat{T}(\zeta)\right] , \tag{39b}$$

$$\lambda(\zeta) = \lambda_h(\zeta) + \epsilon \hat{\lambda}(\zeta) , \tag{39c}$$

defines the dimensionless variables $\hat{V}$ and $\hat{T}$ and $\hat{\lambda}$.

As noted previous, ϵ is small when the reaction zone width is much greater than the length scale for heat conduction. In addition, for small coefficients of heat conduction and viscosity, we expect that the transformed variables $\hat{V}$, $\hat{T}$ and $\hat{\lambda}$ all to be $\mathcal{O}(1)$. Consequently, we can expand the ODEs for the wave profile, Eq. (14), in ϵ to derive equations for the transformed variables. The expansion is facilitated by the fact that (V_h, T_h, λ_h) is a critical point for the thermodynamic part of the wave profile ODEs, *i.e.*, Eqs. (14a) and (14b).

In some respects, the expansion provides an alternative to the singular perturbation approach of Gasser and Szmolyan [1993]. However, the focus here is on providing a framework in which the deflagration speed can be computed rather than on an existence proof of a wave profile.

6.3 Transformed equations

To derive the equations for the transformed variable, we evaluate the derivatives in two ways. Taking $\frac{\mathsf{d}}{\mathsf{d}\zeta}$ of Eq. (39) we obtain

$$\frac{\mathsf{d}}{\mathsf{d}\zeta} V = \left[1 + \epsilon \hat{V}(\zeta)\right] V_h' \circ \lambda_h(\zeta) \frac{\mathsf{d}}{\mathsf{d}\zeta} \lambda_h + V_h \circ \lambda_h(\zeta)\, \epsilon \frac{\mathsf{d}}{\mathsf{d}\zeta} \hat{V} ,$$

$$\frac{\mathsf{d}}{\mathsf{d}\zeta} T = \left[1 + \epsilon \hat{T}(\zeta)\right] T_h' \circ \lambda_h(\zeta) \frac{\mathsf{d}}{\mathsf{d}\zeta} \lambda_h + T_h \circ \lambda_h(\zeta)\, \epsilon \frac{\mathsf{d}}{\mathsf{d}\zeta} \hat{T} ,$$

$$\frac{\mathsf{d}}{\mathsf{d}\zeta} \lambda = \frac{\mathsf{d}}{\mathsf{d}\zeta} \lambda_h + \epsilon \frac{\mathsf{d}}{\mathsf{d}\zeta} \hat{\lambda} ,$$

where $V_h'(\lambda) = \frac{\mathsf{d}}{\mathsf{d}\lambda} V_h$, $T_h'(\lambda) = \frac{\mathsf{d}}{\mathsf{d}\lambda} T_h$, and $\frac{\mathsf{d}}{\mathsf{d}\zeta}\lambda_h$ is given by Eq. (34). Expanding the right hand side of Eq. (14) to first order in ϵ yields

$$V_h^{-1} \frac{\mathsf{d}}{\mathsf{d}\zeta} V = -\epsilon \vec{A}_1 \cdot (\hat{V}, \hat{T}, \hat{\lambda})^T ,$$

$$T_h^{-1}\frac{\mathsf{d}}{\mathsf{d}\zeta}T = -\epsilon\,\vec{A}_2\cdot(\hat{V},\hat{T},\hat{\lambda})^T\ ,$$
$$\frac{\mathsf{d}}{\mathsf{d}\zeta}\lambda = -\frac{\ell\,\widetilde{\mathcal{R}}_h}{m\,\widetilde{V}_h} + \epsilon\,\vec{A}_3\cdot(\hat{V},\hat{T},\hat{\lambda})^T\ ,$$

where $\vec{A}_i$ denotes the i^{th} row of the matrix $\mathbf{A}$, Eqs. (25–28).

Combining the two sets of equations, we obtain to leading order in ϵ the ODEs for the transformed variables:

$$\frac{\mathsf{d}}{\mathsf{d}\zeta}\begin{pmatrix}\hat{V}\\ \hat{T}\\ \hat{\lambda}\end{pmatrix} = -\mathbf{A}(\zeta)\begin{pmatrix}\hat{V}\\ \hat{T}\\ \hat{\lambda}\end{pmatrix} + \frac{\ell\,\widetilde{\mathcal{R}}_h}{\epsilon\,m\,\widetilde{V}_h}\begin{pmatrix}V_h'\circ\lambda_h/\widetilde{V}_h\\ T_h'\circ\lambda_h/\widetilde{T}_h\\ 0\end{pmatrix}\ , \tag{40}$$

where the matrix $\mathbf{A}(\zeta)$ is evaluated at $(\widetilde{V}_h,\widetilde{T}_h,\lambda_h)$. We note that V_h' and T_h' are given explicitly by Eq. (33). Moreover, the singular looking factor $\frac{\ell\,\widetilde{\mathcal{R}}_h}{\epsilon\,m\,V_h} = \frac{V_0}{V_h}\,\tau\,\widetilde{\mathcal{R}}_h$ is actually $\mathcal{O}(1)$ since τ is approximately the inverse of the maximum rate.

The boundary conditions for a deflagration wave profile are that $\hat{V}$, $\hat{T}$ and $\hat{\lambda}$ vanish at both end states. The second term on the right hand side of Eq. (40) or source term is proportional to the rate. When the rate vanishes at the end states, they behave like critical points. This always occurs at the behind state, but not at the ahead state for the deflagration portion of a ZND detonation. Since the eigenvalues of $\mathbf{A}$ are both positive and negative, Eq. (40) is not a system of relaxation type equations.

For a ZND detonation wave, a deflagration profile is possible because of the degree of freedom to set the derivatives behind the lead shock. For the standard case in which the derivative vanish at the ahead state, a solution would only exist for a particular choice of the mass flux that enters into the matrix $\mathbf{A}$. However, when $\ell/\tilde{\ell}$ is not small, numerical examples show that T can exceed T_h along a portion of the wave profile by a significant amount, and the underlying assumption of the expansion breaks down. Consequently, this perturbation approach is only useful for the deflagration portion of a ZND detonation.

We note that $\frac{\mathsf{d}}{\mathsf{d}\zeta} = \epsilon\,\frac{\mathsf{d}}{\mathsf{d}z}$. Thus on the reaction length scale, Eq. (40) is a singular system of ODEs. If a solution exists then the right hand side must

be small. Hence,

$$\begin{pmatrix} \hat{V} \\ \hat{T} \\ \hat{\lambda} \end{pmatrix} = \frac{V_0}{V_h}\,\tau\,\widetilde{\mathcal{R}}_h\,\mathbf{A}^{-1}(\zeta)\begin{pmatrix} V_h' \circ \lambda_h/\widetilde{V}_h \\ T_h' \circ \lambda_h/\widetilde{T}_h \\ 0 \end{pmatrix} ,$$

can be thought of as the first order term in an asymptotic series in ϵ. The zeroth order term $(V_h,\, T_h,\, \lambda_h)$ implies that the appropriate boundary conditions for Eq. (40) at the ahead state are simply the derivatives along the Rayleigh line.

7 Phase-plane analysis

Determining an admissible deflagration wave requires finding the value of the mass flux m such that a solution trajectory of the wave profile ODEs exists between the ahead and behind states. To facilitate this, we analyze the vector field, or right hand side of Eq. (14), in the (V, T, λ)-phase plane. This allows us to characterize how the solution trajectories, for fixed m, vary with different initial conditions. Topological considerations of the general structure of the trajectories then will enable us to construct a numerical algorithm for finding an admissible deflagration wave. This is tantamount to an existence proof of an admissible deflagration wave.

We denote the ahead state with subscript 0, and the weak and strong deflagration states with subscripts w and s, respectively. Three families of curves in phase space play an important role in our analysis:

1. Let $\mathcal{H}_\lambda$ denote the zero level set of the Hugoniot function

$$h_\lambda(V,T) = e(V,T,\lambda) - e_0 + \tfrac{1}{2}\Big[\widetilde{P}(V,T,\lambda) + P_0\Big]\,(V - V_0)\ , \qquad (41)$$

i.e., $\mathcal{H}_\lambda$ is the partly burned Hugoniot locus based on the ahead state.

2. Let $\mathcal{L}_\lambda$ denote the image of the Rayleigh line, or locus of the equation

$$\widetilde{P}(V,T,\lambda) = P_{\mathcal{L}}(V) \equiv P_0 - m^2(V - V_0)\ . \qquad (42)$$

For fixed λ, $\frac{\mathsf{d}}{\mathsf{d}\zeta}V = 0$ on $\mathcal{L}_\lambda$.

3. Let $\mathcal{T}_\lambda$ be the zero level set of the function

$$T_\lambda(V,T) = e(V,T,\lambda) - e_0 + \tfrac{1}{2}[P_{\mathcal{L}}(V) + P_0]\cdot(V - V_0)\ . \tag{43}$$

For fixed λ, $\frac{\mathsf{d}}{\mathsf{d}\zeta}T = 0$ on $\mathcal{T}_\lambda$.
We note that the three curves are each single valued in V. Moreover, the union over λ of each curve family corresponds to a non-intersecting surface in the (V,T,λ)-phase plane.

We assume that a CJ state exists on the deflagration locus. Typically, it will also exist on all partially burned loci. Let $m_{\rm CJ}(\lambda)$ denote the CJ mass flux. It is a decreasing function of λ, which implies the locus of partially burned CJ states in the (V,P)-plane is a convex curve. The existence of the CJ state implies that the full weak branch of the deflagration locus exists for $0 < \lambda \leq 1$. (For $\lambda = 0$, the CJ state is the same as the ahead state, and the weak branch is degenerate.) The strong branch, however, terminates at a phase boundary; either $P = 0$ or $T = 0$. Consequently, for sufficiently small m there are no strong deflagrations. Hence, for some values of m there is a weak but not a strong deflagration. Since in the (V,P)-plane the partially burned deflagration loci are nested, if for a given m a strong deflagration $s(\lambda_2)$ does not exist then a strong state does not exist for any $\lambda_1 < \lambda_2$.

The intersection of $\mathcal{H}_\lambda$ and $\mathcal{L}_\lambda$ corresponds to points on the partially burned deflagration locus. There are at most two points for $m < m_{\rm CJ}(\lambda)$; states w and s. Points on the intersection can be parameterized by λ. We define the functions $V_h(\lambda)$ and $T_h(\lambda)$ as the specific volume and temperature on the intersection; see Eq. (33). There are distinct pairs of functions corresponding to the weak and strong branches of $\mathcal{H}_\lambda$. Let $\mathcal{H}_\lambda \cap \mathcal{L}_\lambda$ denote the curve $(V_h(\lambda), T_h(\lambda), \lambda)$ in the phase-plane. It also plays a key role in the analysis.

It is helpful to consider 2-D projections of phase space. In the (V,P)-plane, $\mathcal{L}_\lambda$ is independent of λ and we denote the Rayleigh line simply by $\mathcal{L}$. Moreover, for fixed V and λ we can invert P and T since $(\partial\tilde{P}/\partial T)_{V,\lambda} = (\Gamma/V)C_V > 0$. We denote $\tilde{T}_\lambda(V,P) = T_\lambda(V,T)$ and $\tilde{h}_\lambda(V,P) = h_\lambda(V,T)$, where $P = \tilde{P}(V,T,\lambda)$. Next we derive geometric properties of the important curves in the (V,P)-plane and (V,T)-plane.

7.1 Geometry in the (V, P)-plane

The three curves $\mathcal{L}$, $\mathcal{H}_\lambda$ and $\mathcal{T}_\lambda$ intersect at two points; the weak and strong deflagration states. Moreover, $\mathcal{L}$ lies above $\mathcal{H}_\lambda$ for $V_w < V < V_s$; see Fig. 1. On the deflagration locus, the CJ point is an entropy maximum. Consequently, the weak branch is subsonic and satisfies

$$-\left(\frac{\partial P}{\partial V}\right)_{S,\lambda} > -\left(\frac{\mathsf{d}P}{\mathsf{d}V}\right)_h > \frac{P - P_0}{V_0 - V} = m^2 \ ;$$

i.e., the isentrope has a steeper slope than the Hugoniot locus which has a steeper slope than the Rayleigh line. With respect to the isothermal sound speed, the weak branch goes from subsonic at $P = P_0$ to supersonic at $P = P_{CJ}$. On subsonic portions, either $-(\frac{\partial P}{\partial V})_h > -(\frac{\partial P}{\partial V})_{T,\lambda}$ or $-(\frac{\partial P}{\partial V})_{T,\lambda} > -(\frac{\partial P}{\partial V})_h$. In the former case T decreases as P decreases and in the latter case T increases; see illustrative examples in Fig. 14.

In contrast, the strong branch is supersonic and the inequalities are reversed;

$$\frac{P - P_0}{V_0 - V} > -\left(\frac{\mathsf{d}P}{\mathsf{d}V}\right)_h > -\left(\frac{\partial P}{\partial V}\right)_{S,\lambda} .$$

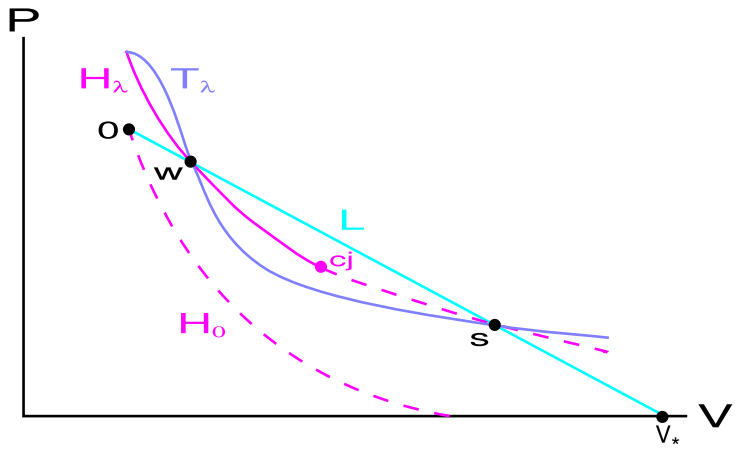

Figure 1: Loci in (V, P)-plane: $\mathcal{L}$ is the Rayleigh line; $\mathcal{H}_\lambda$ is the partly burned Hugoniot locus; $\mathcal{T}_\lambda$ is locus on which $\frac{\mathsf{d}}{\mathsf{d}\zeta}T = 0$. Labels 0, w and s denote the initial, weak and strong deflagration states, respectively.

Since $-(\frac{\partial P}{\partial V})_{S,\lambda} > -(\frac{\partial P}{\partial V})_{T,\lambda}$, the strong branch is also supersonic wrt c_T. Hence, on the strong branch, the temperature always decreases with decreasing pressure.

The vector field of the wave profile ODEs, Eq. (14), has the property that $\mathsf{d}V/\mathsf{d}\lambda > 0$ for points in the (V,P)-plane above $\mathcal{L}$, and that $\mathsf{d}T/\mathsf{d}\lambda > 0$ for points in the (V,P)-plane above $\mathcal{T}_\lambda$. We note that $\mathcal{L}$ intersects the V-axis at $V_* = V_0 + P_0/m^2$. If a solution trajectory starting at the ahead state reaches $V = V_*$, then V can never decrease, as it will hit the phase boundary at $P = 0$ or $T = 0$ before $\frac{\mathsf{d}}{\mathsf{d}\zeta}V$ can reverse sign. Hence, the domain of interest for deflagration wave profiles is restricted to $V < V_*$.

For solid reactants, the cold curve ($T = 0$ isotherm) may intersect $P = 0$ at a value of $V > V_*$. Thus, at sufficiently low pressure, a portion of the Rayleigh line may not be in the physical domain. At $V = 0$, the pressure on the Rayleigh line, $P = P_0 + m^2 V_0$ is finite. Therefore, the Rayleigh line will intersect the cold curve for some $V < V_0$. Hence, a portion of the Rayleigh line for small V will not be in the physical domain. The point is that some solution trajectories of the ODEs, Eq. (14), are of finite extent, *i.e.*, a trajectory terminates if it hits the EOS domain boundary. In the 2-D projections, (V,P)–plane and (V,T)–plane, the EOS domain boundary depends on the value of λ.

The next two propositions characterize important properties of the curves $\mathcal{H}_\lambda$, $\mathcal{T}_\lambda$ and $\mathcal{L}$.

Proposition 7.1. In the (V,P)-plane, $\mathcal{H}_\lambda$ lies between $\mathcal{T}_\lambda$ and $\mathcal{L}$ for $V > V_0$; see Fig. 1.

Proof. Let (V, P_h) be a point on $\mathcal{H}_\lambda$. Suppose $V_0 < V < V_w$. In this interval, $\mathcal{H}_\lambda$ lies above $\mathcal{L}$; *i.e.*, $P_h(V) > P_{\mathcal{L}}(V)$. Then

$$\begin{aligned}\tilde{T}_\lambda(V, P_h(V)) &= \tilde{T}_\lambda(V, P_h(V)) - \tilde{h}_\lambda(V, P_h(V)) \\ &= \tfrac{1}{2}[P_{\mathcal{L}}(V) - P_h(V)]\,(V - V_0) < 0\ .\end{aligned}$$

Since $(\partial \tilde{T}_\lambda/\partial P)_V = (\partial e/\partial P)_{V,\lambda} = V/\Gamma > 0$, it follows that $\tilde{T}_\lambda(V,P)$ can only be 0 for some $P > P_h(V)$. Hence, $\mathcal{T}_\lambda$ lies above $\mathcal{H}_\lambda$. Similar arguments show that the order reverses whenever $\mathcal{H}_\lambda$ crosses $\mathcal{L}$. Consequently, $\mathcal{H}_\lambda$ lies between $\mathcal{T}_\lambda$ and $\mathcal{L}$ for $V > V_0$. ⊠

The slope of $\mathcal{T}_\lambda$ can be obtained by taking the derivative of Eq. (43). With thermodynamic derivatives implied by Eq. (6), the result is

$$\left(\frac{\mathsf{d}P}{\mathsf{d}V}\right)_{\mathcal{T}_\lambda} = -\frac{\Gamma}{V}\left[P_{\mathcal{L}} + (\gamma/\Gamma - 1)\, P\right] . \tag{44}$$

Since $\gamma/\Gamma > 1$, in the domain of interest, $V_0 < V < V_*$, $(\mathsf{d}P/\mathsf{d}V)_{\mathcal{T}_\lambda} < 0$. At the weak and strong states, $\left(\frac{\mathsf{d}P}{\mathsf{d}V}\right)_{\mathcal{T}_\lambda} = -\gamma P/V$. Hence, $\mathcal{T}_\lambda$ is tangent to the isentrope when it crosses $\mathcal{L}$.

Proposition 7.2. In the (V, P)-plane, the curves $\mathcal{T}_\lambda$ with different λ do not intersect. Moreover, $\mathcal{T}_{\lambda_2}$ lies above $\mathcal{T}_{\lambda_1}$ if $\lambda_2 > \lambda_1$.

Proof. Result follows from Eq. (43) and the thermodynamic inequalities $(\partial_\lambda e)_{V,P} < 0$ and $(\partial_P e)_{V,\lambda} = V/\Gamma > 0$. ⊠

Remark: The states w and s satisfy the shock jump conditions. One can define $\mathcal{H}_\lambda(s)$ as the Hugoniot locus based on the state s. Moreover, $\mathcal{L}$ and $\mathcal{T}_\lambda$ are the same for initial states 0 and s. Using a similar argument to that in the proof of proposition 7.1, we can show that for $V < V_s$, $\mathcal{T}_\lambda$ lies between $\mathcal{H}_\lambda(s)$ and $\mathcal{L}$. Consequently, $\mathcal{H}_\lambda(0)$ is not the same as $\mathcal{H}_\lambda(s)$, though they both go through states w and s.

7.2 Geometry in the (V, T)-plane

For a given λ, the curves $\mathcal{H}_\lambda$, $\mathcal{T}_\lambda$ and $\mathcal{L}$ can be projected onto the (V, T)-plane. Since $(\partial_T \widetilde{P})_{V,\lambda} = \frac{\Gamma}{V} C_V > 0$, the curves have the same ordering in the (V, T)-plane as given by proposition 7.1 for the (V, P)-plane. A sketch of the these curves in the (V, T)-plane is shown in Fig. 2. For the sketch, it is assumed that the weak branch of the deflagration locus is subsonic wrt c_T and the EOS is such that isotherms are convex. Consequently, there is a unique temperature maximum on $\mathcal{L}_\lambda$. The qualitative properties of the curves $\mathcal{H}_\lambda$, $\mathcal{T}_\lambda$ and $\mathcal{L}$ shown in the sketch are consistent with the following propositions.

Proposition 7.3. Projected onto the (V, T)-plane, $\mathcal{L}_\lambda$ with different λ do not intersect. Moreover, $\mathcal{L}_{\lambda_2}$ lies below $\mathcal{L}_{\lambda_1}$ if $\lambda_2 > \lambda_1$.

Proof. Follows from the thermodynamic inequalities for the derivatives of $\widetilde{P}$; $(\partial_T \widetilde{P})_{V,\lambda} > 0$ and $(\partial_\lambda \widetilde{P})_{V,T} > 0$. ⊠

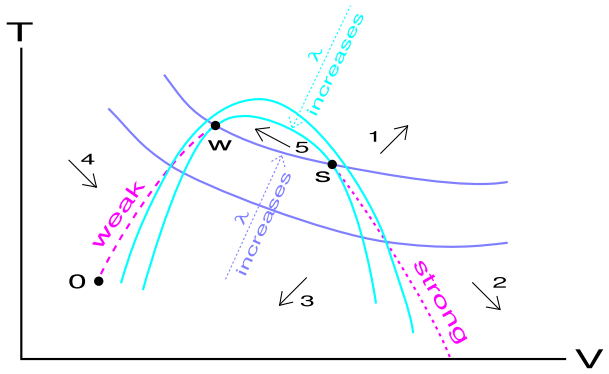

Figure 2: Loci in (V,T)-plane: cyan curves correspond to $\mathcal{L}_\lambda$; blue curves to $\mathcal{T}_\lambda$; dashed magenta curves to weak and strong branches of $\mathcal{H}_\lambda \cap \mathcal{L}_\lambda$. Labels 0, w and s denote the initial, weak and strong states, respectively. Black arrows show the direction of the vector field of the wave profile ODEs in the five regions formed by the intersection of curves $\mathcal{L}_\lambda$ and $\mathcal{T}_\lambda$.

The slope of $\mathcal{L}$ can be obtained by taking the derivative of Eq. (42). After substituting thermodynamic identities, the result is

$$\left(\frac{\mathsf{d}T}{\mathsf{d}V}\right)_{\mathcal{L}} = \frac{V}{\Gamma C_V}\Big[(\rho\, c_T)^2 - m^2\Big] \,. \tag{45}$$

Hence, the slope is positive iff the state is subsonic wrt c_T. Since we are assuming the weak branch is subsonic and the strong branch is always supersonic, the temperature peak occurs at a point with V between V_w and V_s. Moreover, as a consequence of proposition 7.3, the temperature peak decreases as λ increases.

From Eq. (33), the slope of $\mathcal{H}_\lambda \cap \mathcal{L}_\lambda$ is

$$\left(\frac{\mathsf{d}T}{\mathsf{d}V}\right)_{\mathcal{H}_\lambda\cap\mathcal{L}_\lambda} = \frac{-[(\rho\, c_T)^2 - m^2]\,\partial_\lambda e/C_V - (\Gamma/V)\,T\,\partial_\lambda \widetilde{P}}{\partial_\lambda \widetilde{P} - (\Gamma/V)\,\partial_\lambda e} \,. \tag{46}$$

It is straightforward to show that the relative slopes depend on whether the flow is subsonic or supersonic; $\left(\frac{\mathsf{d}T}{\mathsf{d}V}\right)_{\mathcal{L}} > \left(\frac{\mathsf{d}T}{\mathsf{d}V}\right)_{\mathcal{H}_\lambda\cap\mathcal{L}_\lambda}$ on the weak branch, and the opposite inequality on the strong branch.

Proposition 7.4. In the (V,T)-plane, the curves $\mathcal{T}_\lambda$ with different λ do not intersect. Moreover, $\mathcal{T}_{\lambda_2}$ lies above $\mathcal{T}_{\lambda_1}$ if $\lambda_2 > \lambda_1$.

Proof. Follows from the thermodynamic inequalities for the derivatives of e; $(\partial_\lambda e)_{V,T} < 0$ and $(\partial_T e)_{V,\lambda} > 0$. ⊠

The slope of $\mathcal{T}_\lambda$ can be obtained by taking the derivative of Eq. (43). After substituting thermodynamic identities, the result is

$$\left(\frac{\mathsf{d}T}{\mathsf{d}V}\right)_{\mathcal{T}_\lambda} = -\frac{P_{\mathcal{L}} - P}{C_V} - \frac{\Gamma T}{V} \ . \tag{47}$$

Between the weak and strong states, $V_w < V < V_s$, $(\mathsf{d}T/\mathsf{d}V)_{\mathcal{T}_\lambda} < 0$. One consequence is that $T_w > T_s$.

7.3 Phase-plane topology

The curves $\mathcal{L}_\lambda$ and $\mathcal{T}_\lambda$ divide the (V, T)-plane into five sectors, which we label as follows:

$S_1(\lambda)$: Above $\mathcal{L}_\lambda$ and above $\mathcal{T}_\lambda$.

$S_2(\lambda)$: Above $\mathcal{L}_\lambda$ and below $\mathcal{T}_\lambda$ with $V > V_{s(\lambda)}$.

$S_3(\lambda)$: Below $\mathcal{L}_\lambda$ and below $\mathcal{T}_\lambda$.

$S_4(\lambda)$: Above $\mathcal{L}_\lambda$ and below $\mathcal{T}_\lambda$ with $V < V_{w(\lambda)}$.

$S_5(\lambda)$: Below $\mathcal{L}_\lambda$ and above $\mathcal{T}_\lambda$.

The direction of the vector field for the wave profile ODE, Eq. (14), depends on the sector. These sectors and the directions are sketched in Fig. 2.

The sector boundaries depend on λ. Due to the variation of $\mathcal{L}_\lambda$ and $\mathcal{T}_\lambda$ with λ, propositions 7.3 and 7.4, sector S_5 is nested; *i.e.*, $S_5(\lambda_2) \subset S_5(\lambda_1)$ if $\lambda_2 > \lambda_1$. Moreover, at the boundaries of S_5, the vector field points outward, except for the critical point $w(\lambda)$. Consequently, any trajectory starting outside S_5 is appriori excluded from all of $S_5(1) = \bigcap_\lambda S_5(\lambda)$ except the behind state $w(1)$ which can be reached asymptotically since the rate $\mathcal{R}$ then vanishes.

Two additional properties follow from the fact that in the (V, T)–plane with increasing λ the curve $\mathcal{L}_\lambda$ moves down while the curve $\mathcal{T}_\lambda$ moves up. First, the sectors S_2 and S_4 are strictly increasing, *i.e.*, $S_2(\lambda_2) \supset S_2(\lambda_1)$ if $\lambda_2 > \lambda_1$ and similarly for $S_4(\lambda)$. Second, in the sectors S_1 and S_3, the vector field rotates with increasing λ as follows.

Proposition 7.5. For any (V,T) point in sector S_1, with increasing λ the direction of the vector field in the (V,T)-plane rotates clockwise. Similarly, for any point in sector S_3, the vector field rotates counter-clockwise.

Proof. From the ODEs, Eq. (14), the direction of the vector field in the (V,T)–plane is given by

$$\frac{\Delta V}{\Delta T} = \frac{\mathsf{d}V/\mathsf{d}\zeta}{\mathsf{d}T/\mathsf{d}\zeta} = \frac{C_r}{m^2\,Pr}\cdot\frac{\widetilde{P}(V,T) - P_{\mathcal{L}}(V)}{e(V,T) - e_0 - \frac{1}{2}(P_{\mathcal{L}}(V)+P_0)(V_0 - V)}\ . \tag{48}$$

For fixed V and T, the change in the direction of the vector field is

$$\frac{\mathsf{d}}{\mathsf{d}\lambda}\left(\frac{\Delta V}{\Delta T}\right) = \frac{\Delta V}{\Delta T}\cdot\left[\frac{(\partial_\lambda \widetilde{P})_{V,T}}{\Delta V} - \frac{(\partial_\lambda e)_{V,T}}{\Delta T}\right]. \tag{49}$$

From App. C, $(\partial_\lambda \widetilde{P})_{V,T} > 0$ and $(\partial_\lambda e)_{V,T} < 0$. In sector S_1, $\Delta V > 0$ and $\Delta T > 0$. Therefore, the right hand side of Eq. (49) is positive. Hence, with increasing λ, the vector field rotates clockwise.

Similarly, in sector S_3, $\Delta V < 0$ and $\Delta T < 0$. Therefore, the right hand side of Eq. (49) is negative. Hence, with increasing λ, the vector field rotates counter-clockwise. ⊠

The excluded region S_5 is topologically important. In effect, the (V,T)–plane is not simply connected. Starting in a neighborhood of the initial (ahead) state, we will show that some trajectories will go around the top of S_5, while others will go underneath it. A distinguished trajectory will end at the critical point w. Moreover, though the vector field changes with the mass flux, as a result of the excluded region, the general structure of the trajectories is invariant.

7.4 Trajectories in the (V,T)-plane

It is instructive to consider first the solution trajectories of the non-reactive wave profile ODEs, Eq. (14) with fixed λ and zero rate. These are sketched in Fig. 3. The magenta trajectory from s to w corresponds to the shock profile determined by the analysis of Gilbarg [1951]. We note that Fig. 3 covers an extended domain in the (V,T)–plane compared to Fig. 2. Consequently,

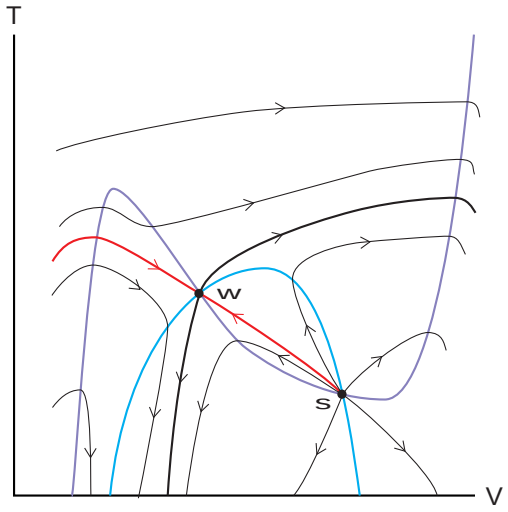

Figure 3: Trajectories in (V, T)-plane for wave profile ODEs with fixed λ and $\mathcal{R} = 0$. Cyan and blue curves correspond to $\mathcal{L}_\lambda$ and $\mathcal{T}_\lambda$, respectively. Labels w and s denote the weak and strong states, respectively. Red curve is attractive manifold to state w. The arrows are in direction of decreasing ζ; *i.e.*, for a wave profile starting at the ahead state.

the curve $\mathcal{T}_\lambda$ is not monotonic and terminates at $T = 0$ for small V. This is due to the EOS domain (cold curve boundary) briefly discussed in the previous subsection. Not shown is the $P = 0$ domain boundary which for solid reactant (and hence partly burned HE in P-T equilibrium) would affect some aspects of the curves at large V.

Several points are noteworthy. First, at the critical point w, the eigenvectors of the matrix $\mathbf{A}_{\rm nr}$ are in the direction between the curves $\mathcal{L}_\lambda$ and $\mathcal{T}_\lambda$. Moreover, for the stable manifold of the ahead state (the positive eigenvalue), $\Delta T/\Delta V > 0$. Therefore, possible trajectories of interest for determining a deflagration wave profile start at $w(0)$ with both V and T increasing.

Second, if the mass flux m is too large then the effective rate, right hand side of Eq. (14c), which is proportional to $1/m$ will be too small. The trajectory starting at the ahead state along the stable manifold will be similar to that of the non-reactive case and pass over the top of sector S_5.

Third, trajectories only enter sector S_5 from the critical point at state s. Moreover, state s is a repeller, *i.e.*, all trajectories go away from s. This enables us to proof that strong deflagrations are inadmissible.

Theorem 7.1. No solution trajectory of the wave profile ODEs, Eq. (14), corresponds to a strong deflagration wave.

Proof. As shown in Fig. 2, sector $S_5(\lambda)$ shrinks as λ increases; *i.e.*, $S_5(\lambda_2) \subset S_5(\lambda_1)$ for $\lambda_2 > \lambda_1$. It follows that no trajectory starting at an initial state outside sector $S_5(\lambda_1)$ can end at the strong state for $\lambda_2 > \lambda_1$. For a deflgration wave, the ahead state $w(\lambda = 0)$ lies outside $S_5(\lambda = 1)$. Therefore, no trajectory can exist that connects the ahead state to a point on the strong branch of the deflagration locus. ⊠

Remarks:

(i) It is possible for a trajectory starting at a supersonic state $V_0 > V_s$, *i.e.*, $s(0)$, to stay within sector S_5; approach close to state $s(1)$ and then continue to terminate at state $w(1)$. Such a profile has the appearance of a weak detonation, followed by an inert shock to the strong detonation state. (The states s and w for a strong and weak detonation are reversed compared to the nomenclature used for a deflagration wave.) Profiles of this type have been proved to exist for an ideal explosive EOS by Wagner [1989], and observed in numerical simulations. Typically, these anomalous detonation waves occur only when the numerical viscosity is sufficiently large that the shock width is comparable to the reaction-zone width.

(ii) Previously, a ZND detonation was described as a lead shock followed by a deflagration wave. The profile of the lead shock corresponds to the magenta curve in Fig. 3 from state $s(0)$ to state $w(0)$. Since $w(0)$ is a saddle type critical point, there are nearby trajectory that closely approach $w(0)$ and then change direction abruptly; either increase or decrease of slope. In the limit of small viscosity, when the shock profile is very narrow, this variation in neighboring profiles provides the degree of freedom to set the derivate $\mathsf{d}T/\mathsf{d}V$ behind the shock front for the deflagration profile to exist.

Next we show that if a trajectory goes over top of sector S_5 then it can not end at a point on the deflagration locus. Hence, this class of trajectories can be eliminated from consideration for a deflagration profile.

Proposition 7.6. A trajectory $\Big(V(\lambda), T(\lambda)\Big)$ that reaches a point such that $T(\lambda) \geq T_1\Big(V(\lambda)\Big)$, where T_1 is the temperature on the curve $\mathcal{T}_\lambda$ for $\lambda = 1$, will either continue to $V \to \infty$ or terminate at an EOS domain boundary, such as $T = 0$.

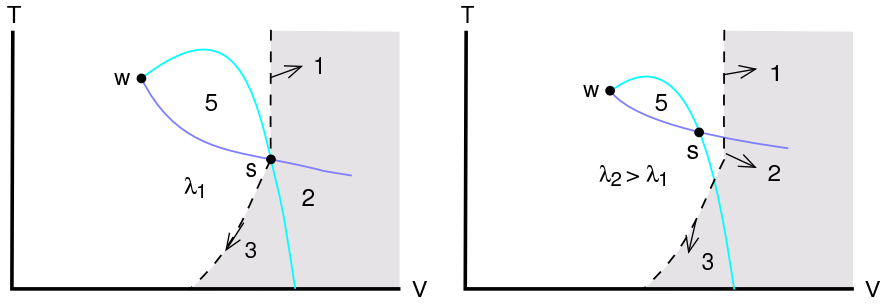

Figure 4: Sketch of absorbing region, shown in gray, for trajectories in (V,T)–plane. Cyan and blue lines correspond to curves $\mathcal{L}_\lambda$ and $\mathcal{T}_\lambda$, respectively, and numbers indicate sector. Arrows at region boundaries (dashed black line) are in direction of vector field for the wave profile ODEs. Right plot is for a larger λ.

Proof. A trajectory reaching the point $T(\lambda) \geq T_1\Big(V(\lambda)\Big)$ lies in the sector $S_1(\lambda)$. It will continue in sector S_1 and reach a point on the line $V = V_{s(\lambda_1)}$ in sector $S_1(\lambda_1)$ for some $\lambda_1 > \lambda$. (If no such state $s(\lambda_1)$ exists then a sector $S_5(\lambda_1)$ would intersect the V-axis and the proposition would be trivially true since V would always be increasing.)

Consider the region to the right (larger V) of the curves (i) $T > T_s(\lambda_1)$ and $V = V_s(\lambda_1)$, and (ii) a trajectory for the vector field of the non-reactive ODEs with λ_1 fixed that lies in sector S_3 and start at the repeller $s(\lambda_1)$ and goes to a point on the phase boundary at $T = 0$. This is the gray region shown in Fig. 4. We show that this is an absorbing region for all $\lambda > \lambda_1$.

Since the reaction rate is positive, λ can only increase. Consider any $\lambda_2 > \lambda_1$. The strong deflagration point $s(\lambda_2)$ lies inside the sector $S_5(\lambda_1)$. As shown in the right plot of Fig. 4, the boundary curve is divided into three sectors. By proposition 7.5, the vector field in sectors S_1 and S_3 rotate into the gray region. The vector field for sector S_2 is in the direction with $\Delta T/\Delta V < 0$, and also points into the gray region. Hence a trajectory that enters the gray region can never leave that region. ⊠

The condition in the proposition that $T(\lambda) \geq T_1\Big(V(\lambda)\Big)$ is important. If the reaction causes $\mathcal{T}_\lambda$ to rise faster than the trajectory moves in the (V,T)-plane then the trajectory could cross into sector S_4. In this case the trajectory may either approach $w(1)$ with T decreasing or cross a boundary of sector S_4. One boundary is the Rayleigh line. As shown in the next

proposition a trajectory crossing the Rayleigh line can not reach $w(1)$. Otherwise the trajectory can cross back into sector S_1. Since V increases while the trajectory is in either sectors S_1 or S_4, the trajectory either hits $w(1)$ or proposition 7.6 would apply when V reaches $V_{w(1)}$.

A corollary to this proposition is that no trajectory of the wave profile ODEs projects in the (V, T)–plane onto a loop around the excluded sector S_5.

Next we show that the trajectory of a deflagration wave profile can not cross the Rayleigh line for $V < V_{w(1)}$.

Proposition 7.7. A trajectory $\Big(V(\lambda), T(\lambda)\Big)$ that crosses the Rayleigh line between sectors $S_3(\lambda_1)$ and $S_4(\lambda_1)$, for some λ_1, can not reach the weak deflagration point $w(1)$.

Proof. On the segment of the Rayleigh line $\mathcal{L}_{\lambda_1}$ between sectors $S_3(\lambda_1)$ and $S_4(\lambda_1)$, $V \leq V_{w(\lambda_1)}$. For simplicity, we assume that the state $w(\lambda_1)$ is subsonic wrt c_T. Then on the segment of $\mathcal{L}_{\lambda_1}$, $\mathsf{d}T/\mathsf{d}V > 0$. The idea of the proof is to construct an absorbing region in the full (V, T, λ)-phase space with the $V \leq V_{w(\lambda_1)}$ segment of $\mathcal{L}_{\lambda_1}$ as part of the boundary and that does not contain the point $w(1)$.

Consider the cylinder with cross section in the (V, T)–plane for $\lambda_2 > \lambda_1$ bounded by the following curves: on the left by $\mathcal{L}_{\lambda_1}$, the top by $T = T(w(\lambda_1))$, the top-right corner by $\mathcal{T}_{\lambda_2}$ and the right by $V = V(s(1))$. This is the gray region shown in Fig. 5. Also shown are arrows at the boundaries for the (V, T)-components of the vector field. It can be readily verified that the vector field points into the cross section.

The cylinder is bounded by the planes $\lambda = \lambda_1$ and $\lambda = 1$. With increasing λ the cross section is strictly increasing. Therefore, the vector field points into the cylinder in the full (V, T, λ)-phase space. Hence, it is an absorbing region. Since it does not contain the state $w(1)$, any trajectory reaching the cylinder boundary can not be a valid wave profile. ⊠

Since the remainder of the Rayleigh line bounds the excluded region S_5, a wave profile trajectory can not cross the Rayleigh line. Hence, V must be monotonically increasing along a wave profile. It then follows that T_0 is a lower bound for the temperature along a wave profile. Previously, proposition 7.6 gave an upper bound on the temperature. Combining all these

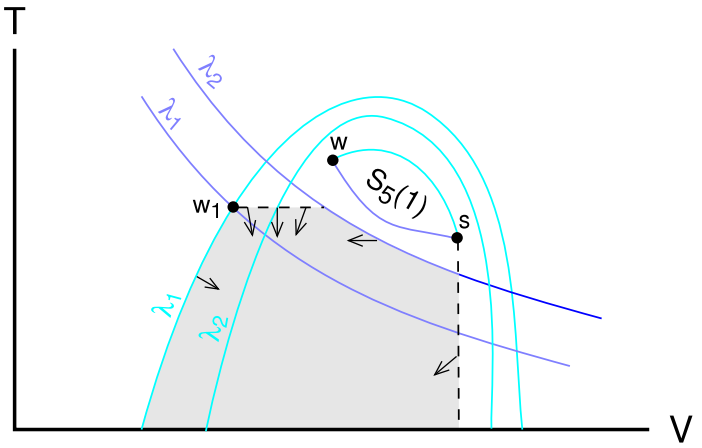

Figure 5: Cross section in (V,T)–plane for $\lambda = \lambda_2$ of absorbing region, shown in gray, with boundary including the Rayleigh line between $S_3(\lambda_1)$ and $S_4(\lambda_1)$. Cyan and blue lines correspond to curves $\mathcal{L}_\lambda$ and $\mathcal{T}_\lambda$, respectively. Arrows at region boundary are in direction of vector field for the wave profile ODEs.

observations, a deflagration wave profile trajectory in the (V,T)–plane must lie in a region bounded by $V_0 \le V \le V_{w(1)}$ and $T_0 \le T \le T_1\Big(V(\lambda)\Big) < T_1(V_0)$. A model EOS only needs to be well defined in this limited region of phase space.

The wave profile trajectory will lie mostly within sector $S_1(\lambda)$ for which both V and T are increasing with λ. The final approach to the weak state is governed by the eigenfunctions of the critical point matrix $\mathbf{A}$ for the stable manifold. In particular, the eigenfunction corresponding to the eigenvalue with the smaller magnitude will dominate. Typically, the coefficient of thermal conduction is sufficiently small such that the eigenvalue from the rate is the smaller, and the corresponding eigenfunction has $\Delta V/\Delta T > 0$. In this case, the temperature may be monotonically increasing along the entire wave profile.

We note that the negative eigenvalue of $\mathbf{A}_{\rm nr}$ has an eigenfunction with $\Delta V/\Delta T < 0$. If this eigenvalue is smaller in magnitude than that of the rate, then the wave profile trajectory would have to cross $\mathcal{T}_\lambda$ into sector $S_4(\lambda)$ and approaches $w(1)$ with T decreasing. Also, if the state $w(1)$ is supersonic wrt c_T (as occurs for the deflagration following the lead shock of a CJ detonation wave) then it lies on the Rayleigh line with $\mathsf{d}T/\mathsf{d}V < 0$, and the wave profile would have to approach $w(1)$ with T decreasing.

Based on the preceding analysis of the trajectories of the ODEs in the (V, T)-plane, we can now give a qualitative description of the trade-offs that determine the mass flux for which a wave profile exists. Without reaction the trajectory from the ahead state would be in sector S_1 and pass over the top of the top of sector S_5. Reaction causes the curves $\mathcal{T}_\lambda$ and $\mathcal{L}_\lambda$ to shift and bends the vector field within sector S_1 in the direction of $w(1)$. The key question is the rate at which the vector field changes.

The right hand side of Eq. (14c) is proportional to $\kappa\mathcal{R}/m^2$. This controls the rate at which the vector field changes. If m is too large then the vector field changes too slowly and the trajectory will go over the top of sector S_5 and miss the end state $w(1)$. On the other hand, if m is too small then the curve $\mathcal{T}_\lambda$ will move up too rapidly, and the trajectory will enter sector S_4. In this sector, the vector field changes direction. The temperature would decrease causing the trajectory to pass through the Rayleigh line and go below sector S_5.

We know from the structure of the deflagration locus that the mass flux lies in a bounded interval; $0 < m \leq m_{\text{CJ}}$. If one checks the end points, *i.e.*, for $m = m_{\text{CJ}}$ the trajectory goes over sector S_5 and for $m = 0$ the trajectory goes under sector S_5, then by continuity a value of m would exist such that the trajectory reaches a weak deflagration state on the deflagration locus. In the limit $m \to 0$, $\frac{\mathsf{d}}{\mathsf{d}\zeta}\lambda \to \infty$. A local analysis about the ahead state would undoubtable show that the trajectory hits the Rayleigh line and hence goes under sector S_5. Then a general proof of the existence of a deflagration wave profile would hinge on analyzing the behavior of the trajectory for $m = m_{\text{CJ}}$.

Undoubtedly a condition will be required on the $\kappa\mathcal{R}$. If the rate is scaled to be sufficiently large (*e.g.*, increasing Z in Eq. (22) for the Arrhenius rate) or κ is increased to be sufficiently large, then the trajectory for $m = m_{\text{CJ}}$ can be expected to pass under the sector S_5. For an initiation source, such as a hot spot, physical intuition suggests that instead of a deflagration wave, a transient due to rapid reaction will generate a shock that either would precondition the ahead state such that a deflagration wave exists or would lead to a shock-to-detonation transition. In addition, depending on boundary conditions, rather than a steady wave, a chugging or pulsating reactive wave could occur.

Remarks:

(i) The rate on the right hand side of Eq. (14c) is proportional to the thermal diffusion length ℓ divided by m. Moreover, the eigenvalue r_3 of $\mathbf{A}$ at the behind state is proportional to ℓ/m. In a sense this sets the scale for how the trajectory in the (V,T)-plane varies relative to how the curves $\mathcal{T}_\lambda$ and $\mathcal{L}_\lambda$ vary. Possibly, this can provide a justification for deflagration speed estimate of Eq. (15).

(ii) Typically, for a gaseous deflagration wave profile, m is very small compared to $m_{\rm CJ}$. In this case, as the rate is varied (*e.g.*, by changing the initial temperature) the mass flux and hence the deflagration speed would scale linearly with the rate since the behind state would not change very much and hence the key curves in the (V,T)-plane would be nearly invariant. However, non-linear effects would become important if the scaled m becomes large, and crucial if the scaled m exceeds $m_{\rm CJ}$.

(iii) A resonant-like behavior is possible in which the trajectory of a wave profile crosses $\mathcal{T}_\lambda$ to sector S_4 and then back to sector S_1 for a larger λ. In this case, the temperature would not be monotonic. This anomalous behavior is unlikely for an Arrhenius like rate which increases very rapidly with temperature.

7.5 Heat conduction only

The right hand side of Eq. (14a) for $\frac{\mathsf{d}}{\mathsf{d}\zeta}V$ is proportional to $(m^2 Pr)^{-1}$. If either m or the Prandtl number (*i.e.*, viscosity) are sufficiently small, then the ODE is nearly singular and numerical integration of the ODEs, Eq. (14), is very sensitive to roundoff errors in evaluating $\Delta\Big[P + m^2\, V\Big]$. Here, we consider the case of zero viscosity, and replace Eq. (14a) with the algebraic constraint that the flow lies on the Rayleigh line, Eq. (20).

Suppose that the points on the deflagration locus are subsonic wrt c_T; *i.e.*, $m < \rho\, c_T$. Geometrically, in the (V,P)-plane at the intersection of the partly burned Hugoniot loci and the Rayleigh line, the isotherm has a greater slope than the Rayleigh line. This is the typical case for a gaseous deflagration wave, which has a sufficiently low deflagration speed that the change in pressure can be neglected.

With this assumption on c_T, we can apply the implicit value theorem to obtain V as a function of T and λ; *i.e.*, $V_{\mathcal{L}}(T,\lambda)$. Consequently, the analysis of the remaining wave profile ODEs, Eqs. (14b) and (14c), is reduced to the study of the two-dimensional phase plane (T,λ). Moreover, $\mathcal{H}_\lambda \cap \mathcal{L}_\lambda$ projects onto the curve $(T_h(\lambda),\lambda)$. Typically, $T_h(\lambda)$ is a monotonically increasing function of λ. Another consequence of the assumption on c_T is that $\frac{\partial V_{\mathcal{L}}}{\partial T}(T_h(\lambda),\lambda) > 0$. It then follows from proposition 7.1 that the T component of the vector field of the ODEs points away from the curve $\mathcal{H}_\lambda \cap \mathcal{L}_\lambda$.

The ahead and behind states remain critical points of the reduced model. The linearized equations about the critical points,

$$\frac{\mathsf{d}}{\mathsf{d}\zeta}\begin{pmatrix}\hat{T}\\ \hat{\lambda}\end{pmatrix} = -\,\mathbf{A}_2\begin{pmatrix}\hat{T}\\ \hat{\lambda}\end{pmatrix}\ , \tag{50}$$

can be obtained from Eqs. (24) and (25). Based on Eq. (21), for the purpose of linearizing, we can substitute

$$\Big[(\rho\, c_T)^2 - m^2\Big]\hat{V} = \rho^2\,\Gamma\,(C_V\,T)\,\hat{T} + \rho\,(\partial_\lambda \widetilde{P})_{V,T}\hat{\lambda}\ . \tag{51}$$

At the ahead state ($\lambda = 0$), with $T_{\text{ign}} = T_0$,

$$\mathbf{A}_2 = \begin{pmatrix} \frac{(\rho\, c)^2 - m^2}{(\rho\, c_T)^2 - m^2}\cdot\frac{C_V}{C_r} & -\frac{(\rho\, c)^2 - m^2}{(\rho\, c_T)^2 - m^2}\cdot\frac{C_V}{C_r}\cdot\frac{\mathsf{d}T_h/\mathsf{d}\lambda}{T} \\ r_2 & 0 \end{pmatrix}\ , \tag{52}$$

and at the behind state ($\lambda = 1$),

$$\mathbf{A}_2 = \begin{pmatrix} \frac{(\rho\, c)^2 - m^2}{(\rho\, c_T)^2 - m^2}\cdot\frac{C_V}{C_r} & -\frac{(\rho\, c)^2 - m^2}{(\rho\, c_T)^2 - m^2}\cdot\frac{C_V}{C_r}\cdot\frac{\mathsf{d}T_h/\mathsf{d}\lambda}{T} \\ 0 & r_3 \end{pmatrix}\ . \tag{53}$$

Moreover, r_2 is small at the ahead state. In both cases, one eigenvalue is

$$\alpha_1 = \frac{C_V}{C_r}\cdot\frac{(\rho\, c)^2 - m^2}{(\rho\, c_T)^2 - m^2} > 0\ . \tag{54}$$

The second eigenvalue is

$$\alpha_2 = \begin{cases} \frac{1}{T}\frac{\mathsf{d}}{\mathsf{d}\lambda}T_h \cdot r_2 > 0\ , & \text{ahead state;} \\ r_3 < 0\ , & \text{behind state.} \end{cases} \tag{55}$$

Hence, the critical points at the ahead and behind states correspond to a repeller and a saddle, respectively. However, as shown in Appendix E, the phase space boundary at either $\lambda = 0$ or $T = T_{\text{ign}}$ limits the degrees of freedom associated with the repeller nature of the ahead state.

A deflagration profile only exists for a critical value of the mass flux, m_*. With $T_0 < T_{\text{ign}}$, the phase portrait is sketched in Fig. 6 for three cases: (i) $m < m_*$; (ii) $m = m_*$; (iii) $m > m_*$. It is important to note that the vector field of the reduced system is compatible with the full system of ODEs, Eq. (14), in the limit as $\nu \to 0$. That is to say that the vector field for a point on the curve $\mathcal{L}_\lambda$ in sectors S_1 or S_4 points in the direction of $\mathcal{L}_{\lambda_1}$ with $\lambda_1 = \lambda + \mathsf{d}\lambda$; see Fig. 2. Consequently, the constraint that the trajectory lies on the Rayleigh line represents a stable manifold, at least for $V < V_w$.

Points on the segment of $\mathcal{H}_\lambda \cap \mathcal{L}_\lambda$ with $T < T_{\text{ign}}$ in the (T, λ)-plane are degenerate critical points. Moreover, there is a limiting solution trajectory starting on $\mathcal{H}_\lambda \cap \mathcal{L}_\lambda$ with $T = T_{\text{ign}}$ and initial direction corresponding to the eigenfunction of $\mathbf{A}_2$ with the larger eigenvalue, *i.e.*, α_1. The different cases depend on whether the limiting trajectory ends to the left or right of $\mathcal{H}_\lambda \cap \mathcal{L}_\lambda$.

We observe from Eq. (14c) that $\frac{\mathsf{d}\lambda}{\mathsf{d}T} \propto m^{-2}$. Consequently, when m is too small the trajectory starting at the ahead state is too steep, crosses $\mathcal{H}_\lambda \cap \mathcal{L}_\lambda$ and continues to the left. Conversely, if m is too large, $\frac{\mathsf{d}\lambda}{\mathsf{d}T}$ is too small and the trajectory continues to the right without ever crossing $\mathcal{H}_\lambda \cap \mathcal{L}_\lambda$. At the critical mass flux the trajectory ends at a weak deflagration wave state. Moreover, for this trajectory, the temperature increases monotonically from the ahead state to the behind state. The value of the critical mass flux, m_*, depends on the ahead state, the rate and the coefficient of thermal conduction κ.

For $T_{\text{ign}} = T_0$, the general structure is similar. There is a critical value of the mass flux, m_*, for which the limiting solution trajectory from the critical point at the ahead state ends at the behind state. One would expect to find other heteroclinic orbits for $m < m_*$, since the initial slope of the trajectory at the ahead state can be in sector between the solid black and red curves shown in Fig. 16. As shown in Appendix E, the sector is very narrow when $\mathsf{d}T_h/\mathsf{d}\lambda$ is large and r_2 is very small. Due to the extreme sensitivity of the trajectories in the vicinity of the ahead state, very likely only the limiting solution trajectory would be stable. Then provided that T_{ign} is only slightly greater than T_0, one would expect T_{ign} to have a negligible affect on the admissible deflagration wave.

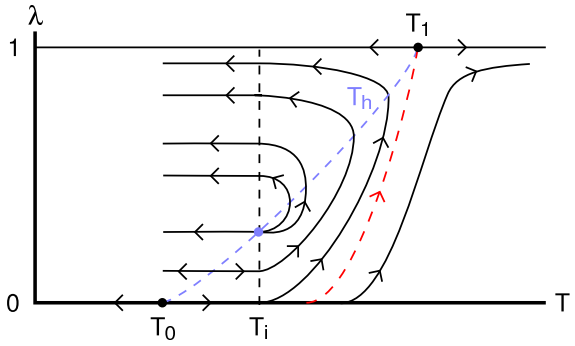

A. $m < m_*$

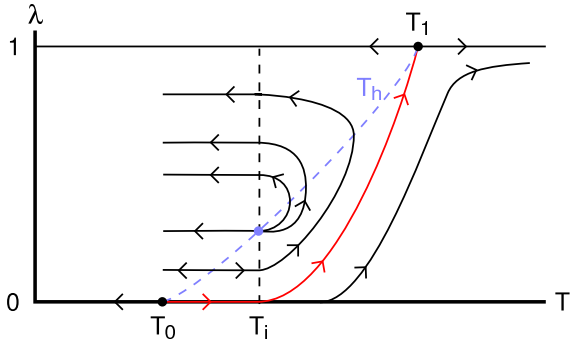

B. $m = m_*$

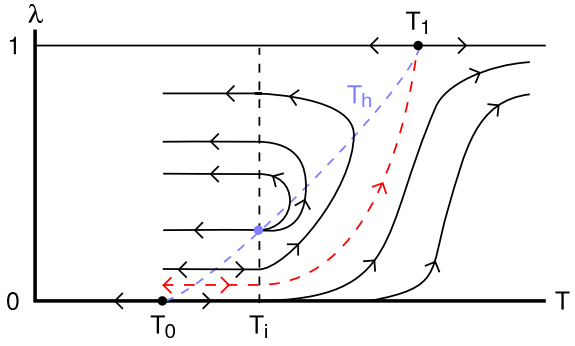

C. $m > m_*$

Figure 6: Phase portrait of wave profile ODEs with zero viscosity and ignition temperature $T_i > T_0$. Ahead and behind states are labeled 0 and 1, respectively. Solid red curve is solution trajectory for a deflagration wave profile. Dashed red curve is the separatrix.

7.6 Zero heat conduction

For completeness, we consider the case of zero thermal conductivity; *i.e.*, viscosity only. Then replacing Eq. (14b) with the algebraic constraint that the flow lies on the curve $\mathcal{T}_\lambda$, *i.e.*, Eq. (43) with $T_\lambda(V,T) = 0$, reduces the system to the study of the two-dimensional phase plane (V,λ).

The phase portrait of the reduced ODEs in the (V,λ)-plane is shown in Fig. 7. It would appear for $T_i = T_0$ that a wave profile trajectory always exists and that for $T_i > T_0$ that no wave profile trajectory exists. However, the vector field of the reduced system is not compatible with the full system

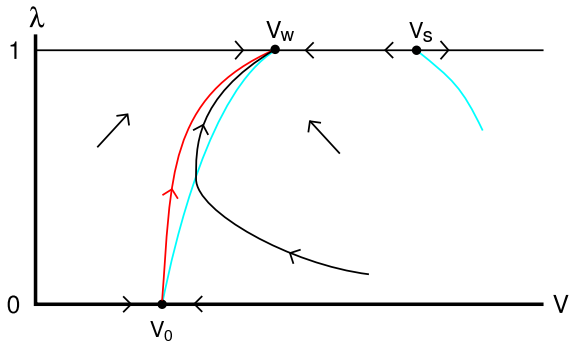

A. $T_i = T_0$

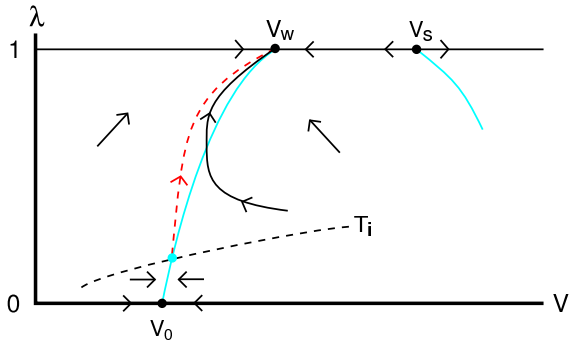

B. $T_i > T_0$

Figure 7: Phase portrait of wave profile ODEs with zero thermal conduction. Ahead and behind states are labeled 0 and w, respectively. Cyan curve is the projection of Rayleigh line. Solid red curve in plot A is a trajectory for a deflagration wave profile. Dashed black curve in plot B is the projection of the ignition temperature.

of ODEs, Eq. (14), in the limit as $\kappa \to 0$. To see this, suppose that the trajectory point lies on $\mathcal{T}_\lambda$ in Fig. 2. Then as λ increases $\mathcal{T}_\lambda$ moves up in the (V, T)-plane. This puts the point in sector S_4 for which the trajectory moves away from $\mathcal{T}_\lambda$. Hence, the constraint $T_\lambda(V, T) = 0$ represents an unstable manifold.

Therefore, in the limit as $\kappa \to 0$, there are no admissible deflagration waves. This implies that head conduction is necessary for the existence of a deflagration wave. The exception is a deflagration wave behind the lead shock of a ZND detonation because the ahead state of the deflagration is way above the ignition temperature and the profile trajectory follows the partially burned Hugoniot, *i.e.*, $\mathcal{H}_\lambda \cap \mathcal{L}_\lambda$; see Sec. 6.

8 Computation of deflagration speed

The deflagration speed for a solid explosive or propellant with realistic EOS for reactants and products can not be determined analytically. It can, however, be computed numerically. The analysis of the wave profile trajectories in the previous section provides the basis for an iterative shooting algorithm that is described in the next subsection. As an illustrative example, the shooting algorithm is applied to PBX 9501 in the following subsection. While the algorithm works well numerically, the computed deflagration speeds do not compare well with the available data. Aspects of the model contributing to the discrepancy will be discussed.

8.1 Shooting algorithm

The shooting algorithm is a variation of the bisection algorithm used for finding the zero of a function. The unknown variable is the detonation speed D. Rather than evaluate a function, the trajectory of the wave profile ODEs is computed, starting at the ahead state. The key points are: (i) to have a criterion for stopping the integration, and (2) to determine whether D is too large or too small based on where the trajectory terminates.

The algorithm starts with initial bounds or bracket for D. We note that a constant pressure burn and the CJ state give a priori bounds on the deflagration speed; *i.e.*, $D \in [0, D_{CJ}]$. The bracket is refined with a bisection

iteration as follows. With D at the mid-point of the bracket, the wave profile ODEs (14) are integrated until the trajectory meets a termination criterion based on the analysis in the previous section:

1. The trajectory crosses the Rayleigh line $\mathcal{L}_\lambda$; *i.e.*, $-\frac{\mathsf{d}}{\mathsf{d}\zeta}V \le 0$.
   In this case D is too small, as the trajectory if continued would go under sector S_5.

2. The trajectory crosses the line $V = V_{w(1)}$ with $T > T_{w(1)}$.
   In this case D is too large, as the trajectory if continued would go over sector S_5.

   There is a potential issue with trajectories for which $T(\zeta) \to \infty$ or hits the domain boundary of the EOS, before reaching $V = V_{w(1)}$. This can be circumvented by stopping the trajectory if $T \ge T_{\max}$ for some appropriate estimate for the maximum value of T. The exact value of $T_{\max}$ is not critical. It can be taken as a multiple of the deflagration temperature; $T_{\max} = 1.2\,T_{w(1)}$ seems to be adequate.

3. The trajectory $V = V_{w(1)}$ with $T = T_{w(1)}$.
   In this case D is the deflagration speed.

The termination criterion also determines whether D is too small or too large. This allows D to replace one of the end points of the bracket. Thus, the bracket is cut in half. The iteration is repeated until a tolerance is reached on the size of the bracket. The effective tolerance is limited by the accuracy to which the ODEs can be integrated.

Remarks:

(i) Since the ahead state is a critical point, the starting point of the trajectory needs to be offset by a small amount in direction of eigenfunction for stable manifold. Typically, for the eigenfunction $\Delta T/\Delta V$ is large and $\Delta V = 0.001(V_w - V_0)$ is a reasonable choice for the offset.

(ii) For a realistic EOS, P-T equilibrium of reactants and products needs to be calculated numerical with an iterative algorithm. Integrating the ODEs for the trajectory can be significantly degraded unless the P-T equilibrium computation is sufficiently accurate.

(iii) Even using the thermal length scale for the ODEs, Eq. (14a) is near singular for either small m or small Prandtl number ($\nu \ll \kappa/C_r$). In this

case, roundoff error and inaccuracies in evaluating the pressure, $P(V, T, \lambda)$, can degrade the accuracy of computing the wave profile trajectory to such an extent that the criterion for D being too large or too small is incorrect. This would cause the shooting algorithm to break down. The signature of such a failure is when the trajectory for the final value of D does not terminate very close to the weak deflagration state.

8.2 Application to PBX 9501

For shock initiation of a PBX, a key issue is the deflagration speed in a shock compressed explosive triggered by a hot spot; see *e.g.*, [Menikoff, 2009a, Menikoff and Shaw, 2010] and references therein. This can be studied by setting the ahead state of a deflagration wave to be the state behind a lead shock and computing the deflagration speed as a function of the shock pressure.

We use PBX 9501, which is 95 wt% HMX (cyclo-tetramethylene-tetranitromine), as an example to illustrate the use of the shooting algorithm. First, we review the EOS model for PBX 9501 and the transport parameters for HMX. Second, we present numerical results for the deflagration speed. Third, we describe the available experimental data and discuss discrepancies with the results for the model.

Remark: In this section we use a consistent set of high pressure units in which length is in mm, time in μs, mass in mg and temperature in K. The corresponding units for other quantities are then km/s for velocity, g/cm^3 for density, GPa for pressure, J for energy and MJ/kg for specific energy.

8.2.1 Model parameters for PBX 9501 and HMX

The EOS of the reactants is based on shock data and quasi-static isothermal compression data obtained with a diamond anvil cell. We use the EOS model of Menikoff and Sewell [2003]; see [Menikoff, 2007, §4.3.4] and [Menikoff, 2009b] for detailed description of model. The EOS of the products is based on overdriven detonation wave data and release isentrope data [Fritz et al., 1996, Hixson et al., 2000]. We use a sesame table generated by M. Sam Shaw [private communications, LANL 2005]. Properties of this HE model are discussed in [Menikoff, 2008]. Parameters for the reactants and products model EOS are provided in Appendix D.

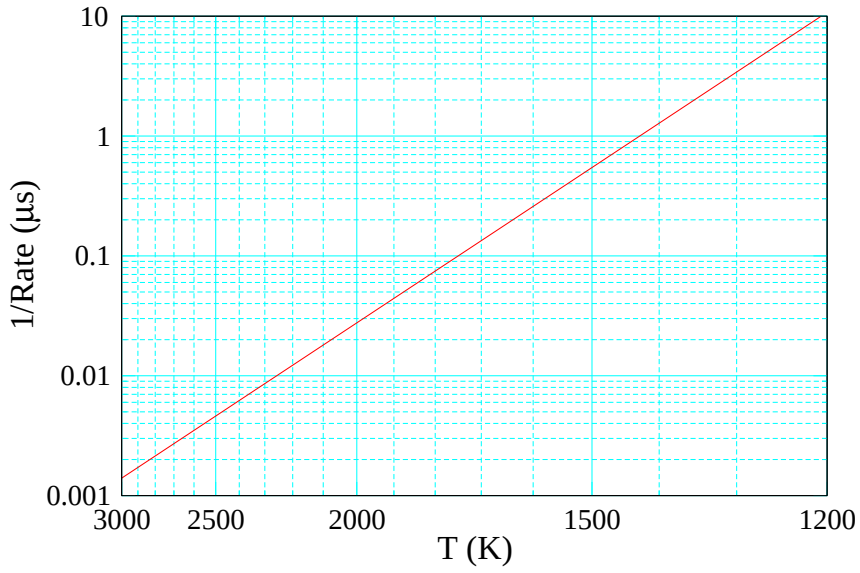

Figure 8: Arrhenius rate for PBX 9501. Inverse rate is on log scale and temperature is on reciprocal scale.

Henson et al. [2002] have shown that the initiation times for HMX over a wide temperature range can be approximately fit with a single global Arrhenius reaction rate. We use parameters slightly adjusted to fit the high temperature regime [Menikoff, 2006] that occurs in the reaction zone of a propagating CJ detonation wave; $T_a = 17.9 \times 10^3\,\mathrm{K}$ and $Z = 2.79 \times 10^5\,\mu\mathrm{s}^{-1}$. The inverse rate as a function of temperature is shown in Fig. 8. Typical deflagration temperatures are about $T = 2500\,\mathrm{K}$; see Fig. 14. At this temperature, the inverse rate is $\tau = 4.6 \times 10^{-3}\,\mu\mathrm{s}$. The deflagration wave time scale is short compared to the inverse rate at the shock temperatures for our calculations; for the strongest shock $P_s = 30\,\mathrm{GPa}$, $T_s = 1360\,\mathrm{K}$ and the inverse rate is $1.85\,\mu\mathrm{s}$. Thus, a deflagration wave in the shock compressed medium is expected to be quasi-steady; *i.e.*, the deflagration speed will vary slowly as the ahead state reacts.

Transport properties of explosives are difficult to measure at high pressure and high temperature. Data for HMX from physical measurements are lim-

ited to atmospheric pressure and temperature less than about 500 K. Added difficulties with temperature dependent measurements stem from a polymorphic phase transition (β to δ) at 438 K and the fact that rapid reaction begins soon after melting at 552 K. Approximate values for some quantities have been obtained through the use of molecular dynamics computations. Representative values of key parameters are listed in the table 1. In general the parameters are not constant but depend on the thermodynamic state; *i.e.*, (V, T).

Table 1: Representative values of constitutive parameters for HMX; see [Menikoff and Sewell, 2002] and references therein.

ρ	.....	density
	1.90 g/cm^3	solid at 293 K and 1 atm
κ	.....	coef. of thermal conduction
	2.6×10^{-10} J/(mm μs K)	liquid at 700 K and 1 atm
C_V	.....	specific heat at constant V
	1.5×10^{-3} (MJ/kg)/K	solid at $T = 1000$ K and 1 atm
ν	.....	coef. of dynamic viscosity
	4.5×10^{-4} GPa μs	liquid at 550 K and 1 atm

Important quantities for deflagration waves can be derived from the parameters in table 1. The coefficient of thermal diffusion, $k = \frac{\kappa}{\rho C_V} = 9.1 \times 10^{-8}$ mm$^2/\mu$s, is very small. The Prandtl number, $Pr = \frac{C_V \nu}{\kappa} = 2.6 \times 10^3$, is much larger than for gases. (In MKS units, $k = 0.26$ W/(m K), $\kappa = 9.1 \times 10^{-8}$ m^2/s and $\nu = 0.45$ Pa s.) The estimated deflagration speed from Eq. (15) is $D = (k/\tau)^{1/2} = 4.5$ m/s. The thermal length scale would then be $\ell = D\,\tau = 0.02\,\mu$m.

For comparison, the reaction zone length of a CJ detonation wave in PBX 9501 is about 25 μm, the reaction time is about 3 ns and the detonation speed is 8.8 km/s; see [Menikoff, 2006]. We note the large disparity of the wave speed and the wave width between a deflagration wave and a detonation wave (about 3 orders of magnitude), even though the reaction time is comparable.

The disparity in the reaction width is crucial for any burn model based on hot spots. A hot spot needs to have enough energy to trigger a deflagration

wave but too little energy for a single hot spot to initiate a detonation wave. The energy needed to trigger a reactive wave is roughly proportional to the wave width.

Remarks:

(i) EOS models for solids are developed for compression and breaks down in expansion; that is, V greater than V_0 by about 10 % or less. Since a deflagration wave is expansive, a typical model is not suitable for calculating a deflagration wave profile when the ahead state is at low pressure. In particular, K_T of the reactants becomes negative and the EOS for a partly burned mixture fails to have a pressure-temperature equilibrium solution. The EOS model can be used when the ahead state is shock compressed to sufficiently high density that the expansion of the deflagration wave stays within the domain of the EOS.

(ii) The thermal conductivity is a key quantity for determining the deflagration speed. Bastea [2002] has calculated κ for the HMX products along the CJ release isentrope using molecular dynamics and Enskog theory. He finds that κ increases roughly linear with pressure. Extrapolated to 0 pressure, the calculation is in agreement with the measured value listed in table 1, and at the CJ pressure it is about 10 times larger. Since the deflagration speed is proportional to the square root of κ, the variation in κ affects the deflagration speed by only a factor of about 3.

(iii) The value of the coefficient of shear viscosity in table 1 was determined from molecular dynamics simulations. For the liquid phase of HMX, the coefficient decreases with temperature; by about 2 orders of magnitude between 550 K and 800 K [Bedrov et al., 2000]. Calculations for HMX products along the CJ release isentrope by Bastea [2002] also give a low value for the viscosity coefficient. These calculation also show that the coefficient increases with pressure. For the solid phase, based on the shock rise time, estimates of an effective viscosity coefficient are on the order of 0.1 GPa μs (1000 Poise). The large value is due to a change in the mechanism for momentum transfer; plasticity rather than diffusion.

(iv) For the HMX reactants (solid phase), C_V varies by about a factor of 2 between room temperature and the temperature of the reaction products; see [Menikoff and Sewell, 2003]. In contrast to a low density gas, the specific heat of the solid at constant P is only a few per cent greater than that at constant V. Moreover, shocked to a high pressure and then reacted, the

products would be at a density comparable to the solid phase, and the specific heat of the reaction products would be comparable to that of the reactants.

(v) To fit accurately thermal ignition data, a multi-step reaction model is needed; see for example, McGuire and Tarver [1981], Henson et al. [2009]. Thermal ignition experiments are at relatively low pressure and low temperatures; typically below 1 kb and below 500 K. Ignition times are on the order of tens of minutes. In contrast, a deflagration wave profile is driven by the high temperature of the reaction products (~ 2500 K), which leads to a very short reaction time, on the order of a few ns. In this regime, we expect the reaction step with the lowest activation energy to be rate limiting and dominate the decomposition. Thus, a single-step rate model, with appropriate Arrhenius parameters, might be suitable for determining the deflagration speed. Later we comment further on this point.

8.2.2 Numerical results

There is considerable uncertainty in the value of parameters in the reactants, products and partly burned mixed phase. To show how deflagration waves are affected, the parameters will be varied and deflagration profiles calculated for shock pressures in the range $10 \le P_s \le 30$ GPa. The lower bound (10 GPa) is to avoid hot partly burned reactants expanding out of the domain of the model EOS. The upper bound (30 GPa) is to limit the shock temperature and hence the reaction rate at the ahead state.

First, we fix the viscosity coefficient and vary κ over a wide range. For $\nu = 6.6 \times 10^{-4}$ GPa μs (which for $\kappa = 1 \times 10^{-8}$ J/(mm μs K) corresponds to $Pr \approx 100$), the deflagration speed and wave width as a function of κ for several shock pressures are shown in Fig. 9. To avoid the tails in the wave profile, we use the region $0.1 \le \lambda \le 0.9$ as a measure of the wave width w. Several points are worth noting: (i) In agreement with the estimate in Eq. (15), both the speed and width are proportional to $\kappa^{1/2}$. (ii) The variation of D with P_s is fairly small. This is largely due to the products EOS, for which the temperature on the deflagration locus is nearly constant; see Fig. 14. (iii) For κ in the expected range, 1×10^{-10} to 1×10^{-8} J/(mm μs K), the deflagration speed and wave width are small; $D \lesssim 10$ m/s compared to the CJ detonation speed of 8.8 km/s, and $w \lesssim 0.3\,\mu$m compared to the CJ detonation reaction zone width of about 25 μm. (iv) For $\kappa \gtrsim 1 \times 10^{-3}$ J/(mm μs K) no deflagration profile exists. The ODE trajectories alway hit the Rayleigh line and go

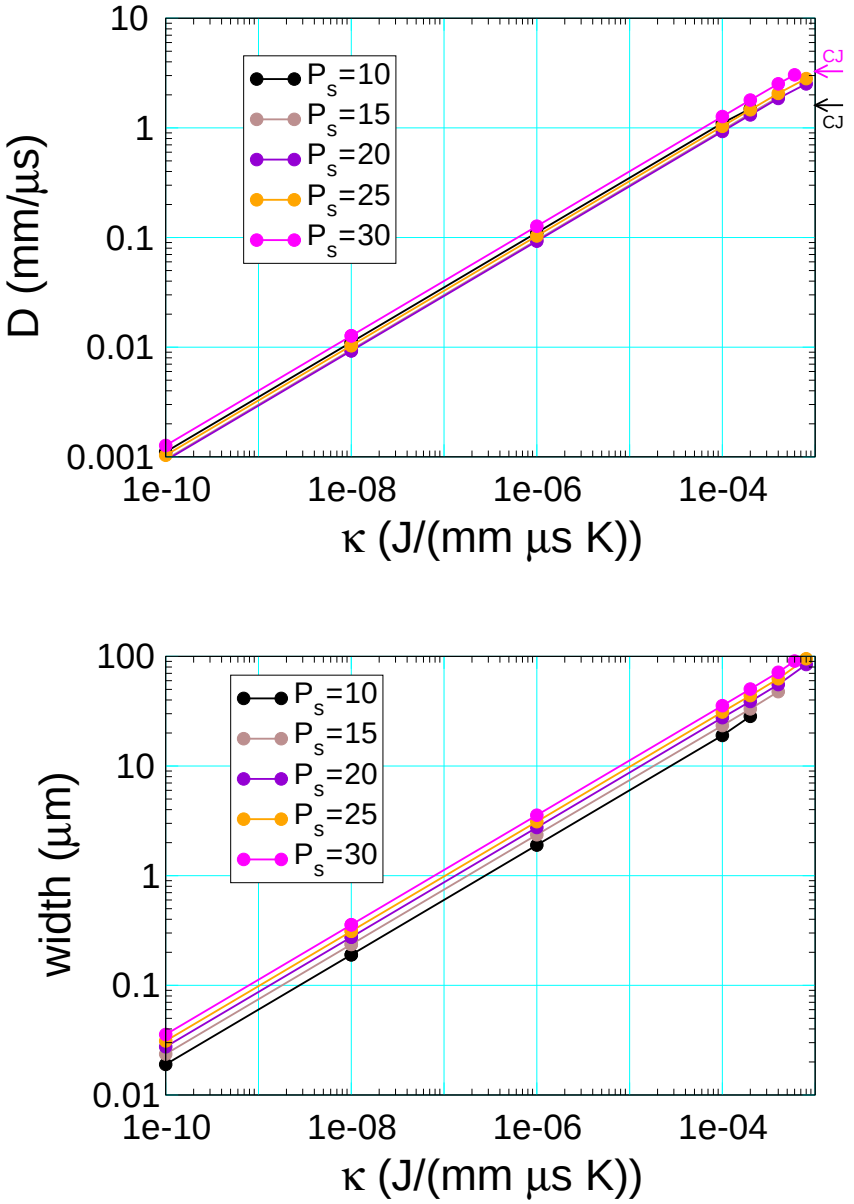

Figure 9: Deflagration speed and wave width as a function of thermal conduction for $\nu = 6.6 \times 10^{-4}\,\mathrm{GPa}\,\mu\mathrm{s}$. Each curve is labeled with the shock pressure to the ahead state. The CJ deflagration speed is indicated by the arrows on the right side for the minimum and maximum P_s. Wave width is from 10 % to 90 % burned.

under section S_5. Since D_{CJ} depends on the shock pressure, the maximum κ depends on P_s. The shooting algorithm succeeds in finding the deflagration speed right up to nearly D_{CJ}.

Spatial profiles of deflagration waves as P_s is varied are shown for the case with $\kappa = 1 \times 10^{-8}\,\mathrm{J/(mm\,\mu s\,K)}$ and $\nu = 6.6 \times 10^{-4}\,\mathrm{GPa\,\mu s}$ in Fig. 10. The x-origin has been shifted to correspond to $\lambda = 0.5$. We observe that the profiles $\lambda(x)$ and $\mathcal{R}(x)$ are very similar for all P_s. The rate peaks near the origin and hence $\lambda \approx 0.5$. The profiles $T(x)$ and $V(x)$ show more variation since the ahead and behind states of the deflagration waves depend on P_s.

The eigenvalues and eigenvectors of the critical point at the behind state are listed in table 2. The negative eigenvalues correspond to the stable manifold. The one with the smaller magnitudes dominates and sets the direction $\mathrm{d}T/\mathrm{d}V$ as the ODE trajectory approaches the behind state. For this case, the eigenvalue corresponding to the rate dominates and $\mathrm{d}T/\mathrm{d}V > 0$. Moreover, $|r_3| = \mathcal{O}(1)$.

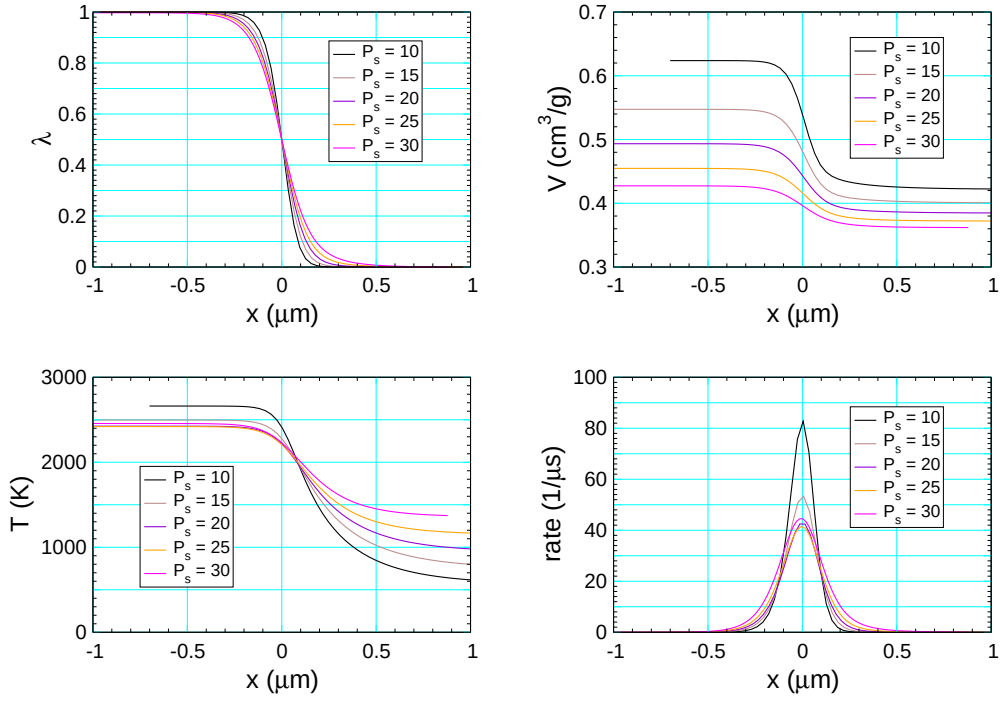

Figure 10: Deflagration wave profiles for $\kappa = 1 \times 10^{-8}\,\mathrm{J/(mm\,\mu s\,K)}$, $\nu = 6.6 \times 10^{-4}\,\mathrm{GPa\,\mu s}$ and a series of shock pressures. The x-origin corresponds to $\lambda = 0.5$.

Table 2: Critical point eigenvalues and eigenvector projected on (V,T)–plane, Eqs. (24–28), at the behind state for $\kappa = 1\times10^{-8}\,\mathrm{J/(mm\,\mu s\,K)}$ and $\nu = 6.6\times10^{-4}\,\mathrm{GPa\,\mu s}$. The ahead state corresponds to state at shock pressure P_s.

P_s GPa	D mm/μs $\times10^{-3}$	λ_1 -	$\mathsf{d}T/\mathsf{d}V$ K g/cm^3 $\times10^3$	λ_2 - $\times10^3$	$\mathsf{d}T/\mathsf{d}V$ K g/cm^3	r_3 -	$\mathsf{d}T/\mathsf{d}V$ K g/cm^3 $\times10^3$
10	11.10	1.76	36.7	-0.95	-3.30	-6.15	2.47
20	9.26	1.43	58.8	-1.88	-1.57	-3.96	3.32
30	12.70	1.26	97.1	-1.51	-2.05	-2.13	5.74

Plots of pairs of thermodynamic variables as κ is varied for fixed $P_s = 20\,\mathrm{GPa}$ and $\nu = 6.6\times10^{-4}\,\mathrm{GPa\,\mu s}$ are shown in Fig. 11. Several points are noteworthy. Though the $\lambda(x)$ profile spreads out with increasing κ, there is only a small variation in $T(\lambda)$ or $T(V)$. Moreover, the deflagration profiles in the (V,P)–plane is close to the Rayleigh line. We later will see that this property occurs when ν is sufficiently small. In addition, for small κ, less than about $1\times10^{-6}\,\mathrm{J/(mm\,\mu s\,K)}$, the pressure is nearly constant. This is due to the low deflagration speed (compared to D_{CJ}) for small κ, and the variation of the pressure on the deflagration locus versus wave speed shown in Fig. 15.

The dashed curves in the $T(V)$ plot correspond to points on the partially burned Hugoniot loci along the Rayleigh line; referred to in the phase-plane analysis section 7 as $\mathcal{H}_\lambda \cap \mathcal{L}_\lambda$ and determined by Eq. (33). The wave profiles (solid curves) lies above the dashed curves because the deflagration wave is driven by head conduction from the behind state. The temperature difference, $T_h(V) - T(V)$, is too large for the perturbative approach in section 6 to apply.

Next we examine the effect of varying ν. For fixed $P_s = 20\,\mathrm{GPa}$ and high and low values of κ, deflagration profiles are shown in Fig. 12 for a series of ν. We observe that there is a small variation of $T(\lambda)$ but a significant variation of $V(\lambda)$ when ν is large. This can have a large affect on $P(\lambda)$. For large ν, the pressure is no longer monotonic. Moreover, the pressure can even exceed the value at the ahead state. Despite the large variation in pressure, there is only a small variation in the detonation speed; see table 3.

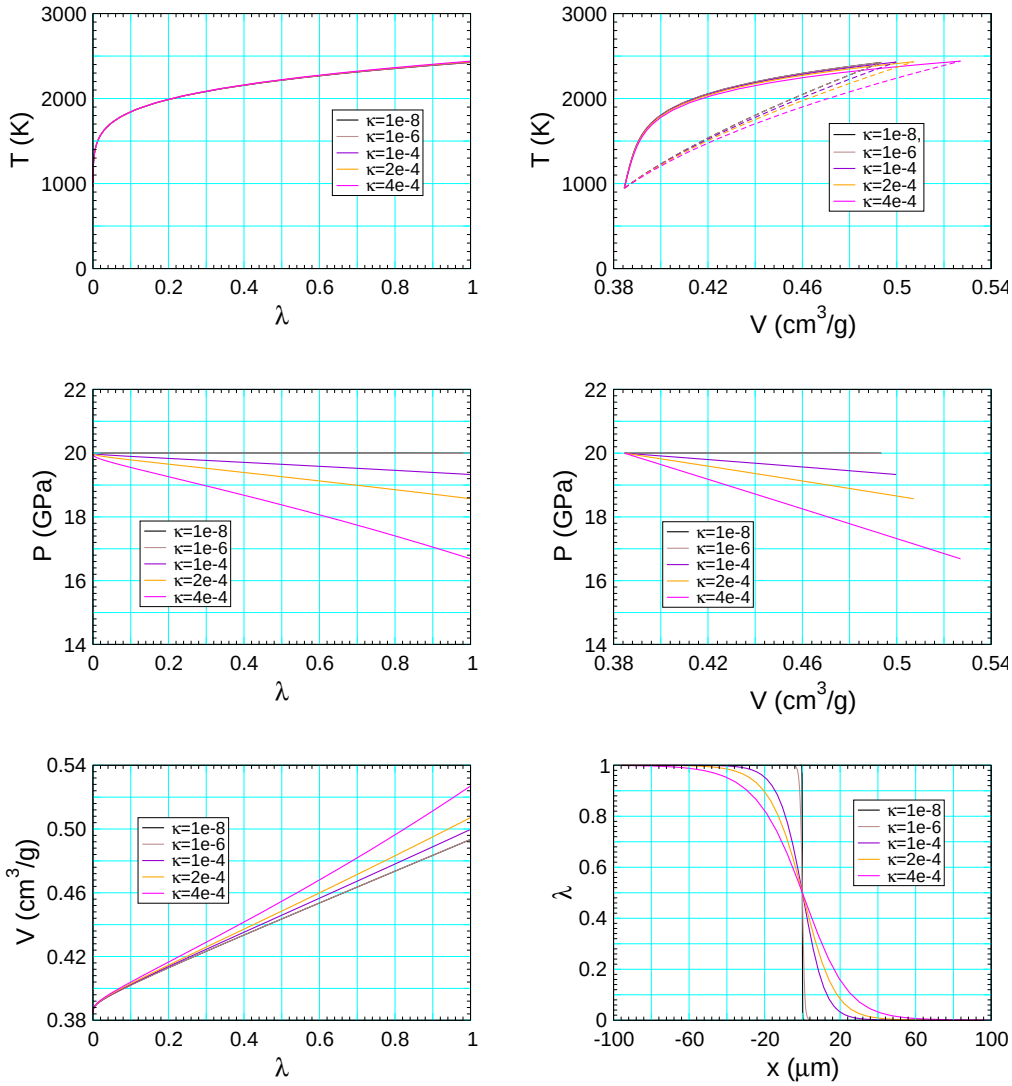

Figure 11: Deflagration wave profiles for $P_s = 20\,\mathrm{GPa}$, $\nu = 6.6 \times 10^{-4}\,\mathrm{GPa}\,\mu\mathrm{s}$, and a series of κ. Dashed curves in $T(V)$ plot correspond to points on the partially burned Hugoniot loci along the Rayleigh line, Eq. (33).

The large viscosity has another anomalous effect. The eigenvalues and eigenvectors of the critical point of the behind state are listed in table 4 for $\kappa = 1 \times 10^{-8}\,\mathrm{J/(mm}\,\mu\mathrm{s\,K)}$ and $\nu = 6.6 \times 10^{-1}\,\mathrm{GPa}\,\mu\mathrm{s}$. We note that

$|\lambda_2| < |r_3|$. Hence, the non-reactive eigenvalue dominates the approach to the behind state. Moreover, for both eigenvalues of the stable manifold $\mathsf{d}T/\mathsf{d}V < 0$. Hence, the temperature is not monotonic at the end of the deflagration wave profile. The temperature decrease occurs in only a very small neighborhood of the behind state.

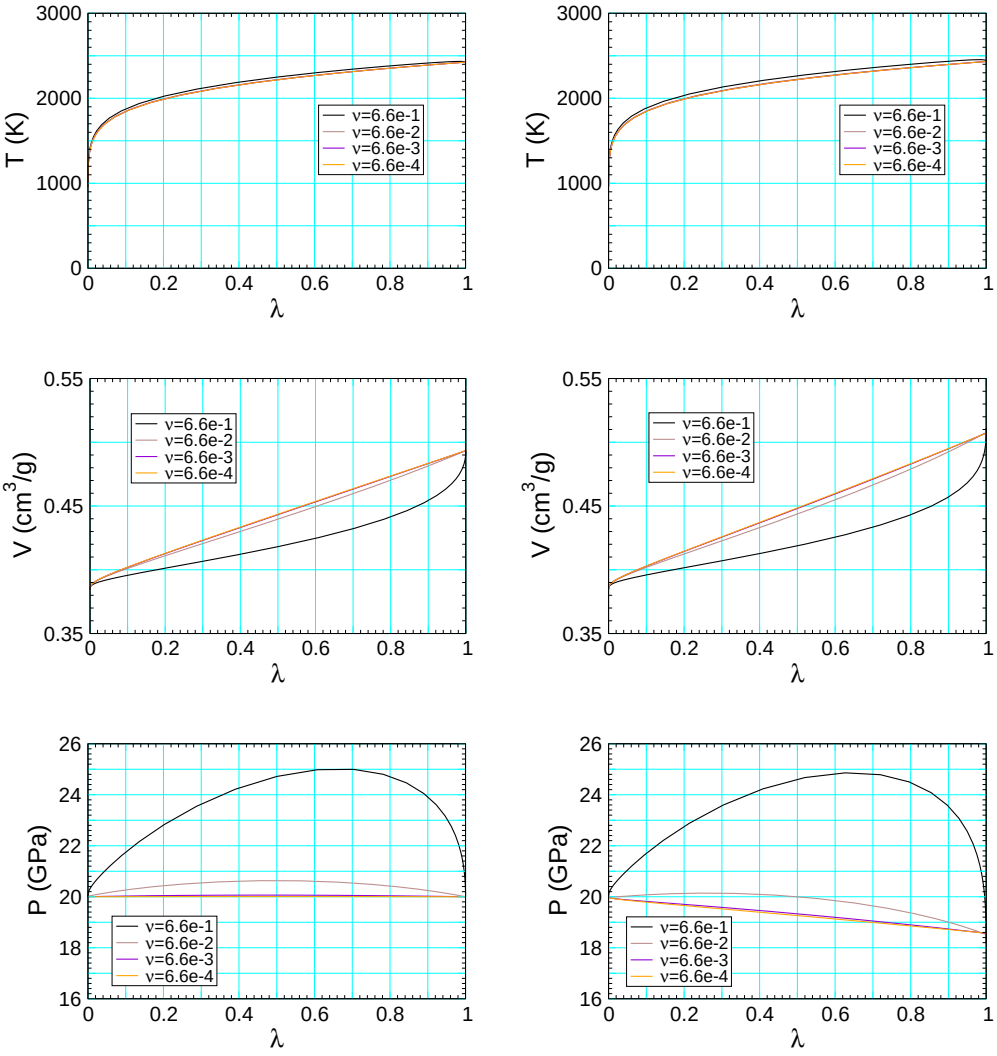

$\kappa = 1 \times 10^{-8}\,\mathrm{J/(mm\,\mu s\,K)}$ $\kappa = 2 \times 10^{-4}\,\mathrm{J/(mm\,\mu s\,K)}$

Figure 12: Deflagration wave profiles for $P_s = 20\,\mathrm{GPa}$ and a series of ν. Plots on the left and right are for small κ and large κ, respectively.

Table 3: Deflagration speed for cases shown in Fig. 12; $P_s = 20\,\text{GPa}$ with small and large κ of 1×10^{-8} and $2 \times 10^{-4}\,\text{J/(mm}\,\mu\text{s K)}$, respectively. Units for ν and D are $\text{GPa}\,\mu\text{s}$ and $\text{mm}/\mu\text{s}$, respectively.

ν	small κ	large κ
6.6×10^{-1}	10.09×10^{-3}	1.46
6.6×10^{-2}	9.38×10^{-3}	1.33
6.6×10^{-3}	9.28×10^{-3}	1.31
6.6×10^{-4}	9.27×10^{-3}	1.31

Table 4: Critical point eigenvalues and eigenvector projected on (V, T)–plane, Eqs. (24–28), at the behind state for $\kappa = 1 \times 10^{-8}\,\text{J/(mm}\,\mu\text{s K)}$ and $\nu = 6.6 \times 10^{-1}\,\text{GPa}\,\mu\text{s}$. The ahead state corresponds to state at shock pressure P_s.

P_s GPa	D mm/μs $\times 10^{-3}$	λ_1 -	$\mathsf{d}T/\mathsf{d}V$ K g/cm^3 $\times 10^3$	λ_2 -	$\mathsf{d}T/\mathsf{d}V$ K g/cm^3 $\times 10^3$	r_3 -	$\mathsf{d}T/\mathsf{d}V$ K g/cm^3 $\times 10^3$
15	10.6	1.53	109.	-1.31	-1.07	-3.93	-8.21
20	10.1	1.41	111.	-1.62	-0.99	-3.34	-5.35
25	10.9	1.32	138.	-1.71	-1.01	-2.65	-3.85

For sufficiently small ν, less than $6.6 \times 10^{-3}\,\text{GPa}\,\mu\text{s}$ for the values of κ in Fig. 12, the variation of the profiles is negligible; *i.e.*, the wave profiles converge as $\nu \to 0$. Alternatively, the deflagration speed converges for small Prandtl number. As previously noted, for fixed Prandtl number, the wave profile ODEs (14) depend on $\kappa\mathcal{R}/m^2$. Thus, for sufficiently small ν the deflagration speed depends on $(\kappa\mathcal{R})^{1/2}$ and the wave width on κ/D. Hence, the variation of a deflagration wave profile when the rate is multiplied by a constant can be determined instead by scaling κ with $\mathcal{R}$ fixed.

For a typical deflagration wave, such as for PBX 9501, ν and κ are sufficiently small for the deflagration speed to be small and the pressure nearly constant. However, it is important to note that these standard properties depend on parameter values, and are not general properties of the wave profile ODEs.

Remarks:

(i) An alternative approach for determining the deflagration speed has previously been used; see for example, [Reaugh, 2004] and [Handley, 2011, sec. 6.3]. A simulation is run using a reactive hydro code with heat conduction. It is initialized with a hot spot or a temperature boundary condition and run until a steady deflagration wave is propagating. The time-dependent simulation is computationally intensive since the very narrow reaction zone must be resolved and the length of run needed to reach steady state is a large number of reaction zone widths. Moreover, an explicit algorithm is not practical as the heat conduction term in the PDEs is parabolic and the stable time step is proportional to the square of the cell size rather than the linear dependence (CFL condition) required by the hyperbolic fluid equations. Numerical algorithms for ODEs with adaptive time steps are much more straight forward. We postpone comments on how the two approaches compare till the next subsection.

(ii) Many reactive-hydro codes use artificial viscosity for the numerical dissipation needed to capture shock fronts. The viscous pressure has the form $Q = -\tilde{\nu}\rho c(\Delta x)\partial_x u$, where $\tilde{\nu}$ is a dimensionless coefficient on the order of 1. The effective viscosity coefficient is $\nu \sim \rho c(\Delta x)$. For shocked PBX 9501, $\rho c \sim 10\,(\mathrm{g/cm^3})\cdot(\mathrm{mm}/\mu\mathrm{s})$. For a very fine mesh with $\Delta x = 0.1\,\mu\mathrm{m}$, this gives a viscous coefficient of $\nu \sim 10^{-3}\,\mathrm{GPa}\,\mu\mathrm{s}$, which is larger than the value we have used for the wave profile ODEs. Fortunately, for reasonably small values of the viscous coefficient, the trajectory is sufficiently close to the Rayleigh line that the profile is insensitive to the exact value of the coefficient; see subsection 7.5.

8.2.3 High pressure data

A diamond anvil cell can be used to compress HMX powder up to a high static pressure. A hot spot generated by a narrow laser beam can then be used to initiate a deflagration wave. Using this technique Esposito et al. [2003] and Zaug et al. [2009] have measured the deflagraion speed of HMX at room temperature as a function of pressure up to the CJ detonation pressure of PBX 9501; about 35 GPa. The data shows that the deflagration speed varies as $D \propto P^n$ with $n \approx 0.8$.

The numerical results for the deflagration speed in the previous subsection does not show a power-law pressure dependence. Nor is the estimated

deflagration speed for the model, Eq. (15), compatible with a P^n behavior since none of the parameters are strongly pressure dependent and the deflagration temperature, shown in Fig. 14, has a very weak dependence on pressure.

At low pressures, the deflagration speed of propellants and HMX based explosives have a similar power-law pressure dependence [Atwood et al., 1999, Maienschein et al., 2004]. This can be explained by a simple model with a two-step reaction; see for example, Ward et al. [1998]. The first step is vaporization or pyrolysis which has a small heat release. The second step is a gas-phase reaction with a large heat release. A key feature of the deflagration profile for the two-step model, is a flame standoff distance; convective-diffusion zone between the solid reactants and the gas-phase reaction front. In effect, the deflagration speed is controlled by the rate of vaporization which is determined by the heat diffusion across the convective-diffusion zone. The width of the diffusion zone is pressure dependent due to the compressibility of the unreacted gas. Since the temperature at the ends of the diffusion zone (reactant surface and flame front) are approximately constant, the heat flux and hence the deflagration speed is pressure dependent.

The single-step reaction model used in the previous subsection neglects the gas-phase diffusion zone. Considering the uncertainty in the model parameters, the deflagration speed predicted with the single-step rate is comparable with the maximum deflagration speed measured in the experiments. Very likely the single-step rate model gives an upper bound on the deflagration speed. This bound on the deflagration speed is about a factor of 100 lower than the detonation speed.

Two previous calculations of the pressure dependence of the HMX deflagration speed are noteworthy. Reaugh [2004] used a hydro simulation approach with the three-step McGuire and Tarver [1981] reaction model. He found a power-law pressure dependence to the deflagration speed with $n = 0.38$. At a high pressure of 30 GPa, the deflagration speed of 10 m/s is comparable to the result in the previous section. Handley [2011, sec. 6.3] also used a hydro simulation approach, but with a single-step Arrhenius reaction. She found the deflagration speed decreased from 7 m/s at 2 GPa to 1 m/s at 20 GPa. Again the deflagration speed is comparable to the results in the previous section. The EOS and other model parameters are not exactly the same for these studies. Consequently, one would not expect the computed deflagration speeds to agree. Yet the deflagration speeds are all in the range

of 1 to 10 m/s. A key point is that the computed deflagration speeds and the measured deflagration speed, while subject to uncertainties, are all much lower than the detonation speed.

Remarks:

(i) There are anomalies in the HMX deflagration speed data [Esposito et al., 2003, Zaug et al., 2009], such as a dependence on the grain size and a discontinuous jump in deflagration speed at a pressure of about 10 GPa. The former is not understood, and surprising since at pressures significantly over the yield strength one does not expect any porosity or grain packing effects. The latter is similar to a jump in deflagration speed that has been observed in propellant. For propellants, the jump in deflagration speed is believed to be due to de-consolidation [Fifer and Cole, 1981] which leads to an enhanced heat transfer from convective flow; *i.e.*, two-phase flow in the deflagration zone in which hot products flow around the reactant grains.

(ii) Mechanisms for generating hot spots, such as void collapse by a shock wave, also lead to high vorticity in the neighborhood of the hot spot. Possibly this leads to an enhance heat transfer, which may be modeled with an increased 'turbulent' thermal diffusion coefficient; see [Karpenko et al., 2008].

(iii) There are differences in the measured deflagration speed between the two experiments of [Esposito et al., 2003, Zaug et al., 2009]. These are believed to be due to the use of different criterion for determining the position of the deflagration front from the speckle pattern of light reflected from the explosive surface; either first change in the speckle pattern or extinction of the speckle pattern when the reaction completes. The latter criterion gives a lower deflagration speed, and is believed to be more accurate.

9 Implication for shock initiation

The low deflagration speed, compared to the detonation speed, has implications for burn models based on the ignition and growth concept. The burn rate due to deflagration waves triggered by hot spots (reactive wavelets) is proportional to the number density of hot spots times the deflagration speed. With a low deflagration speed, a large number density is needed to achieve a sufficiently large rate to drive a shock-to-detonation transition.

Shock initiation of a PBX is sensitive to its porosity. This leads to the hypothesis that hot spots are formed when a shock passes over and collapses a pore. The phenomenon of shock desensitization [Campbell and Travis, 1986], in which the pressure behind a weak shock squeezes out pores, supports this hypothesis. For a PBX with a given initial density, and hence porosity, the number density of potential hot spots is limited by the pore size; *i.e.*, small pores are required for a large number density when the total pore volume is fixed.

Pores that are too small, even if they generate hot spots, do not have sufficient energy to trigger a reactive wavelet. Since hot spots are smaller than the pores that generate them, the thermal length scale, Eq. (15), can be used as an estimate for the minimum pore size that can give rise to a reactive wavelet. The results of the previous subsection then imply that the minimal pore size is on the order of $0.1\,\mu$m. This is much smaller than the average grain size for PBX 9501; about $100\,\mu$m. Recent measurements with ultra-small-angle neutron scattering by Mang et al. [2010] show that there are a large number of pores of the necessary size. These are very likely solvent inclusion or imperfections within an HMX grain, rather than within the binder between grains.

We note that there is also an upper limit on the pore size. To get a high volume fraction of explosive (*i.e.*, small amount of binder), a PBX utilizes a bimodal distribution of grains in order that the small grains fill in the intergranular pores between the large grains. For PBX 9501, the pores are less than $10\,\mu$m. This places an upper limit on the width of a deflagration wave, which then gives rise to a limit on the coefficient of thermal conduction for hot-spot models; $\kappa < 10^{-6}\,\mathrm{J}/(\mathrm{mm}\,\mu\mathrm{s}\,\mathrm{K})$. This in turn limits the deflagration speed to be much less than the detonation speed.

Reactive burn modeling of PBXs has been held back by the inability to measure experimentally the small spatial and temporal scales of hot spots and the interactions of the deflagration wavelets they generate. With the advances in computing power, it is natural to consider using meso-scale simulations of a PBX, which resolve grains and hot spots, as numerical experiments to better understand the physical processes in a shock-to-detonation transition; in particular, the feedback between the energy released by deflagration wavelets triggered by the hot spots and the lead shock strength. The small hot-spot length scale and the slow deflagration speeds make such simulations a very challenging computational problem. Very likely subgrid models will

be needed to generate the hot spots and to propagate the deflagration fronts.

Successfully demonstrating a shock-to-detonation transition with meso-scale simulations would place the ignition & growth concept on a firmer foundation. It might even lead to the capability for predicting the behavior of a PBX from properties of its components (explosive grains and binder) plus a statistical description of grain sizes and pore distribution.

Appendix A. Ideal explosive EOS

An ideal explosive EOS provides an illustrative example that has been widely used to study qualitative properties of deflagration and detonation waves. As a mixture EOS, it is defined by (see *e.g.*, Fickett and Davis [1979, p. 18])

$$P(V, e, \lambda) = (\gamma - 1)(e + \lambda\, q)/V \ , \tag{A.1a}$$
$$T(V, e, \lambda) = (e + \lambda\, q)/C_V \ , \tag{A.1b}$$
$$\widetilde{P}(V, T, \lambda) = (\gamma - 1)C_V\, T/V \ , \tag{A.1c}$$

where the parameters γ, q and C_V represent the adiabatic exponent, the chemical energy release per unit mass, and the specific heat, respectively. This is equivalent to a P–T equilibrium mixture of an ideal gas reactants EOS

$$P_r(V, e) = (\gamma - 1)e/V \ , \tag{A.2a}$$
$$T_r(V, e) = e/C_V \ , \tag{A.2b}$$
$$\widetilde{P}_r(V, T) = (\gamma - 1)C_V\, T/V \ , \tag{A.2c}$$

and an ideal gas products EOS

$$P_p(V, e) = (\gamma - 1)(e + q)/V \ , \tag{A.3a}$$
$$T_p(V, e) = (e + q)/C_V \ , \tag{A.3b}$$
$$\widetilde{P}_p(V, T) = (\gamma - 1)C_V\, T/V \ . \tag{A.3c}$$

The chemical energy or heat release q is the offset of the energy origin for the products relative to the reactants. Moreover, the adiabatic index and specific heat is the same for the reactants, the products and the mixture. Furthermore, $K_T = P$ and $\Gamma = \gamma - 1$, for the reactants, the products and the mixture.

In P–T equilibrium the reactant and products specific volumes are

$$V = V_r = V_p = (\gamma - 1)C_V\, T/P \ , \tag{A.4}$$

and the specific energies are

$$\begin{aligned} e = C_V\, T - \lambda\, q \quad &= \lambda\, e_p + (1 - \lambda)\, e_r \ , \\ e_p = C_V\, T - q \quad &= e - (1 - \lambda)\, q \ , \\ e_r = C_V\, T \quad &= e + \lambda\, q \ . \end{aligned} \tag{A.5}$$

The key λ derivatives, for the partly burned Hugoniot loci and the wave profile, are

$$\left(\frac{\partial \widetilde{P}}{\partial \lambda}\right)_{V,T} = 0 \ , \tag{A.6a}$$

$$\left(\frac{\partial e}{\partial \lambda}\right)_{V,T} = -q \ . \tag{A.6b}$$

Needless to say, the simplified relations for all the thermodynamic derivatives greatly facilitates mathematical analysis of the ODEs for a deflagration profile.

In particular, the analysis can take advantage of the special relation for an ideal explosive that the enthalpy,

$$h = e + P\,V = \gamma C_V\,T - \lambda\,q \ , \tag{A.7}$$

is linear in both T and λ, and independent of V. Consequently, $h_p - h_r = -q$ is constant. The isentropic sound speed can be expressed in terms of h and q as

$$c^2 = \gamma PV = \gamma(\gamma-1)\,C_V\,T \tag{A.8a}$$

$$= (\gamma-1)\cdot(h + \lambda\,q) \ . \tag{A.8b}$$

Moreover, the isothermal sound speed can be expressed as

$$c_T^2 = P\,V = \frac{\gamma-1}{\gamma}\,(h + \lambda\,q) \ . \tag{A.9}$$

The Hugoniot equation can be expressed in terms of h as

$$h = h_0 + \tfrac{1}{2}\,(V_0 + V)\cdot(P - P_0) \ . \tag{A.10}$$

Consequently, for a constant pressure deflagration $h = h_0$. Therefore, the temperature and the sound speed are given by $T = T_0 + q/(\gamma\,C_V)$ and $c^2 = c_0^2 + (\gamma-1)\,q$, respectively. Moreover, for a convex EOS, h is monotonically decreasing on the deflagration locus as P decreases. Consequently, the temperature and the sound speed also decrease.

The entropy for the mixture can be expressed as

$$S = C_V \ln\Big[(P_{\rm ref}/P)^{\gamma-1}(T/T_{\rm ref})^{\gamma}\Big] + (\Delta S_{\rm ref})\,\lambda + S_{r,\rm ref} \ , \tag{A.11a}$$

where $\Delta S_{\text{ref}} = S_p - S_r$ at the reference state $(P_{\text{ref}}, T_{\text{ref}})$. The reactant and products entropy have the same form with a relative shift or offset;

$$S_r = C_V \ln\Big[(P_{\text{ref}}/P)^{\gamma-1}(T/T_{\text{ref}})^{\gamma}\Big] + S_{r,\text{ref}} \ , \tag{A.11b}$$

$$S_p = C_V \ln\Big[(P_{\text{ref}}/P)^{\gamma-1}(T/T_{\text{ref}})^{\gamma}\Big] + S_{p,\text{ref}} \ . \tag{A.11c}$$

It follows for the Gibbs free energy, $G(P,T) = h - T\,S$, that the difference between the reactants and products is given by

$$\Delta G = G_p - G_r = \Delta h - T\Delta S = -\Big[q + T(S_{p,\text{ref}} - S_{r,\text{ref}})\Big] \ . \tag{A.12}$$

When $S_{p,\text{ref}} \geq S_{r,\text{ref}}$, as physically expected, $\Delta G < 0$. Hence, the products are thermodynamically stable and the reactants only meta-stable. Moreover, it is easily checked that the fundamental thermodynamic identity, $\mathsf{d}e = -P\,\mathsf{d}V + T\,\mathsf{d}S + (\Delta G)\,\mathsf{d}\lambda$, is satisfied.

As a result of Eq. (A.4), we find

$$\left(\frac{\partial S}{\partial \lambda}\right)_{V,T} = \Delta S_{\text{ref}} \ , \tag{A.13a}$$

$$\left(\frac{\partial S}{\partial \lambda}\right)_{V,e} = \Delta S_{\text{ref}} + q/T \ , \tag{A.13b}$$

which directly verify Eqs. (C.31) and (C.32). Also, the leading term in the entropy equation for the reactants, products and mixture can be reexpressed as

$$\ln\Big[(P_{\text{ref}}/P)^{\gamma-1}(T/T_{\text{ref}})^{\gamma}\Big] = \ln\Big[(P/P_{\text{ref}})(V/V_{\text{ref}})^{\gamma}\Big] \ , \tag{A.14}$$

which determines an isentrope in the (P,T)-plane or (V,P)-plane.

Two extensions are analytically solvable for the mixture and somewhat more realistic. First, by allowing different values of C_V and γ for the reactants and products, the mixture EOS can account for a chemical reaction that increases the number of moles for the products compared to the reactants. Moreover, V_p would not equal V_r, and $(\partial_\lambda P)_{V,T}$ would be non-zero. Second, by using a stiffened gas EOS (see *e.g.*, [Menikoff, 2007, § 4.3.2]), one can account for the high sound speed of solid reactants. Even so, the thermal properties of these simplified EOS would not be accurate for solid explosives. This is important since chemical reactions, such as exemplified by the Arrhenius rate with high activation temperature, are very temperature sensitive.

Appendix B. Gaseous & solid deflagration loci

We use PBX 9501 to illustrate differences between an ideal explosive EOS and a realistic solid EOS. The realistic EOS is described and compared with experimental data in Menikoff [2006, 2008]; see Appendix D for model parameters. For the ideal explosive EOS, parameters were chosen to match the CJ detonation state ($P_{CJ} = 35\,\text{GPa}$) and the CJ release isentrope. The parameters are listed below.

Table 5: Ideal HE EOS parameters for PBX 9501

ρ_0	1.83	g/cm^3	initial density
γ	3.1	–	adiabatic index
q	4.5	MJ/kg	chemical energy released per unit mass
C_V	0.002	$\text{MJ}\,(\text{kg}\,\text{K})^{-1}$	specific heat at constant volume

The CJ isentrope for both EOS are shown in Fig. 13. We note that they agree well in the (V, P)–plane but not in the (P, T)–plane. This is because the behavior of the high density products is well described by an adiabatic

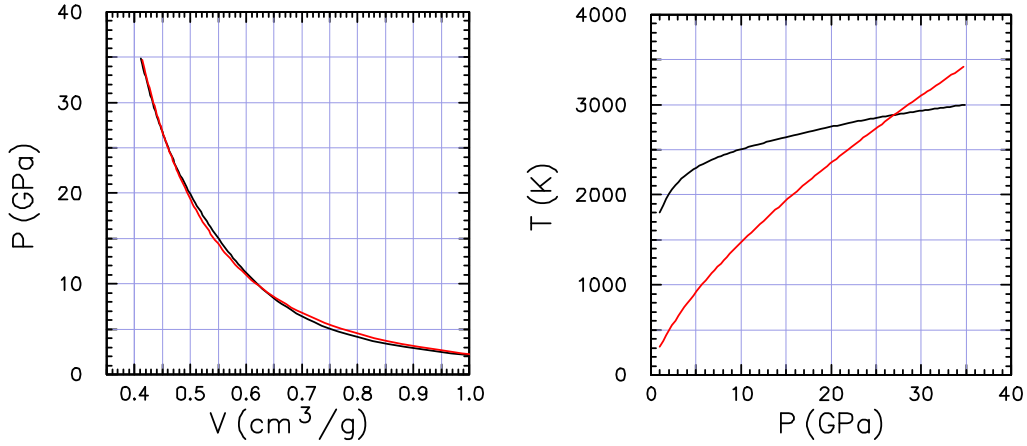

Figure 13: CJ isentrope for PBX 9501. Red curves correspond to ideal explosive EOS and black curves to realistic solid EOS.

index of about 3. The temperature along the release isentrope is given by

$$T(V) = T_{CJ} \cdot \exp\Big[- \int_{V_{CJ}}^{V} \mathsf{d}V \, \frac{\Gamma(V)}{V} \Big] \ .$$

For an ideal EOS, $\Gamma = \gamma - 1$. This is not a good approximation for a gas at high density. To summarize, the ideal explosive products EOS does well on the mechanical properties but poorly on the thermal properties. The reason is that for a gas at low density $C_P/C_V = \gamma$ whereas as at high density it is more fluid like and C_p is only a few per cent higher than C_V.

A key issue for shock initiation of a PBX, is the deflagration speed in the shock compressed and heated reactants triggered by a hot spot. The deflagration loci from a shocked state at several pressures are shown in Fig. 14. There are several important differences between a realistic and an ideal explosive.

First, we note that for the ideal EOS, the sound speed at the initial state is very low. Consequently, at the high pressures of interest, the shock locus is in the strong shock limit with compression ratio given by

$$V_s/V_0 = (\gamma - 1)/(\gamma + 1) \ .$$

To make the locus in the (V, P)–plane appear continuous, the initial sound speed, $c_0 = (\gamma \, P_0 \, V_0)^{1/2}$, is increased by raising the initial pressure from 1×10^{-4} to 0.1 GPa. For both EOS, the deflagration loci for the different shock pressures nearly overlap. There is an offset in V for the deflagration loci corresponding to each EOS due to the different shock compression ratio, and hence ahead state for the deflagration loci.

The deflagration loci in the (P, T)–plane are notably different. For the realistic EOS, there is very little temperature variation along a deflagration locus and between loci corresponding to different shock pressures. In contrast, for the ideal EOS, along a deflagration locus the temperature decreases monotonically with decreasing pressure. Furthermore, the temperature for a constant pressure deflagration increases with shock pressure. This is due to the shock temperature increasing with pressure, and the property of an ideal EOS that the temperature change for a constant pressure deflagration is given by

$$T(P_0) - T_0 = q/(\gamma \, C_V) \ ,$$

and is independent of the initial state.

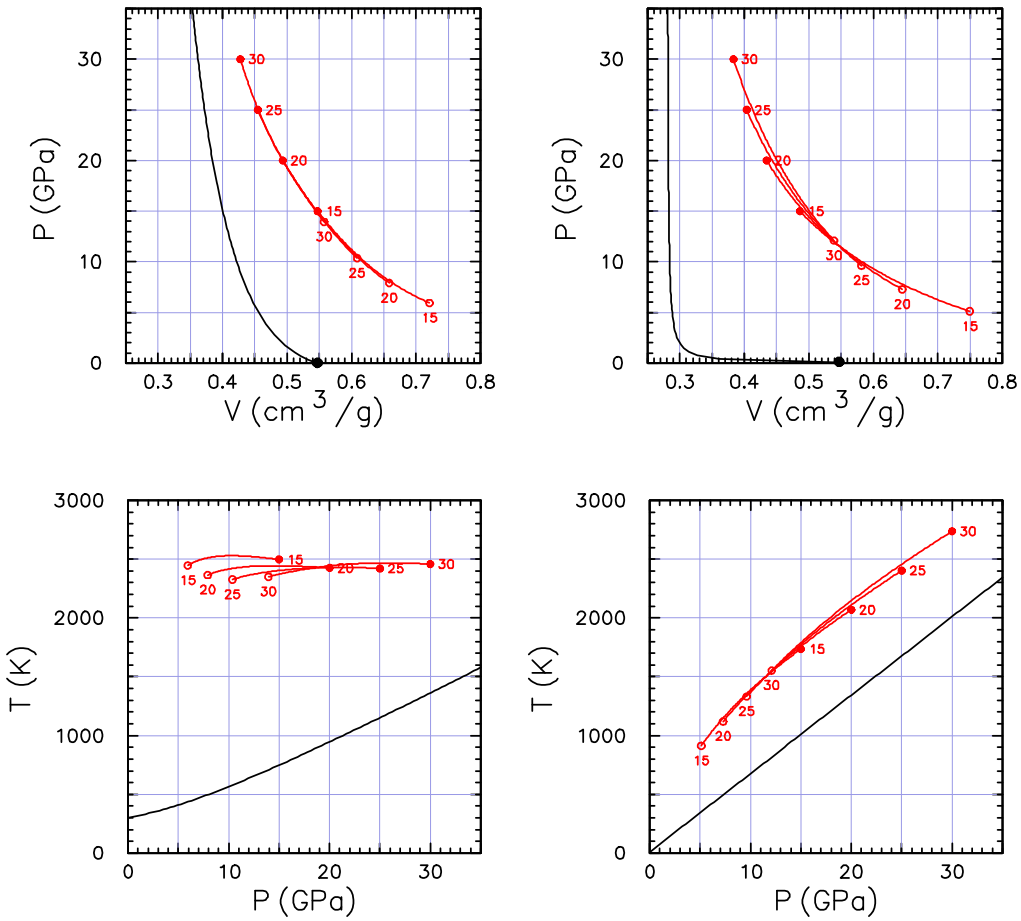

Figure 14: Deflagration loci from shocked state in PBX 9501. Left figures correspond to realistic solid EOS, and right figures to ideal explosive EOS. Black curves are shock loci of reactant and red curves are deflagration loci. Solid circle denotes constant pressure point and open circle CJ deflagration state. Both symbols are labeled with the shock pressure.

The difference in the variation of the temperature along the deflagration locus can be understood from the thermodynamic relation

$$\mathrm{d}T/T = -\Gamma \mathrm{d}V/V + \mathrm{d}S/C_V \ .$$

On the weak branch, both V and S increase as P decreases. Therefore, the terms on right hand side have the opposite sign and T can either increase or decrease. We also note that for both EOS, when $P_s < P_{CJ}$, the deflagra-

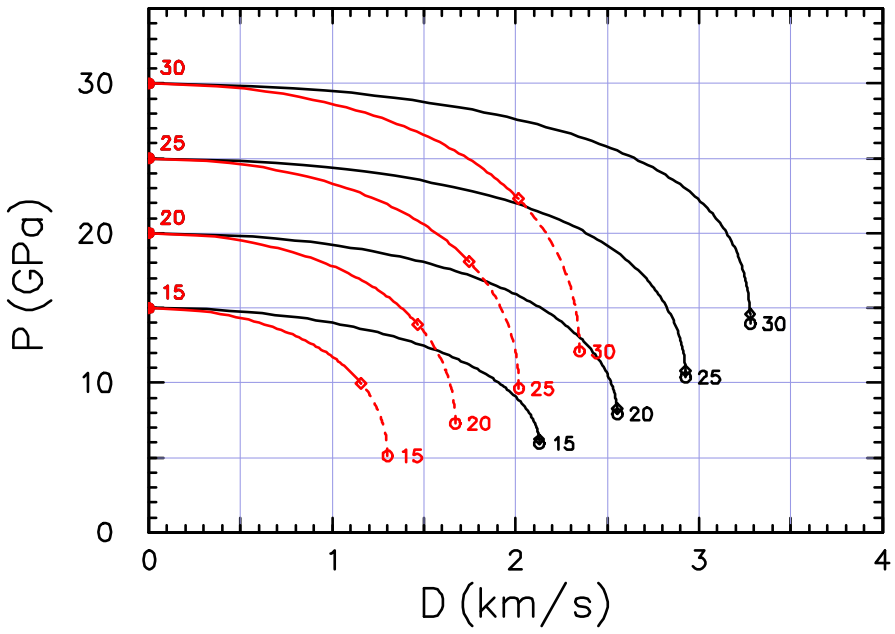

Figure 15: Deflagration loci in (D, P)-plane from shocked state for PBX 9501. Black and red curves are for realistic EOS and ideal explosive EOS, respectively. Solid circle denotes constant pressure deflagration state and open circle CJ deflagration state. Both symbols are labeled with the shock pressure. Diamond marks the sonic point with respect to c_T. Dashed portion of loci are supersonic with respect to c_T.

tion temperature is less than the CJ detonation temperature; 3000 K for the realistic EOS and 3420 K for the ideal EOS.

The different shock compression ratio for the two EOS has important qualitative effects shown in Fig. 15. For the realistic EOS, the CJ deflagration speed is larger than that of the ideal explosive EOS. For a fixed deflagration speed, the change in pressure across the deflagration wave is smaller for the realistic EOS. We also note that for a fixed deflagation speed, ΔP decreases as the ahead state shock pressure increases. For the realistic EOS and a shock pressure of 30 GPa, $\Delta P < 1$ GPa up to a deflagration speed of 1 km/s. Another difference, due to the thermal properties, is that a larger portion of the deflagration loci for the ideal explosive EOS is supersonic with respect to the isothermal sound speed.

Appendix C. Thermodynamic relations

An equilibrium mixture EOS is used for the partly burned explosive. The pressure equilibrium conditions are

$$\widetilde{P}(V,T) = \widetilde{P}_r(V_r,T) = \widetilde{P}_p(V_p,T) \ , \tag{C.1a}$$

$$V = \lambda\, V_p + (1-\lambda)\, V_r \ , \tag{C.1b}$$

where the subscripts p and r denote the products and reactants variables, respectively, and λ is the mass fraction of the products. Following Menikoff [2007, § 4.6] thermodynamic quantities of the mixture are derived in terms of those of the components.

The isothermal sound speed of the mixture can be obtained by taking the derivative with respect to V at fixed λ and T of Eq. (C.1). This yields a pair of simultaneous equations

$$\frac{K_{T,p}}{V_p}\frac{\mathsf{d}}{\mathsf{d}V}V_p - \frac{K_{T,r}}{V_r}\frac{\mathsf{d}}{\mathsf{d}V}V_r = 0 \ , \tag{C.2a}$$

$$\lambda\,\frac{\mathsf{d}}{\mathsf{d}V}V_p + (1-\lambda)\,\frac{\mathsf{d}}{\mathsf{d}V}V_r = 1 \ , \tag{C.2b}$$

where $K_T = -V\frac{\partial \widetilde{P}}{\partial V} = \rho\, c_T^2$ is the isothermal bulk modulus. Hence,

$$\frac{\mathsf{d}}{\mathsf{d}V}V_p = \frac{K_{T,r}/V_r}{\lambda K_{T,r}/Vr + (1-\lambda)K_{T,p}/V_p} \ , \tag{C.3a}$$

$$\frac{\mathsf{d}}{\mathsf{d}V}V_r = \frac{K_{T,p}/V_p}{\lambda K_{T,r}/Vr + (1-\lambda)K_{T,p}/V_p} \ . \tag{C.3b}$$

Substituting into the equation for the mixture bulk modulus,

$$K_T = V\,\frac{K_{T,p}}{V_p}\frac{\mathsf{d}}{\mathsf{d}V}V_p \ , \tag{C.4}$$

the result can be expressed as

$$\frac{V}{K_T} = \frac{\lambda\, V_p}{K_{T,p}} + \frac{(1-\lambda)\, V_r}{K_{T,r}} \ . \tag{C.5}$$

The isentropic bulk modulus can be obtained from the thermodynamic relation,

$$K_S = K_T + \frac{\Gamma^2}{V} C_V \, T \ , \tag{C.6}$$

in terms of the specific heat $C_V = \left(\frac{\partial e}{\partial T}\right)_{V,\lambda}$ and the Grüneisen coefficient $\Gamma = V\left(\frac{\partial P}{\partial e}\right)_{V,\lambda}$.

The mixture specific heat can be derived by taking the derivative with respect to T, at fixed V and λ, of the mixture energy

$$e(V,T) = \lambda \, e_p(V_p,T) + (1-\lambda) \, e_r(V_r,T) \ . \tag{C.7}$$

First one has to determine $\frac{\mathsf{d}}{\mathsf{d}T} V_p$ and $\frac{\mathsf{d}}{\mathsf{d}T} V_r$ by solving the simultaneous equations obtained by taking the derivative of the pressure equilibrium conditions, Eq. (C.1). Using the thermodynamic relations,

$$\left(\frac{\partial \widetilde{P}}{\partial T}\right)_{V,\lambda} = \frac{\Gamma}{V} C_V \ , \tag{C.8}$$

applied to the reactants and products, the result is

$$\lambda^{-1} \frac{\mathsf{d}}{\mathsf{d}T} V_r = -(1-\lambda)^{-1} \frac{\mathsf{d}}{\mathsf{d}T} V_p = \frac{\Gamma_r C_{V,r}/V_r - \Gamma_p C_{V,p}/V_p}{(1-\lambda) K_{T,p}/V_p + \lambda K_{T,r}/V_r} \ . \tag{C.9}$$

Then using the thermodynamic relations,

$$\left(\frac{\partial e}{\partial V}\right)_{T,\lambda} = -\left(P - \frac{\Gamma}{V} C_V \, T\right) \ , \tag{C.10}$$

applied to the reactant and products, the result for the mixture specific heat is

$$\begin{aligned} C_V = {} & \lambda \, C_{V,p} + (1-\lambda) \, C_{V,r} \\ & + \lambda \, (1-\lambda) \frac{K_T}{K_{T,p} K_{T,r}} \frac{V_p \, V_r}{V} \left[\frac{\Gamma_p C_{V,p}}{V_p} - \frac{\Gamma_r C_{V,r}}{V_r}\right]^2 T \ . \end{aligned} \tag{C.11}$$

We note that the mixture specific heat is greater than the mass weighted average of the reactant and products specific heats, *i.e.*, the first two terms on the right hand side of Eq. (C.11).

Again using the derivative $\frac{\mathsf{d}}{\mathsf{d}T}V_p$, the mixture Grüneisen coefficient can be obtained from Eq. (C.8),

$$\Gamma = \frac{V}{C_V}\left[\frac{\partial \widetilde{P}_p}{\partial T} + \frac{\partial \widetilde{P}_p}{\partial V}\,\frac{\mathsf{d}}{\mathsf{d}T}V_p\right] . \tag{C.12}$$

The result is

$$\Gamma = \frac{\lambda\,\Gamma_p C_{V,p}/K_{T,p} + (1-\lambda)\,\Gamma_r C_{V,r}/K_{T,r}}{C_V/K_T} . \tag{C.13}$$

It is readily checked that the mixture formulae for K_T, C_V and Γ have the correct limits for pure products ($\lambda = 1$), pure reactants ($\lambda = 0$), and when the reactants and products have the same EOS.

For completeness, we note an alternate derivation based on the Gibbs free energy, Eq. (2). The fundamental thermodynamic identity, Eq. (3), can be expressed as

$$\mathsf{d}G = V\,\mathsf{d}P - S\,\mathsf{d}T + \Delta G\,\mathsf{d}\lambda . \tag{C.14}$$

It is easy to show that the second derivatives are given by

$$\left(\frac{\partial^2 G}{\partial P^2}\right)_{T,\lambda} = -\frac{1}{(\rho\, c_T)^2} , \tag{C.15a}$$

$$\left(\frac{\partial^2 G}{\partial T^2}\right)_{P,\lambda} = -\frac{C_P}{T} . \tag{C.15b}$$

Equations (C.15a) and (2) yield Eq. (C.5). Similarly, Eqs. (C.15b) and (2) gives for the mixed specific heat at constant pressure

$$C_P = \lambda\, C_{P,p} + (1-\lambda)\, C_{P,r} . \tag{C.16}$$

Finally, the mixed second derivative is

$$\left(\frac{\partial^2 G}{\partial P\,\partial T}\right)_{\lambda} = \beta\, V , \tag{C.17}$$

where $\beta = V^{-1}(\partial V/\partial T)_{P,\lambda}$ is the coefficient of thermal expansion. Combined with Eq. (2), this gives the mixed coefficient of thermal expansion

$$\beta = \phi\,\beta_p + (1-\phi)\,\beta_r , \tag{C.18}$$

where $\phi = \lambda V_p/V$ is the volume fraction of the products. The equations for C_P and β are thermodynamically consistent with those for C_V and Γ since they all can be derived from the same thermodynamic potential.

C.1 Partial derivatives with respect to λ

The partial derivatives with respect to λ, $\left(\frac{\partial \widetilde{P}}{\partial \lambda}\right)_{V,T}$ and $\left(\frac{\partial e}{\partial \lambda}\right)_{V,T}$, can be obtained in terms of thermodynamic derivatives of the reactants and products component EOS as follows. Taking the derivative with respect to λ, at fixed V and T, of the pressure equilibrium condition, Eq. (C.1), yields

$$\frac{K_{T,p}}{V_p}\frac{\mathsf{d}}{\mathsf{d}\lambda}V_p - \frac{K_{T,r}}{V_r}\frac{\mathsf{d}}{\mathsf{d}\lambda}V_r = 0 \ , \tag{C.19a}$$

$$\lambda\frac{\mathsf{d}}{\mathsf{d}\lambda}V_p + (1-\lambda)\frac{\mathsf{d}}{\mathsf{d}\lambda}V_r = V_r - V_p \ . \tag{C.19b}$$

This determines the λ derivative of the component specific volumes

$$\frac{\mathsf{d}}{\mathsf{d}\lambda}V_p = \frac{K_{T,r}/V_r}{(1-\lambda)\,K_{T,p}/V_p + \lambda\,K_{T,r}/V_r}\left(V_r - V_p\right) \ , \tag{C.20a}$$

$$\frac{\mathsf{d}}{\mathsf{d}\lambda}V_r = \frac{K_{T,p}/V_p}{(1-\lambda)\,K_{T,p}/V_p + \lambda\,K_{T,r}/V_r}\left(V_r - V_p\right) \ . \tag{C.20b}$$

Substituting into Eq. (C.19a) leads to the desired pressure derivative

$$\begin{aligned}\left(\frac{\partial \widetilde{P}}{\partial \lambda}\right)_{V,T} &= \frac{V_p - V_r}{\lambda\,V_p/K_{T,p} + (1-\lambda)\,V_r/K_{T,r}} \\ &= \frac{V_p - V_r}{V}\,K_T \ .\end{aligned} \tag{C.21}$$

Since reactions typically increases the mole fraction, we expect that $V_p > V_r$, *i.e.*, in P–T equilibrium the HE products have a lower density than the reactants. In this case, $(\partial_\lambda \widetilde{P})_{V,T} > 0$.

Taking the derivative of the mixture specific energy, Eq. (C.7), using the chain rule, we obtain

$$\left(\frac{\partial e}{\partial \lambda}\right)_{V,T} = e_p - e_r + \lambda\left(\partial_V e_p\right)_T\frac{\mathsf{d}}{\mathsf{d}\lambda}V_p + (1-\lambda)\left(\partial_V e_r\right)_T\frac{\mathsf{d}}{\mathsf{d}\lambda}V_r \ . \tag{C.22}$$

Substituting Eq. (C.20) and the thermodynamic relation, Eq. (C.10), we find

$$\left(\frac{\partial e}{\partial \lambda}\right)_{V,T} = \left(h_p - h_r\right) - \frac{\lambda\left(\frac{\Gamma C_V}{K_T}\right)_p + (1-\lambda)\left(\frac{\Gamma C_V}{K_T}\right)_r}{\lambda\,V_p/K_{T,p} + (1-\lambda)\,V_r/K_{T,r}}\left(V_p - V_r\right)T \ , \tag{C.23}$$

where $h = e + P\,V$ is the enthalpy. This can be simplified using Eq. (C.5), Eq. (C.13) and Eq. (C.21) to yield

$$\begin{aligned}\left(\frac{\partial e}{\partial \lambda}\right)_{V,T} &= \left(h_p - h_r\right) - \Gamma\, C_V\, T\, \frac{V_p - V_r}{V} \\ &= \left(h_p - h_r\right) - \frac{\Gamma\, C_V\, T}{K_T}\left(\frac{\partial P}{\partial \lambda}\right)_{V,T} .\end{aligned} \tag{C.24}$$

For an exothermic reaction, $h_p - h_r < 0$. Since $V_p > V_r$, both terms on the right hand side of Eq. (C.24) are negative. Hence, $(\partial_\lambda e)_{V,T} < 0$.

C.2 Additional formula

The derivation of wave properties often depends on the sign of derivatives of thermodynamic quantities. Additional formula are derived below. These are obtained using the cyclic rule for variables x, y, z,

$$\left(\frac{\partial y}{\partial x}\right)_z \left(\frac{\partial z}{\partial y}\right)_x \left(\frac{\partial x}{\partial z}\right)_y = -1 , \tag{C.25}$$

and the chain rule for $f(x, y) = \hat{f}(x, z(x, y))$,

$$\left(\frac{\partial f}{\partial x}\right)_y = \left(\frac{\partial \hat{f}}{\partial x}\right)_z + \left(\frac{\partial z}{\partial x}\right)_y \left(\frac{\partial \hat{f}}{\partial z}\right)_x . \tag{C.26}$$

Applying the cyclic rule to the variables T, P, λ (with V held constant) yields

$$\left(\frac{\partial T}{\partial \lambda}\right)_{V,P} = -\frac{V}{\Gamma\, C_V}\left(\frac{\partial \widetilde{P}}{\partial \lambda}\right)_{V,T} . \tag{C.27}$$

If as expected $(\partial_\lambda \widetilde{P})_{V,T} > 0$, then $(\partial_\lambda T)_{V,P} < 0$.

The cyclic rule for variables T, e, λ (with V held constant) yields

$$\left(\frac{\partial e}{\partial \lambda}\right)_{V,T} = -\,C_V \left(\frac{\partial T}{\partial \lambda}\right)_{V,e} . \tag{C.28}$$

If as expected $(\partial_\lambda e)_{V,T} < 0$, then $(\partial_\lambda T)_{V,e} > 0$; *i.e.*, the temperature goes up as an adiabatically confined explosive burns.

Applying the chain rule and using Eq. (C.8),

$$\left(\frac{\partial P}{\partial \lambda}\right)_{V,e} = \left(\frac{\partial \widetilde{P}}{\partial \lambda}\right)_{V,T} + \frac{\Gamma}{V} C_V \left(\frac{\partial T}{\partial \lambda}\right)_{V,e} . \tag{C.29}$$

As noted previously, we expect $(\partial_\lambda T)_{V,e} > 0$ and $(\partial_\lambda \widetilde{P})_{V,T} > 0$. Hence, $(\partial_\lambda P)_{V,e} > (\partial_\lambda \widetilde{P})_{V,T} > 0$. The dimensionless quantity $(\partial_\lambda P)_{V,e}/K_S$ is called the thermicity. Physically, the first term on the right hand side of Eq. (C.29) is associated with the change in mole fraction and the second term with the heat release.

The cyclic rule applied to variable e, P, λ (with V fixed) yields

$$\left(\frac{\partial e}{\partial \lambda}\right)_{V,P} = -\frac{V}{\Gamma} \left(\frac{\partial P}{\partial \lambda}\right)_{V,e} . \tag{C.30}$$

Since the thermicity is positive, we obtain $(\partial_\lambda e)_{V,P} < 0$.

Derivatives of the mixture entropy can be derived using Eq. (3). Most important is the relation

$$T\left(\frac{\partial S}{\partial \lambda}\right)_{V,e} = -\Delta G . \tag{C.31}$$

Since the reaction tends to minimize the entropy, the sign of $\Delta G = G_p - G_r$ determines the direction of the reaction. In particular, reactants go to products if $\Delta G < 0$. Finally, from Eq. (C.24) and the relation $h = G + T\,S$, it can be shown that

$$\left(\frac{\partial S}{\partial \lambda}\right)_{V,T} = \Delta S - \Gamma \frac{V_p - V_r}{V} C_V . \tag{C.32}$$

When the reaction significantly increases the mole fraction, we expect $S_p \gg S_r$. In this case, $(\partial_\lambda S)_{V,T} > 0$.

C.3 Partly burned Hugoniot loci

For a fixed wave speed, or mass flux m, on the partly burned Hugoniot loci, the specific volume as a function of λ is determined by a system of ODEs. In particular, from Eq. (33),

$$\frac{\mathsf{d}}{\mathsf{d}\lambda} V = \frac{(\partial_\lambda \widetilde{P})_{V,T} - \frac{\Gamma}{V}(\partial_\lambda e)_{V,T}}{(\rho\, c)^2 - m^2} . \tag{C.33}$$

Using Eq. (C.28) and Eq. (C.29) the numerator reduces to $(\partial_\lambda P)_{V,e}$, which is proportional to the thermicity. The denominator only vanishes at a sonic point. Consequently, when the thermicity is positive, $\frac{\mathrm{d}}{\mathrm{d}\lambda}V > 0$ on the subsonic branch and $\frac{\mathrm{d}}{\mathrm{d}\lambda}V < 0$ on the supersonic branch. Therefore, $V(\lambda)$ would be monotonic on each branch.

Moreover, for positive thermicity, Eq. (C.30) implies that e, for fixed V and P, is monotonically decreasing with λ. It then follows from the Hugoniot equation, $\Delta e = \frac{1}{2}(P + P_0)(V_0 - V)$, that partly burned Hugoniot loci with different values of λ, do not intersect in the (V, P)-plane.

We note that a phase transition, for example from a liquid to a gas, can be viewed as an endothermic reaction. With a sufficiently large change in mole fraction, the thermicity can be positive. In this case, a phase front will have properties similar to those of a deflagration wave.

C.4 Caveats

A P-T equilibrium mixture EOS is equivalent to maximizing the mixture entropy

$$S(V, e) = \lambda\, S_p(V_p, e_p) + (1 - \lambda)\, S_r(V_r, e_r)\ , \tag{C.34}$$

subject to the constraints that mass and energy are conserved

$$V = \lambda\, V_p + (1 - \lambda)\, V_r\ , \tag{C.35a}$$
$$e = \lambda\, e_p + (1 - \lambda)\, e_r\ . \tag{C.35b}$$

For a thermodynamically stable EOS, the entropy is jointly concave in V and e. Consequently, if the reactants and products each have thermodynamically stable EOS, then there is a unique equilibrium solution for V_p, e_p, and V_r, e_r. Moreover, the P-T equilibrium EOS is thermodynamically consistent and thermodynamically stable.

Outside the domain on which the component EOS are thermodynamically stable, the equilibrium EOS for a given V, e and λ may fail to exist. This can and sometimes does occur for model EOS typically used for solid reactants. Solid EOS models, such as the Mie-Grüneisen EOS with the principal shock Hugoniot as the reference curve, have been developed for compression. In expansion, sometimes by as little as $V/V_0 - 1 = 5\,\%$, the isothermal compressibility may go negative, which would violate thermodynamic stability.

The EOS difficulty sometime results from the choice of fitting form for the Grüneisen coefficient, such as $\Gamma/V = \text{constant}$, in which Γ grows unphysically large as V increases. However, the fundamental issue is due to the fact that a solid sublimates. Hence, at high temperature and low density, it is not physical to treat a solid as a single-phase material. It should also be noted that the reactant vapor is not chemically the same as the products. Moreover, rather than to simply vaporize, the large reactant molecules may break up into smaller intermediate molecules in a pyrolysis step. When this occurs, the assumption of a single-step reaction may not be adequate for a description of an explosive. The EOS difficulty is most severe for calculating the deflagration wave speed when the ahead state for the reactants is at ambient conditions; room temperature and one atmosphere.

In addition, empirical burn models used to simulate a detonation wave in a PBX, are typically insensitive to the thermal component of the explosive. Typically, the specific heats of the reactants and products are taken as constant. This simplification is not adequate for use with a temperature sensitive chemical reaction rate. In particular, the explosives used in PBXs are large molecules and the reactant specific heat has a significant variation with temperature.

Appendix D. Model EOS for PBX 9501

Both the reactants and products EOS models have a pressure in the Mie-Grüneisen form

$$P(V,e) = P_{\rm ref}(V) + \frac{\Gamma(V)}{V}\Big(e - e_{\rm ref}(V)\Big) \ , \tag{D.1}$$

and a thermodynamically consistent temperature. The reference curve for the reactants is the cold curve ($T = 0$ isotherm, which is also the $S = 0$ isentrope), and for the products is the isentrope through the CJ detonation state. Consequently, for both reactants and products,

$$e_{\rm ref}(V) = e_{\rm ref}(V_{\rm ref}) - \int_{V_{\rm ref}}^{V} \mathsf{d}V' \, P_{\rm ref}(V') \ . \tag{D.2}$$

Both EOS models are calibrated to high pressure data. In addition, $e_{\rm ref}(V_{\rm ref})$ for the products is chosen to be compatible with the Hugoniot equation for the ambient reactants state and the measured CJ detonation speed and pressure.

D.1 Reactants model

A Birch-Murnaghan fitting form is used for the pressure on the cold curve

$$P_c(V) = \tfrac{3}{2}K_c\Big[(V/V_c)^{-7/3} - (V/V_c)^{-5/3}\Big]\times \\ \Big(1 + \tfrac{3}{4}\Big[K_c' - 4\Big]\Big[(V/V_c)^{-2/3} - 1\Big]\Big) \ , \tag{D.3}$$

where K_c is the bulk modulus and $K_c' = \mathsf{d}K_c/\mathsf{d}P$, both evaluated at the reference specific volume V_c at which $P_c = 0$. The cold curve energy is

$$e_c(V) = e_c(V_c) - \int_{V_c}^{V} \mathsf{d}V' \, P_c(V') \ , \tag{D.4}$$

and $e_c(V_c) = 0$. The Grüneisen coefficient is taken to have the form

$$\Gamma(V) = a + b\,\frac{V}{V_c} \ . \tag{D.5}$$

The temperature is based on a quasi-harmonic model for lattice vibrations and a single temperature scale. The specific heat has the form

$$C(V,T) = \widehat{C}_V(T/\theta(V)) \ , \tag{D.6}$$

where the temperature scale is

$$\theta(V)/\theta(V_c) = \left(\frac{V_c}{V}\right)^a \exp\Big[b\,(V_c - V)/V\Big] \ , \tag{D.7}$$

$\theta(V_c) = 1\,\mathrm{K}$ serves to set the unit for the temperature, and the scaled specific heat has the form

$$\widehat{C}_V(\widetilde{T}) = \frac{\widetilde{T}^3}{c_0 + c_1\widetilde{T}^2 + c_2\widetilde{T}^2 + c_3\widetilde{T}^3} \ . \tag{D.8}$$

The temperature, $T(V,e)$, is determined by the equation

$$e - e_c(V) = \int_0^{T(V,e)} \mathsf{d}T'\, C(V,T') \ . \tag{D.9}$$

The EOS model can be derived from a thermodynamic potential, and hence is thermodynamically consistent; see [Menikoff, 2007, §4.3.4] and [Menikoff, 2009b, 2011].

The parameters fit to HMX diamond anvil cell compression data and shock Hugoniot data by Menikoff and Sewell [2003] have been adjusted slightly for PBX 9501, which is 95 wt % HMX. They are listed in table 6. The ambient state, $P_0 = 10^{-4}\,\mathrm{GPa}$ and $T_0 = 300\,K$, is $\rho_0 = 1.828\,\mathrm{g/cm^3}$ and $e_0 = 0.1753\,\mathrm{MJ/kg}$. The domain of the fit is $e \geq e_c(V)$ and $V \leq V_c$.

The fit for $P_c(V)$ can be extrapolated to $V < 0.622\,\mathrm{cm^3/g}$ before the compressibility $-V\mathsf{d}P_c/\mathsf{d}V$ goes negative. The extension of the EOS domain to larger V requires a modification to limit the value of Γ. For $V > V_c$, we use the form

$$\Gamma(V) = a + \frac{(V/V_c)\,\epsilon}{[(V/V_c - 1)^2 + \epsilon^2]^{1/2}}\, b \tag{D.10}$$

where ϵ is a parameter. This has the properties that Γ and $(\mathsf{d}/\mathsf{d}V)\Gamma$ are continuous at $V = V_c$, $\Gamma \to a + \epsilon b$ for large V, and $\frac{\mathsf{d}}{\mathsf{d}V}[\Gamma(V)/V] < 0$. The last condition guarantees that

$$\frac{\partial c^2}{\partial e} = V^2\left(\left[\frac{\Gamma(V)}{V}\right]^2 - \frac{\mathsf{d}}{\mathsf{d}V}\left[\frac{\Gamma(V)}{V}\right]\right) > 0 \ . \tag{D.11}$$

Thermodynamic consistency requires that $\Gamma = -\mathsf{d}\ln\theta/\mathsf{d}\ln V$. Therefore, θ also needs to be modified for $V > V_c$,

$$-\ln\left[\frac{\theta(V)}{\theta(V_c)}\right] = a\,\ln\left[\frac{V}{V_c}\right] + b\,\epsilon\,\ln\left[\frac{(V/V_c - 1 + [(V/V_c-1)^2+\epsilon^2]^{1/2}}{\epsilon}\right]. \quad \text{(D.12)}$$

While the extrapolation to larger V is thermodynamically consistent, it is not expected to be accurate.

D.2 Products model

The fitting form for pressure on the CJ isentrope is

$$P_{\rm CJ}(\rho) = \begin{cases} \rho^{\gamma_1}\sum_n a_1(n)\rho^n & \text{for } \rho < \rho_{sw}\ , \\ \rho^{\gamma_2}\sum_n a_2(n)\rho^n & \text{for } \rho > \rho_{sw}\ , \end{cases} \quad \text{(D.13)}$$

and for the Grüneisen coefficient

$$\rho\,\Gamma(\rho) = \begin{cases} \sum_n b_1(n)\rho^n & \text{for } \rho < \rho_{swg}\ , \\ \sum_n b_2(n)\rho^n & \text{for } \rho > \rho_{swg}\ . \end{cases} \quad \text{(D.14)}$$

The parameters fit to overdriven detonation wave data and release isentrope data [Fritz et al., 1996, Hixson et al., 2000] by M. Sam Shaw [private communications, LANL 2005] are given in the table 7. The polynomials have been constructed such that P, P' and P'' are continuous at ρ_{sw} and Γ is continuous at ρ_{swg}. The domain of the fit $0.5 < \rho < 3.4\,\mathrm{g/cm^3}$ has a range $0.35 < P_{\rm CJ}(\rho) < 90\,\mathrm{GPa}$. For lower densities the model losses accuracy, and for larger densities $c^2 = \mathsf{d}P/\mathsf{d}\rho < 0$ and the model becomes thermodynamically unstable.

For the initial state $\rho_0 = 1.836\,\mathrm{g/cm^3}$ and $P_0 = 0$, the CJ detonation state is given by: $\rho_{\rm CJ} = 2.4403\,\mathrm{g/cm^3}$, $P_{\rm CJ} = 34.9\,\mathrm{GPa}$ and detonation speed $D = 8.811\,\mathrm{km/s}$. The Rayleigh line is tangent to the reference isentrope at the CJ state. The energy on the CJ isentrope is defined by

$$e_{\rm CJ}(V) = e_{\rm CJ} - \int_{V_{\rm CJ}}^{V} \mathsf{d}V'\,P_{\rm CJ}(V') \quad \text{(D.15)}$$

with $e_{\rm CJ} = e_0 + \frac{1}{2}(P_0 + P_{\rm CJ})\,(V_0 - V_{\rm CJ})$ where the subscript '0' denotes the ambient state of the reactants. We note that initial state, for which the

CJ isentrope was calibrated, differs slightly from the ambient state of the reactants EOS model. We use $e_{\rm CJ} = 2.5385\,{\rm MJ/kg}$ corresponding to $\rho_{\rm CJ} = 2.4305\,{\rm g/cm^3}$, $P_{\rm CJ} = 34.86\,{\rm GPa}$ and $D = 8.773\,{\rm km/s}$.

The temperature along the CJ isentrope is given by

$$T_{\rm CJ}(V) = T_{\rm CJ}(V_0)\exp\Big[-\int_{V_0}^{V} {\rm d}V\,\Gamma(V)/V\Big]\ , \tag{D.16}$$

where $T_{\rm CJ}(V_0) = 2650\,{\rm K}$. Off the CJ isentrope

$$T(V,e) = T_{\rm CJ}(V) + \Big(e - e_{\rm CJ}(V)\Big)/C_V\ , \tag{D.17}$$

where the specific heat is $C_V = 2.09\times10^{-3}\,({\rm MJ/kg})/{\rm K}$.

Table 6: Parameters for PBX 9501 reactants EOS.

V_c	0.534418	cm^3/g
K_c	14.	GPa
K_c'	9.8	—
a	0.	—
b	0.9	—
ϵ	0.2	—
c_0	0.5265	K·kg/MJ
c_1	307.3	K·kg/MJ
c_2	183.1×10^3	K·kg/MJ
c_3	419.4	K·kg/MJ

Table 7: Parameters for PBX 9501 products EOS. Units for density and pressure are g/cm^3 and GPa, respectively.

	$\rho_{sw} = 2.10$		$\rho_{swg} = 2.5$	
n	a_1	a_2	b_1	b_2
0	0.6728985375	-219.2657856	0.	61.5054
1	7.874226637	543.2739202	0.43901	-61.5554
2	-40.42313566	-546.3149119		20.5154
3	66.04682011	289.1261639		-2.2234
4	-1.205555487	-85.06903635		
5	-104.6827535	13.21219714		
6	124.3984562	-0.8473		
7	-65.66713800			
8	16.83269500			
9	-1.702550000			
	$\gamma_1 = 1.4$	$\gamma_2 = 3.0$		

Appendix E. Nodal critical point

For the ahead state of the reduced model with zero viscosity, the matrix for the critical point, Eq. (52), has the form

$$\mathbf{A} = \begin{pmatrix} 1 & -b \\ \epsilon & 0 \end{pmatrix} , \tag{E.1}$$

where $\epsilon \ll 1$ and $b = \mathcal{O}(1) > 0$. Here we analyze the structure of the critical points, and discuss the effect of the boundary in phase space at either $\lambda = 0$ or $T = T_{\text{ign}}$.

The eigenvalue equation for the matrix $\mathbf{A}$ is

$$\alpha^2 - \alpha + \epsilon\, b = 0 \ . \tag{E.2}$$

The eigenvalues,

$$\alpha_\pm = \tfrac{1}{2}\Big(1 \pm [1 - 4\epsilon\, b]^{1/2}\Big) \ , \tag{E.3}$$

are both positve. The corresponding right eigenvectors are

$$\vec{r}_\pm = (2b, 1 \mp [1 - 4\epsilon\, b]^{1/2})^T \ . \tag{E.4}$$

To leading order in ϵ, the eigenvalues and eigenvectors are:

$$\alpha_1 = 1 \ , \quad \vec{r}_1 = (1, \epsilon)^T \ ; \tag{E.5}$$

$$\alpha_2 = \epsilon\, b \ , \quad \vec{r}_2 = (1, 1/b)^T \ . \tag{E.6}$$

Since $\mathbf{A}$ is not Hermitian, the eigenfunctions are not orthogonal. The left eigenvectors are

$$\vec{\ell}_1 = \frac{1}{1 - \epsilon\, b}\,(1, -b) \ , \tag{E.7}$$

$$\vec{\ell}_2 = \frac{b}{1 - \epsilon\, b}\,(-\epsilon, 1) \ . \tag{E.8}$$

Hence, $\mathbf{A} = \alpha_1\, \vec{r}_1 \otimes \vec{\ell}_1 + \alpha_2\, \vec{r}_2 \otimes \vec{\ell}_2$. For the case of interest, $\alpha_2 \ll \alpha_1$.

The linearized ODEs about the critical point are

$$\frac{\mathsf{d}}{\mathsf{d}\zeta} \begin{pmatrix} \hat{T} \\ \hat{\lambda} \end{pmatrix} = \mathbf{A} \begin{pmatrix} \hat{T} \\ \hat{\lambda} \end{pmatrix} \ . \tag{E.9}$$

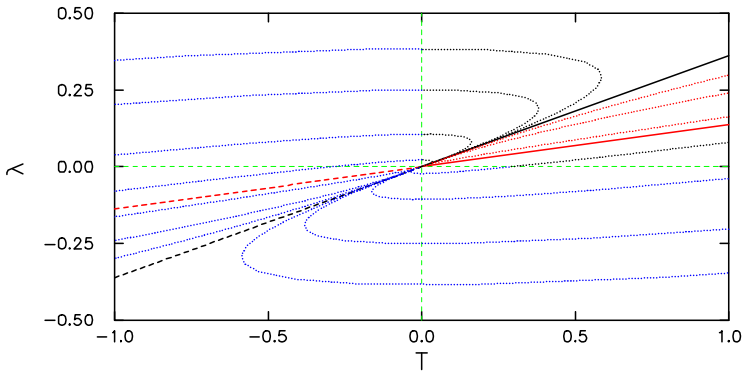

Figure 16: Solution trajectories for nodal critical point corresponding to the ahead state. Solid and dashed red lines correspond to the eigenfunction with the larger eigenvalue. Solid and dashed black lines correspond to the eigenfunction with the smaller eigenvalue. Dotted red lines correspond to $|c_1| > |c_2|$. Dotted black lines correspond to $|c_1| < |c_2|$. Dotted blue lines are the portion of the trajectory for which either $\lambda < 0$ or $T < T_{\text{ign}}$; *i.e.*, outside the physical domain.

For convenience, we assume here that the ahead state is at $\zeta = -\infty$ and that ζ increases as the trajectory heads towards the behind state at $\zeta = \infty$. The solution to Eq. (E.9) with $\hat{T}(-\infty) = 0$ and $\hat{\lambda}(-\infty) = 0$ is

$$\left(\hat{T}(\zeta), \hat{\lambda}(\zeta)\right)^T = c_1 \, \exp(\alpha_1 \zeta) \, \vec{r}_1 + c_2 \, \exp(\alpha_2 \zeta) \, \vec{r}_2 \; , \tag{E.10}$$

where c_1 and c_2 are arbitrary constants.

The phase portrait — solution trajectories as c_1 and c_2 are varied — is shown in Fig. 16 for the case with $\epsilon = 0.1$ and $b = 2$. The noteworthy feature is that unless $c_1 = 0$, the slope of the trajectories asymptotically approaches $\mathsf{d}\lambda/\mathsf{d}T \to \epsilon$ corresponding to the eigenvector $\hat{r}_1$. Moreover, as ϵ gets smaller the asymptotics sets in sooner. For a realistic case, $\epsilon \ll 1$, and the larger eigenvalue is even more dominant. This results in extreme curvature of the trajectories very close to the critical point. Moreover, $b = T^{-1}\mathsf{d}T_h/\mathsf{d}\lambda \approx T_1/T_0$ which may be about 10. Consequently, the angle of the sector between the two eigenfunction directions is much smaller than shown in the figure.

Mathematically, for a repeller node, the outgoing trajectories cover a local neighborhood of the critical point. Physically, however, there is a boundary on phase space; namely, $\lambda \geq 0$. Moreover, the linearization would be discontinuous for $T < T_{\text{ign}}$. Discarding those trajectories for which either $\lambda < 0$

or $\hat{T} < 0$, then for any $\epsilon > 0$ there would be no trajectory emanating from the critical point that traverses the line segment $\lambda = 0$ with $\hat{T} > 0$. For the purpose of determining a heteroclinic orbit corresponding to a deflagration wave, this has the effect of eliminating the degree of freedom at the ahead state normally associated with the repeller nature of the critical point.

References

Atwood, A. I., T. L. Boggs, P. O. Curran, T. P. Parr, D. M. Hanson-Parr, C. E. Price, and J. Wiknich. Burning rate of solid propellant ingredients, Part 1: pressure and initial temperature effects. *Journal of Propulsion and Power*, 15:740–747, 1999. 60

Bastea, S. Transport properties of fluid mixtures at high pressures and temperatures: Application to the detonation products of HMX. In *Proceedings of the Twelfth International Symposium on Detonation*, pages 576–583, 2002. 51

Bedrov, D., G. D. Smith, and T. D. Sewell. Temperature dependent shear viscosity coefficients of HMX, a molecular dynamics simulation study. *J. Chem. Phys.*, 112:7203–7208, 2000. 51

Campbell, A. W., and J. R. Travis. The shock desensitization of PBX-9404 and composition B-3. In *Eighth Symposium (International) on Detonation*, pages 1057–1068, 1986. 62

Courant, R., and K. O. Friedrichs. *Supersonic Flow and Shock Waves*. Springer-Verlag, 1976. reprint of 1948 edition. 1

Esposito, A. P., D. L. Farber, J. Reaugh, and J. M. Zaug. Reaction propagation rates in HMX at high pressure. *Propellants, Explosives, Pyrotechnics*, 28:83–88, 2003. 59, 61

Fickett, W., and W. C. Davis. *Detonation*. University of California Press, 1979. 64

Fifer, R. A., and J. E. Cole. Transitions from laminar burning for porous crystalline explosives. In *Proceeding of the Seventh International Symposium on Detonation*, pages 164–174, 1981. 61

Friedrichs, K. O. On the mathematical theory of deflagrations and detonations. Technical Report Naval Report 79-46, Bureau of Ordinance, 1946. 1

Fritz, J. N., R. S. Hixson, M. S. Shaw, C. E. Morris, and R. G. McQueen. Overdriven-detonation and sound-speed measurements in PBX 9501 and

the thermodynamic Chapman-Jouguet pressure. *J. Appl. Phys.*, 80:6129–6149, 1996. 48, 81

Garbey, M. Domain decomposition to solve transition layers and asymptotics. *SIAM J. Sci. Comput.*, 15:866–891, 1994. 20

Gasser, I., and P. Szmolyan. A geometric singular perturbation analysis of detonation and deflagration waves. *SIAM J. Math. Anal.*, 24:968–986, 1993. 2, 25

Gilbarg, D. The existence and limit behavior of the one-dimensional shock layer. *Am. J. Math.*, 73:256–274, 1951. 14, 34

Handley, C. A. *Numerical Modelling of two HMX-based Plastic-Bonded Explosives at the Mesoscale*. PhD thesis, University of St. Andrews, 2011. 59, 60

Henson, B. F., B. W. Asay, L. B. Smilowitz, and P. M. Dickson. Ignition chemistry in HMX from thermal explosion to detonation. In *Shock Compression of Condensed Matter – 2001*, pages 1069–1072, 2002. 48

Henson, B. F., L. B. Smilowitz, J. J. Romero, and B. W. Asay. Modeling thermal ignition and the initial conditions for internal burning in PBX 9501. In *Shock Compression of Condensed Matter – 2009*, pages 257–262, 2009. 52

Hixson, R. S., M. S. Shaw, J. N. Fritz, J. N. Vorthman, and W. W. Anderson. Release isentropes of overdriven plastic-bonded explosive PBX 9501. *J. Appl. Phys.*, 88:6287–6293, 2000. 48, 81

Karpenko, I. I., V. G. Morozov, O. N. Chernysheva, and Y. V. Yanilkin. Calculations of rate of growth of hot spots during detonation taking into account the turbulent mechanism of energy transfer. *Russian Journal of Physical Chemistry B*, 2:157–161, 2008. 61

Kassoy, D. R. Mathematical modeling for planar, steady, subsonic combustion waves. *Ann. Rev. of Fluid Mech.*, 17:267–287, 1985. 5

Maienschein, J. L., J. F. Wardell, M. R. DeHaven, and C. K. Black. Deflagration of HMX-based explosives at high temperatures and pressures. *Propellants, Explosives, Pyrotechnics*, 29:287–295, 2004. 60

Mang, J. T., R. P. Hjelm, and E. G. Francois. Measurement of porosity in a composite high explosive as a function of pressing conditions by ultra-small-angle neutron scattering with contrast variations. *Propellants, Explosives, Pyrotechnics*, 35:7–14, 2010. 62

McGuire, R. R., and C. M. Tarver. Chemical decomposition model for the thermal explosion of confined HMX, RDX and TNT explosives. In *Proceeding of the Seventh International Symposium on Detonation*, pages 56–64, 1981. 52, 60

Menikoff, R. Detonation waves in PBX 9501. *Combustion Theory Modelling*, 10:1003–1021, 2006. 49, 50, 67

Menikoff, R. Empirical equations of state for solids. In Horie, Y., editor, *Shock Wave Science and Technology Reference Library: Solids I*, volume 2, chapter 4. Springer-Verlag, 2007. 48, 66, 71, 80

Menikoff, R. Comparison of constitutive models for plastic-bonded explosives. *Combustion Theory Modelling*, 12:73–91, 2008. 48, 67

Menikoff, R. On beyond the standard model for high explosives: Challenges & obstacles to surmount. In *Shock Compression in Condensed Matter–2009*, volume 1195 of *AIP Conf. Proc.*, pages 18–25, 2009a. 2, 48

Menikoff, R. Complete EOS for PBX 9502. Technical Report LA-UR-09-06529, Los Alamos National Lab., 2009b. 48, 80

Menikoff, R. Complete Mie-Grüneisen Equation of State. Technical Report LA-UR-11-06921, Los Alamos National Lab., 2011. 80

Menikoff, R., and B. J. Plohr. The Riemann problem for fluid flow of real materials. *Reviews of Modern Physics*, 61:75–130, 1989. 5, 14

Menikoff, R., and T. D. Sewell. Constituent properties of HMX needed for mesoscale simulations. *Combustion Theory Modelling*, 6:103–125, 2002. 50

Menikoff, R., and T. D. Sewell. Complete equation of state for beta-HMX and implications for initiation. In *Shock Compression in Condensed Matter–2003*, pages 157–160, 2003. 48, 51, 80

Menikoff, R., and M. S. Shaw. Reactive burn models and ignition & growth concept. *EPJ Web of Conferences*, 10, 2010. doi: 10.1051/epjconf/20101000002. 48

Rayleigh, L. Aerial plane waves of finite amplitude. *Proc. Royal Society*, 84: 247–284, 1910. 14

Reaugh, J. E. Computer simulations to study the high-pressure deflagration of HMX. In *Shock Compression of Condensed Matter – 2003*, pages 401–404, 2004. 59, 60

Wagner, D. H. The existence and behavior of viscous structure for plane detonation waves. *SIAM J. Math. Anal.*, 5:1035–1054, 1989. 2, 36

Ward, M. J., S. F. Son, and M. Q. Brewster. Steady deflagration of HMX with simple kinetics: A gas phase chain reaction model. *Combustion and Flame*, 5114:556–558, 1998. 60

Weyl, H. Shock waves in arbitrary fluids. *Commun. Pure Appl. Math.*, 2: 103–122, 1949. 15

Zaug, J. M., C. E. Young, G. T. Long, J. L. Maienschein, E. A. Glascoe, D. W. Hansen, J. F. Wardell, C. K. Black, and G. B. Sykora. Deflagration rates of secondary explosives under static MPa–GPa pressure. In *Shock Compression in Condensed Matter–2009*, volume 1195 of *AIP Conf. Proc.*, pages 420–423, 2009. 59, 61